Understanding mechanisms of metastasis of aggressive breast cancers via microfluidic means

by

Steven Goble Allen

A dissertation submitted in partial fulfillment
of the requirements for the degree of
Doctor of Philosophy
(Cellular and Molecular Biology)
in the University of Michigan
2016

Doctoral Committee:

Professor Sofia D. Merajver, Chair
Professor Ronald J. Buckanovich
Professor Celina G. Kleer
Associate Professor Carey N. Lumeng
Professor Gabriel Nuñez

For Dorothy Allen and George Goble who were
my inspirations for pursuing cancer research

Acknowledgements

I owe a great deal to countless people who have helped me along my way through my research career. First among them, and someone for whom words on a page cannot adequately convey the depths of my gratitude, is my mentor Sofia Merajver. I truly mean it when I answer others asking what I want to do after my training is completed and I say that I want to be my mentor. I have had the privilege over these past 5 years to attend clinic with her and see how she connects with and instantly *understands* her patients, to be a part of fundraising events and meetings with potential donors and see how she can inspire hope and enthusiasm for cures, and to be a part of her lab where she challenges her mentees and instills in them a zeal for discovery with her uncanny ability to just *know* where the field will be in 5 or 10 years. If I have learned just a fraction of what she has taught me, my graduate training will have been a success. I would also like to thank Sofia for her sage wisdom and acting as a second mother to me. I always valued and sought her guidance on important (and sometimes trivial) life matters outside the purview of research.

I would like to sincerely thank the past and current members of the Merajver Lab with whom I have worked alongside. Chief among them are Zhifen Wu and Liwei Bao without whom whatever research success I have had as a graduate student would not be possible. I am grateful for their tireless efforts and patient teaching

of a freshman graduate student while working on our collaborative projects. Former lab member, Laura Nejedlik, and current lab member, Joel Yates, also deserve special thanks for their insightful, almost daily, solicited informal critiques and suggestions on my projects as well as for the mental reprieve and joy of our countless lunches. I am also quite appreciative of all that Chelsea Fournier, a former undergraduate student, did for me while she was here. Her laboratory technical skill and Excel mastery know no bounds. There are countless others, past and present, in the Merajver Lab too numerous to list that I am also indebted to and would like to thank. I would like to also acknowledge and thank the very special significant and generous donors who have provided funds to let our work in the Merajver be only limited by our imagination.

Good science is team science and all of my projects have had a significant collaborative element integral to their success. I worked very closely with Yu-chih Chen, formerly in Euisik Yoon's lab now a post-doc in Max Wicha's lab, and Weiqiang Chen, formerly in Jianping Fu's lab now an Assistant Professor at NYU of his own lab, on numerous projects and am a better scientist because of our collaborations. I also want to especially thank Celina Kleer, who also is a member of my thesis committee, for her many hours using her pathological acumen reviewing histologic slides all the while teaching a little pathology to this interested medical student. Kathy Toy in her lab deserves my gratitude as well for the immunostaining of those slides. I am also indebted to the other members of my committee – Ronald Buckanovich, Carey Lumeng, and Gabriel Nuñez – for

their insightful evaluation and valuable suggestions on my research as it progressed.

To my family and friends, thank you. Thank you for your love, your support, our laughter, and the joy you have brought me over these past years. Weekly Nagomi sushi dinners catching up with local friends and yearly New Year's Eve travel enjoying the company of distant friends really are the simple highlights I look forward to.

And to my beautiful wife Brittany, what can I say? You inspire me, you ground me, you sustain me, and you (and Rosie) bring me joy. My graduate school years would not nearly have been as pleasurable as they were without you. I am looking forward to our many years to come.

Table of Contents

List of Tables

List of Figures

Chapter 1

Introduction

A woman in the United States in her lifetime has a 1 in 3 chance of being diagnosed with cancer[1]. Of those diagnosed, the greatest percentage will have breast cancer[1]. Focused research and public health efforts over the last 40 years since the signing into law of the National Cancer Act have contributed to dramatic increases in 5-year survival rates for all cancers from 50% in 1975 to nearly 70% in 2010, and for breast cancer from 75% to over 90%[1]. However, the greatest strides have come from the successful treatment of the early stages of cancer. This is evidenced by the 99% 5-year survival rate for breast cancers defined as localized disease compared to the tragic 25% 5-year survival rate for those that have disease spread to other organs[1].

This spread of cancer from its initiating site to propagate in other organs is called metastasis, and it is this stage of the disease that is most feared by clinicians and patients alike as it is responsible for over 90% of cancer deaths[2,3]. Yet despite the clinical challenges metastasis poses, it is still a biological program and may be parsed into its constitutive subroutines, each to be interrogated and inspected for an obscured fault in the process that might be exploited by a new therapy, potentially adding to the oncologist's options for metastatic disease treatment. In

this work, I investigate the metastatic process at various levels looking for such exploitable subtleties by asking the following questions and answering them in the subsequent chapters. They are:

Chapter 2: *What are genetic molecular drivers that allow certain cancer cells to metastasize?*

Chapter 3: *What are environmental cues to tumor cells that trigger metastasis?*

Chapter 4: *Can we harness physical property differences to isolate cancer cells in patients once they do metastasize?*

Chapter 5: *Is there an overall mechanical phenotype of the most aggressive tumor cells that are successful in metastasis?*

The biological program of metastasis that tumor cells undergo is termed the metastatic cascade[4,5]. In this metaphor, cascade conjures up images of rushing waterfalls pouring en masse from one level to the next, but cancer cells are not as homogenous as the water molecules in a river. Tumors are comprised of a heterogeneous population and not every cell in a primary tumor has the intrinsic capability to metastasize. This was definitively shown by Isaiah Fidler in 1977[6]. In that work, he divided a murine melanoma cell line into two halves, injecting portions of one half into a series of mice and using the other half to generate clonal populations from individual cells[6]. If every cell in the original population was capable of forming metastases, then all mice injected with the clonal populations should have similar numbers of metastases as those mice injected with the parental cell line mixture. What he observed instead was that the clonal populations had a broad range of metastases some with fewer than the parental

line and some with many times more[6]. This was not an artifact brought about by the cloning procedure as re-cloning two of the original moderately metastatic subclones maintained a similar burden of metastasis[6]. This conclusively demonstrated that not all cells within a cell line are equal in their capability to metastasize. The group later showed similar results with a human melanoma cell line[7]. Another group then expanded these observations and was able to track the expansion of a clonal population *in vivo* rather than artificially pre-select populations *in vitro*[8]. They transfected plasmid DNA and used the random insertion location as a unique identifier for clones. After injecting mice with this heterogeneous population of transfected cells, they isolated and analyzed the metastatic lesions determining that each lesion was formed by one clone from the original population[8]. That is, each metastasis had cells with only one insertion site. Primary tumor heterogeneity and the metastatic capability of only select cells from the original tumor has held true to the present day with researchers now using modern deep-sequencing techniques on primary and metastatic tumor samples from patients directly rather than from mouse models[9,10]. What these studies show is that in order to stop the lethal process of metastasis, preventing a tumor from growing in size is not enough. We must understand the characteristics of the metastatic cells specifically and what factors allow them to metastasize and the others cells not.

The challenge in studying the metastatic population of cells, however, lies in their rarity. Only few cells at every step in the metastatic process are able to meet the

varied and differing criteria required of them to successfully metastasize[11-19]. In seminal work as a PhD student, Fidler demonstrated only 1.5% of cells injected into the tail veins of mice survived 24 hours and 0.5% survived 72 hours[16]. Lower percentages were seen by other groups analyzing later time points in experimental mouse models of metastasis with only 0.1% of tail vein injected cells dividing after 11 days in one study[17] and just 0.02% of injected cells growing into metastatic tumors in another[15]. An important consideration to these works is the artificial nature of the experimental setup. Cancer cells were injected directly into the circulation of mice and not shed from primary tumors. However, sobering studies in humans quantified just how unlikely it is for metastasis to occur in a clinical setting as well[11,12]. Weiss's group collected blood from the renal vein in patients undergoing nephrectomy for renal carcinoma[12]. Ostensibly, the renal vein would contain all cancer cells shed into the circulation by the primary renal tumor. One patient had a 10 cm primary tumor that shed 7,309 tumor emboli per 1 mL of collected blood yet had no detectable metastases after surgery over 2 years later[12]. Given a renal blood flow of about 500 mL per minute[12], this patient's tumor was releasing countless cancer cells every day into her circulation prior to resection and none were able to successfully grow. Tarin *et. al.* in a more dramatic example with a prospective study followed patients with peritoneovenous shunts to relive their chronic ascites generated from incurable abdominal tumors[11]. Multiple patients released tens of *millions* of viable cancer cells as measured by a clonogenicity assay from their ascites directly into their jugular vein every 24 hours, yet about half of the 15 patients autopsied after

death had no metastases to other organs – including one patient who survived 27 months after the shunt was placed[11]. Certainly other patients did develop lethal metastases in each study, but they were only from very rare cells of the heterogeneous population – estimated to be <0.01% of those that even leave the primary tumor[11,12,15,16,20,21] – that ultimately flourished at distant sites and killed the patients.

Beginning with first principles, naturally, in order to form metastases one must first have a primary tumor. The biological processes that govern tumor initiation and growth and the heritable and environmental factors that may predispose to cancer formation are worthy of intense study themselves[22-24], but they are beyond the scope of this work. However, the Appendix details the study of a rare auto-immune breast disease that shares a striking geographic overlap with a particularly aggressive form of breast cancer. Much more investigation is warranted in order to definitively establish or refute this relationship, but I hypothesize this rare disease might prepare the necessary breast environment for a specific type of aggressive breast cancer to take hold.

Once a primary tumor has formed though, the series of steps a cancer cell must traverse in order to form a metastasis are: acquiring motion, invading into local tissue, entering the lymphatics or blood vessels, surviving in circulation, leaving the vasculature, and finally proliferating in the new location[2,13,19-21,24-30]. Because of the rarity of the cells that can successfully navigate this process and the

inefficiency at each step, metastasis should not be thought of as a cascading, progressive waterfall of cancer cells, but rather a series of sieves each presenting an obstacle only tumors cells with certain traits can bypass and move on to the next step.

Acquiring the capability to migrate and invade the normal surrounding parenchyma represents the first metastatic sieve separating cancer cells from normal cells[31]. This change is the transition of a lesion from a benign adenoma to a carcinoma. E-cadherin, the main adhesion molecule of epithelia, is frequently lost during this transition in many cancers and was first shown as a necessary step in a transgenic mouse model of pancreatic ß-cell carcinogenesis[32]. In this model, E-cadherin was expressed in the non-invasive adenoma stage in all samples, but in over 200 spontaneous ß-cell carcinomas it was lost[32]. This mouse model of spontaneous cancer was then crossed with another model that had E-cadherin expression driven by the insulin promoter to maintain E-cadherin expression. The tumor incidence in the double transgenics dropped from 26% to 8% and, notably, all carcinomas that did arise in the double transgenics had lost the expression of E-cadherin – even the transgene expression – demonstrating the strong negative selective pressure against this common epithelial adhesion marker as a necessary step in the formation of ß-tumors[32]. After cancer cells lose normal adhesion proteins, they must gain the ability to migrate. Erik Sahai's group demonstrated the role of transforming growth factor ß (TGF-ß) in inducing this motility switch in breast cancer[33]. Using

intravital imaging and a fluorescent reporter of TGF-ß activity, they saw heterogeneity in TGF-ß signaling throughout the tumor with its activity coinciding with just the 5% of cells that were motile[33]. This work further demonstrated the inefficiency of the metastatic process as 95% of the primary tumor cells were non-motile[33]. Also important in bypassing this first metastatic sieve and progressing to an invasive carcinoma is the role of the normal stromal cells and basement membrane surrounding a lesion[34]. In a breast cancer model of ductal carcinoma in situ (DCIS), the loss of myoepithelial cells and a degradation of the basement membrane was required for the transition from DCIS to invasive carcinoma[35]. Furthermore, co-injection of myoepithelial cells could suppress the conversion[35]. Taken together, these studies accurately portray the first challenge of the metastatic series of sieves in that would-be metastatic cells must lose cellular adhesion proteins and gain motility and normal stromal cells act in regulating this step.

The next sieve, intravasation, involves cancer cells moving between endothelial cell junctions, or transcellularly through the endothelial cells themselves[36], and entering the lumina of lymphatic or blood capillaries[20,21] Condeelis and Segall's group was able to directly visualize this process *in vivo*[37,38]. Using fluorescently labeled metastatic and non-metastatic cell rat mammary adenocarcinoma cell lines and time lapse *in vivo* imaging, they followed cancer cells as they moved through the tumor and intravasated into capillaries. Upon reaching the capillary, the non-metastatic cell line fragmented apart as it could not withstand the

geometric rigors of squeezing through the endothelium[37]. In a separate study, the same group showed a necessary role for perivascular macrophages, a component of the normal stroma, aiding in the intravasation step[38]. Furthermore, the vessels cancer cells use to intravasate are not pre-existing but are newly formed with the growth of the lesion. The growing tumor induces lymphangiogenesis by secreting vascular endothelial growth factor (VEGF), specifically VEGF-C and VEGF-D[21,39-43]. Seminal studies demonstrated a role for VEGF in breast and other cancers by overexpressing it in various cell lines[41-43]. The tumors grown from cell lines overexpressing VEGF had increased growth of new lymphatic vessels coupled with increased cancer metastasis through these newly formed vessels[41-43]. Later work showed this newly formed tumor vasculature was weakened and "leaky" as compared to mature vessels in normal tissues due to secreted signals from the tumor, a characteristic which further facilitated intravasation[44,45].

Once in the circulation, cancer cells are called circulating tumor cells (CTCs) and must survive the inhospitable circulatory system plagued with hemodynamic shear forces and immune-mediated killing[20,21,26,46]. CTCs must ultimately physically lodge or, via cell surface receptors, attach to the endothelium in a distant organ. In one of the earliest CTC studies, Zeidman watched as CTCs lodged in or passed through the mesenteric capillaries of anesthetized rabbits[47]. He injected suspensions of cancer cells into the mesenteric artery and filmed the arterio-capillary junction as the cancer cells either deformed in shape and

squeezed through the constriction or maintained their rigid shape and arrested at the junction[47]. Arresting was not merely a function of cancer cell size as some large cells never arrested being pliable enough to circulate and other smaller more rigid cells arrested immediately[47]. Further research demonstrated a role for platelets and fibrin forming emboli with the tumor cells leading to their arrest in vessels[48,49] and more recently activated integrin on a cancer cell's surface was shown to promote metastasis by interacting with platelets and causing the arrest of cancer cells in the vasculature[50]. Of note, only a subpopulation of the breast cancer cell line used in the study expressed activated integrin[50]. Once arrested in a blood vessel, the cancer cell either migrates across the endothelial cell barrier or, as some studies have shown[21,51,52], simply multiplies and grows large enough to rupture the vessel. In conjunction with the intravasation studies, this body of work suggests a metastatic cell must have a precise biomechanical phenotype in order to be deformable enough to squeeze into a blood vessel but not so pliable that it never arrests in circulation. It must also display the proper integrin signal to interact with platelets to form a tumor embolus.

In the final stage of metastasis, a cancer cell must overcome the last metastatic sieve and proliferate in its new location. While some metastases grow intravascularly and rupture the vessel, many extravasate and remain dormant[53-56]. Judah Folkman pioneered the concept of primary tumors requiring new vasculature to grow beyond a diffusion limited size[57,58] and his group also later demonstrated a need for angiogenesis at metastatic sites for proliferation[53,54]. In

their later work, the Folkman group showed that systemic suppression of angiogenesis maintained stable-sized micrometastases[54]. His group determined these stable metastases proliferated just as rapidly as growing metastases, but without sufficient nutrients to support a larger population, their growth was balanced by a higher degree of apoptosis[54]. Another group – using a chronic cranial window in mice and fluorescently labeled cancer cells – imaged in real-time as cells arrested, extravasated, and moved to a perivascular position and remained dormant in the mouse brain[56]. This nutrient-rich perivascular position was essential for survival as cells that migrated too far away perished[56]. Ann Chambers's group similarly investigated metastatic dormancy using a nanoparticle dye to track individual cells of highly metastatic and lowly metastatic mammary carcinoma cell lines[55]. They found that only 0.006% of cells in the highly metastatic population formed metastases corroborating the rarity of successful metastatic cells; and, interestingly, in the lowly metastatic cell line they found that a significant portion of these cells were able to successfully extravasate but remained quiescent afterwards neither dividing or dying[55]. These lowly metastatic cells had all the capabilities required to get to the final site of a metastasis, but yet failed at the last step and were unable to ultimately grow. Taken together, these studies demonstrate the true inefficiency of the metastatic series of sieves. Even if a cancer cell is successful in gaining motility and intravasating, survives the circulation and arrests, is able to extravasate and remains close enough to a vessel to receive nutrients, a cancer cell must still

finally receive the proper signals and be in the right microenvironment to flourish, otherwise it will lay dormant.

Imbued with the knowledge of the metastatic journey of a cancer cell through often fibrotic tissues, squeezing into blood vessels in the small spaces between other cells, being pumped around the body in the circulation, and crawling back out again in a distant organ, it is easy to come to see how very physical and mechanical in nature the process is[59-61]. As was exampled above, a non-metastatic cell line while able to bypass the first metastatic sieve becoming an invasive carcinoma could not withstand the geometric constraints of intravasation or the circulatory shear forces and was immediately fragmented after entering the capillary lumen[37]. Another study demonstrated that a cancer cell could be too flexible and not arrest in a blood vessel to form a metastasis[47]. However traversing the metastatic series of sieves is not just a one-way interaction of the cancer cells moving through their environment. In fact, there is increasing evidence that physical environmental itself signals to cancer cells and can dictate cellular behavior and alter tumor characteristics[59-63]. Valerie Weaver's group first demonstrated a role for substrate stiffness in altering a breast cancer cell's intracellular signaling[64]. In *in vitro* work in 2D and 2D cultures, they modified the stiffness of mixed collagen and basement membrane gels and investigated the activity of known mechanotransducers. They found that by increasing the stiffness of the substrate, much as a tumor is stiffer than its surrounding tissue, integrin adhesions linked this mechanical input to intracellular signaling pathways

that enhance growth and promote malignant transformation[64]. Other groups demonstrated more global changes such as increased histone acetylation in cancer cells grown in suspension versus adherent cultures[65] and altered chromosomal nuclear localization with a corresponding change in gene expression in response to differently shaped nanopillars generating different forces on the cytoskeleton[66]. More recent studies by the Weaver group proved that mechanical inputs not only change cell signaling or gene expression *in vitro*, but that tumor rheology can have a functional effect *in vivo*[67]. They used a transgenic mouse model of breast cancer and fibroblasts expressing different levels of lysyl oxidase, an enzyme that initiates the crosslinking of collagen and increases stiffness of the extracellular matrix, to test the importance of this matrix remodeling and stiffening. They showed that fibroblasts in the mammary fat pad expressing high amounts of lysyl oxidase lead to tissue stiffening which promoted tumor growth via increased signaling by focal adhesion kinase and phosphatidylinositol-3-kinase[67]. Inhibition of lysyl oxidase reversed this effect[67]. They further showed the tumor promotion was not due to any secreted factor but due to changes in rheology alone[67]. Therefore, given the bi-directional nature of the environmental physical inputs to cancer cells and metastatic cells' biomechanically guided traversing of the metastatic process, in order to study the metastatic series of sieves effectively one requires both the capability to precisely control physical attributes of a cell's surroundings and the understanding of cancer biology. The engineering field of microfluidics affords just this opportunity

to marry precision engineering on a micrometer scale with testing clinically relevant questions of metastasis.

Microfluidics deals with the manipulation of fluids on the very small scale – typically microliter volumes in channels 1 μm to 1000 μm[68,69]. The laws of physics at this size scale allow for precision in controlling multiple variables on the cellular level[68-71]. The main disadvantage of *in vivo* studies of metastases is that this tight regulation is not possible[70,71]. Over the last decade, there has been a dramatic rise in the use of microfluidic engineered devices for applications in cancer[68,69,72,73]. They have been particularly useful in cancer metastasis research in two main areas: as advanced cell migration assays and as tools to separate and collect cancer cells from the circulation[68,69]. For harvesting circulating tumor cells, they afford a larger surface to volume ratio increasing the likelihood of capturing these exceedingly rare cells[68]. Mehmet Toner's group has proved microfluidic technology's utility for capturing CTCs in two seminal studies[74,75]. The used a microfluidic chip, termed the CTC-chip, which had 78,000 microposts coated with anti-epithelial-cell-adhesion-molecule antibody to capture CTCs[74]. They captured CTCs from 112 of 113 patients by processing their samples of whole blood directly through the CTC-chip and were able to further manipulate the captured cells for RNA extraction for RT-PCR analysis, which is an important investigative capability the other immunomagnetic-bead purification assays lack[74]. A later improvement in the design facilitated greater

cancer cell-micropost interaction under gentler flow that allowed for the discovery of clusters of cancer cells and leukocytes circulating together in patients[75].

Microfluidic techniques' primary advantages in chemotactic assays are the capability to generate defined and complex concentration gradients of various factors, direct visualization of migrating cells, and the ability to engineer specific structures to mimic the tumor environment[68-71,76]. Shuichi Takayama's group used these advantages to engineer a device to study the role of chemokine receptors in the CTC adhesion and extravasation step in the metastatic series of sieves[77]. They created a monolayer of endothelial cells at the base of a channel and flowed breast cancer cells over their vasculature mimic calculating the percent that successfully arrested[77]. Importantly, the design of the device allowed for different stimulation of endothelial cells in upstream and downstream positions serving as an internal control for itself. Because of this ingenuity, they discovered the importance of the chemokine receptor, CXCR4, expressed by the endothelial cells themselves – and not just by the cancer cells as was previously known – in the adhesion and arrest of CTCs[77]. David Beebe's group in studying the DCIS to carcinoma transition in breast cancer used the precise patterning and localization of cells afforded by microfluidics to show that the transition to invasive cancer in this model was not just dependent on secreted factors, but also on physical cell-cell interaction between fibroblasts and the DCIS cell line[78]. They were able to separate the cells by small, defined distances that allowed for soluble factor diffusion but did not allow for cell-cell contact. At these ranges,

they saw an intermediate and incomplete transition to invasive cancer[78]. Only when the fibroblasts and DCIS cell line were positioned closely enough to physically interact did the transition to carcinoma complete[78]. Melody Swartz's group utilized the advantages provided by microfluidics to investigate the effects of interstitial fluid flow in the tumor microenvironment on cancer cell migration and invasion in 3D[79]. They found yet another example of tumor heterogeneity and that the breast cancer cells studied contained a subpopulation that was intrinsically stimulated to migrate in the direction of the fluid flow, i.e. towards the draining lymphatic vessels[79]. This observation could only be made in a microfluidic device allowing for the control of specific, slow flow rates and live cell imaging.

Because of the mechanical nature of the journey of a tumor cell through the metastatic series of sieves and for the aforementioned advantages of using microfluidics to study steps in this process, I utilized both microfluidic migration devices (Chapters 2 and 3) and circulating tumor cell capture devices (Chapter 4) in my study of metastasis (Fig. 1.1). In Chapter 2, cancer cells are challenged with a geometrically confining migration space which mimics the constraints of a lymphatic capillary and the early metastatic sieve intravasation. After migration, cells are recaptured and analyzed for genetic differences. In Chapter 3, the effects of secreted factors from normal immune cells in the tumor microenvironment are tested for their stimulation of cancer cell migration to bypass metastatic sieves. In Chapter 4, the adhesive property of cancer cells as

they differ from normal blood cells is leveraged as a novel paradigm for circulating tumor cell capture. Lastly, Chapter 5 presents work which represents a departure from the typical utility of microfluidics and using specifically designed microfluidic assays accomplishes a multiparametric cellular phenotyping of the most aggressive subpopulation of cancer cells' biomechanical properties, which may confer the capability to effectively traverse the metastatic series of sieves.

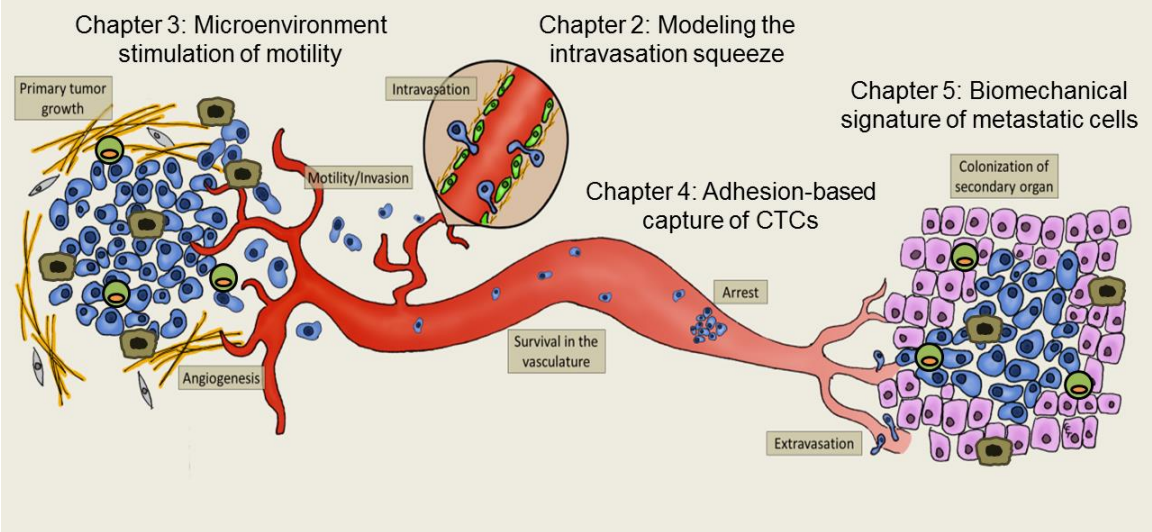

Figure 1.1. The metastatic series of sieves. An outline of the metastatic series of sieves and the steps studied by each of the subsequent chapters.

References

1 Siegel, R. L., Miller, K. D. & Jemal, A. Cancer statistics, 2015. *CA Cancer J Clin* **65**, 5-29, (2015).

2 Talmadge, J. E. & Fidler, I. J. AACR centennial series: the biology of cancer metastasis: historical perspective. *Cancer Res* **70**, 5649-5669, (2010).

3 Fidler, I. J. The pathogenesis of cancer metastasis: the 'seed and soil' hypothesis revisited. *Nat Rev Cancer* **3**, 453-458, (2003).

4 Viadana, E., Bross, I. D. & Pickren, J. W. An autopsy study of some routes of dissemination of cancer of the breast. *Br J Cancer* **27**, 336-340, (1973).

5 Bross, I. D., Viadana, E. & Pickren, J. W. The metastatic spread of myeloma and leukemias in men. *Virchows Arch A Pathol Anat Histol* **365**, 91-101, (1975).

6 Fidler, I. J. & Kripke, M. L. Metastasis results from preexisting variant cells within a malignant tumor. *Science* **197**, 893-895, (1977).

7 Kozlowski, J. M., Hart, I. R., Fidler, I. J. & Hanna, N. A human melanoma line heterogeneous with respect to metastatic capacity in athymic nude mice. *J Natl Cancer Inst* **72**, 913-917, (1984).

8 Waghorne, C., Thomas, M., Lagarde, A., Kerbel, R. S. & Breitman, M. L. Genetic evidence for progressive selection and overgrowth of primary tumors by metastatic cell subpopulations. *Cancer Res* **48**, 6109-6114, (1988).

9 Kuukasjarvi, T. *et al.* Genetic heterogeneity and clonal evolution underlying development of asynchronous metastasis in human breast cancer. *Cancer Res* **57**, 1597-1604, (1997).

10 Ding, L. *et al.* Genome remodelling in a basal-like breast cancer metastasis and xenograft. *Nature* **464**, 999-1005, (2010).

11 Tarin, D. *et al.* Mechanisms of human tumor metastasis studied in patients with peritoneovenous shunts. *Cancer Res* **44**, 3584-3592, (1984).

12 Glaves, D., Huben, R. P. & Weiss, L. Haematogenous dissemination of cells from human renal adenocarcinomas. *Br J Cancer* **57**, 32-35, (1988).

13 Poste, G. & Fidler, I. J. The pathogenesis of cancer metastasis. *Nature* **283**, 139-146, (1980).

14 Weiss, L. Metastatic inefficiency. *Adv Cancer Res* **54**, 159-211, (1990).

15 Luzzi, K. J. *et al.* Multistep nature of metastatic inefficiency: dormancy of solitary cells after successful extravasation and limited survival of early micrometastases. *Am J Pathol* **153**, 865-873, (1998).

16 Fidler, I. J. Metastasis: quantitative analysis of distribution and fate of tumor emboli labeled with 125 I-5-iodo-2'-deoxyuridine. *J Natl Cancer Inst* **45**, 773-782, (1970).

17 Baserga, R., Kisieleski, W. E. & Halvorsen, K. A study on the establishment and growth of tumor metastases with tritiated thymidine. *Cancer Res* **20**, 910-917, (1960).

18 Butler, T. P. & Gullino, P. M. Quantitation of cell shedding into efferent blood of mammary adenocarcinoma. *Cancer Res* **35**, 512-516, (1975).

19 Price, J. E., Aukerman, S. L. & Fidler, I. J. Evidence that the process of murine melanoma metastasis is sequential and selective and contains stochastic elements. *Cancer Res* **46**, 5172-5178, (1986).
20 Valastyan, S. & Weinberg, R. A. Tumor metastasis: molecular insights and evolving paradigms. *Cell* **147**, 275-292, (2011).
21 Reymond, N., d'Agua, B. B. & Ridley, A. J. Crossing the endothelial barrier during metastasis. *Nat Rev Cancer* **13**, 858-870, (2013).
22 Friberg, S. & Mattson, S. On the growth rates of human malignant tumors: implications for medical decision making. *J Surg Oncol* **65**, 284-297, (1997).
23 Gallaher, J., Babu, A., Plevritis, S. & Anderson, A. R. Bridging population and tissue scale tumor dynamics: a new paradigm for understanding differences in tumor growth and metastatic disease. *Cancer Res* **74**, 426-435, (2014).
24 Hanahan, D. & Weinberg, R. A. Hallmarks of cancer: the next generation. *Cell* **144**, 646-674, (2011).
25 Sahai, E. Illuminating the metastatic process. *Nat Rev Cancer* **7**, 737-749, (2007).
26 Gupta, G. P. & Massague, J. Cancer metastasis: building a framework. *Cell* **127**, 679-695, (2006).
27 Leong, S. P. *et al.* Clinical patterns of metastasis. *Cancer Metastasis Rev* **25**, 221-232, (2006).
28 Scully, O. J., Bay, B. H., Yip, G. & Yu, Y. Breast cancer metastasis. *Cancer Genomics Proteomics* **9**, 311-320, (2012).
29 van Zijl, F., Krupitza, G. & Mikulits, W. Initial steps of metastasis: cell invasion and endothelial transmigration. *Mutat Res* **728**, 23-34, (2011).
30 Chambers, A. F., Groom, A. C. & MacDonald, I. C. Dissemination and growth of cancer cells in metastatic sites. *Nat Rev Cancer* **2**, 563-572, (2002).
31 Friedl, P. & Wolf, K. Tumour-cell invasion and migration: diversity and escape mechanisms. *Nat Rev Cancer* **3**, 362-374, (2003).
32 Perl, A. K., Wilgenbus, P., Dahl, U., Semb, H. & Christofori, G. A causal role for E-cadherin in the transition from adenoma to carcinoma. *Nature* **392**, 190-193, (1998).
33 Giampieri, S. *et al.* Localized and reversible TGFbeta signalling switches breast cancer cells from cohesive to single cell motility. *Nat Cell Biol* **11**, 1287-1296, (2009).
34 Bissell, M. J. & Hines, W. C. Why don't we get more cancer? A proposed role of the microenvironment in restraining cancer progression. *Nat Med* **17**, 320-329, (2011).
35 Hu, M. *et al.* Regulation of in situ to invasive breast carcinoma transition. *Cancer Cell* **13**, 394-406, (2008).
36 De Bruyn, P. P. & Cho, Y. Vascular endothelial invasion via transcellular passage by malignant cells in the primary stage of metastases formation. *J Ultrastruct Res* **81**, 189-201, (1982).

37 Wyckoff, J. B., Jones, J. G., Condeelis, J. S. & Segall, J. E. A critical step in metastasis: in vivo analysis of intravasation at the primary tumor. *Cancer Res* **60**, 2504-2511, (2000).
38 Wyckoff, J. B. *et al.* Direct visualization of macrophage-assisted tumor cell intravasation in mammary tumors. *Cancer Res* **67**, 2649-2656, (2007).
39 Stacker, S. A., Achen, M. G., Jussila, L., Baldwin, M. E. & Alitalo, K. Lymphangiogenesis and cancer metastasis. *Nat Rev Cancer* **2**, 573-583, (2002).
40 Stacker, S. A. *et al.* Lymphangiogenesis and lymphatic vessel remodelling in cancer. *Nat Rev Cancer* **14**, 159-172, (2014).
41 Skobe, M. *et al.* Induction of tumor lymphangiogenesis by VEGF-C promotes breast cancer metastasis. *Nat Med* **7**, 192-198, (2001).
42 Stacker, S. A. *et al.* VEGF-D promotes the metastatic spread of tumor cells via the lymphatics. *Nat Med* **7**, 186-191, (2001).
43 Karpanen, T. *et al.* Vascular endothelial growth factor C promotes tumor lymphangiogenesis and intralymphatic tumor growth. *Cancer Res* **61**, 1786-1790, (2001).
44 Anderberg, C. *et al.* Deficiency for endoglin in tumor vasculature weakens the endothelial barrier to metastatic dissemination. *J Exp Med* **210**, 563-579, (2013).
45 Weis, S., Cui, J., Barnes, L. & Cheresh, D. Endothelial barrier disruption by VEGF-mediated Src activity potentiates tumor cell extravasation and metastasis. *J Cell Biol* **167**, 223-229, (2004).
46 Mehlen, P. & Puisieux, A. Metastasis: a question of life or death. *Nat Rev Cancer* **6**, 449-458, (2006).
47 Zeidman, I. The Fate of Circulating Tumor Cells. *Acta Cytol* **9**, 136-140, (1965).
48 Kinjo, M. Lodgement and extravasation of tumour cells in blood-borne metastasis: an electron microscope study. *Br J Cancer* **38**, 293-301, (1978).
49 Chew, E. C. & Wallace, A. C. Demonstration of fibrin in early stages of experimental metastases. *Cancer Res* **36**, 1904-1909, (1976).
50 Felding-Habermann, B. *et al.* Integrin activation controls metastasis in human breast cancer. *Proc Natl Acad Sci U S A* **98**, 1853-1858, (2001).
51 Al-Mehdi, A. B. *et al.* Intravascular origin of metastasis from the proliferation of endothelium-attached tumor cells: a new model for metastasis. *Nat Med* **6**, 100-102, (2000).
52 Ito, S. *et al.* Real-time observation of micrometastasis formation in the living mouse liver using a green fluorescent protein gene-tagged rat tongue carcinoma cell line. *Int J Cancer* **93**, 212-217, (2001).
53 O'Reilly, M. S. *et al.* Angiostatin: a novel angiogenesis inhibitor that mediates the suppression of metastases by a Lewis lung carcinoma. *Cell* **79**, 315-328, (1994).
54 Holmgren, L., O'Reilly, M. S. & Folkman, J. Dormancy of micrometastases: balanced proliferation and apoptosis in the presence of angiogenesis suppression. *Nat Med* **1**, 149-153, (1995).

55 Naumov, G. N. *et al.* Persistence of solitary mammary carcinoma cells in a secondary site: a possible contributor to dormancy. *Cancer Res* **62**, 2162-2168, (2002).
56 Kienast, Y. *et al.* Real-time imaging reveals the single steps of brain metastasis formation. *Nat Med* **16**, 116-122, (2010).
57 Folkman, J. & Greenspan, H. P. Influence of geometry on control of cell growth. *Biochim Biophys Acta* **417**, 211-236, (1975).
58 Folkman, J. Toward an understanding of angiogenesis: search and discovery. *Perspect Biol Med* **29**, 10-36, (1985).
59 Michor, F., Liphardt, J., Ferrari, M. & Widom, J. What does physics have to do with cancer? *Nat Rev Cancer* **11**, 657-670, (2011).
60 Wirtz, D., Konstantopoulos, K. & Searson, P. C. The physics of cancer: the role of physical interactions and mechanical forces in metastasis. *Nat Rev Cancer* **11**, 512-522, (2011).
61 Kumar, S. & Weaver, V. M. Mechanics, malignancy, and metastasis: the force journey of a tumor cell. *Cancer Metastasis Rev* **28**, 113-127, (2009).
62 Moore, N. M. & Nagahara, L. A. Physical biology in cancer. 1. Cellular physics of cancer metastasis. *Am J Physiol Cell Physiol* **306**, C78-79, (2014).
63 Stroka, K. M. & Konstantopoulos, K. Physical biology in cancer. 4. Physical cues guide tumor cell adhesion and migration. *Am J Physiol Cell Physiol* **306**, C98-C109, (2014).
64 Paszek, M. J. *et al.* Tensional homeostasis and the malignant phenotype. *Cancer Cell* **8**, 241-254, (2005).
65 Kim, Y. B. *et al.* Cell adhesion status-dependent histone acetylation is regulated through intracellular contractility-related signaling activities. *J Biol Chem* **280**, 28357-28364, (2005).
66 Dalby, M. J. *et al.* Nanomechanotransduction and interphase nuclear organization influence on genomic control. *J Cell Biochem* **102**, 1234-1244, (2007).
67 Levental, K. R. *et al.* Matrix crosslinking forces tumor progression by enhancing integrin signaling. *Cell* **139**, 891-906, (2009).
68 Zhang, Z. & Nagrath, S. Microfluidics and cancer: are we there yet? *Biomed Microdevices* **15**, 595-609, (2013).
69 Sackmann, E. K., Fulton, A. L. & Beebe, D. J. The present and future role of microfluidics in biomedical research. *Nature* **507**, 181-189, (2014).
70 Bersini, S., Jeon, J. S., Moretti, M. & Kamm, R. D. In vitro models of the metastatic cascade: from local invasion to extravasation. *Drug Discov Today* **19**, 735-742, (2014).
71 Zaman, M. H. The role of engineering approaches in analysing cancer invasion and metastasis. *Nat Rev Cancer* **13**, 596-603, (2013).
72 Sung, K. E. & Beebe, D. J. Microfluidic 3D models of cancer. *Adv Drug Deliv Rev* **79-80**, 68-78, (2014).
73 Keenan, T. M. & Folch, A. Biomolecular gradients in cell culture systems. *Lab Chip* **8**, 34-57, (2008).

74 Nagrath, S. *et al.* Isolation of rare circulating tumour cells in cancer patients by microchip technology. *Nature* **450**, 1235-1239, (2007).
75 Stott, S. L. *et al.* Isolation of circulating tumor cells using a microvortex-generating herringbone-chip. *Proc Natl Acad Sci U S A* **107**, 18392-18397, (2010).
76 Samatov, T. R., Shkurnikov, M. U., Tonevitskaya, S. A. & Tonevitsky, A. G. Modelling the metastatic cascade by in vitro microfluidic platforms. *Prog Histochem Cytochem* **49**, 21-29, (2015).
77 Song, J. W. *et al.* Microfluidic endothelium for studying the intravascular adhesion of metastatic breast cancer cells. *PLoS One* **4**, e5756, (2009).
78 Sung, K. E. *et al.* Transition to invasion in breast cancer: a microfluidic in vitro model enables examination of spatial and temporal effects. *Integr Biol (Camb)* **3**, 439-450, (2011).
79 Haessler, U., Teo, J. C., Foretay, D., Renaud, P. & Swartz, M. A. Migration dynamics of breast cancer cells in a tunable 3D interstitial flow chamber. *Integr Biol (Camb)* **4**, 401-409, (2012).

Chapter 2

Single-cell Migration Chip for Chemotaxis-Based Microfluidic Selection of Heterogeneous Cell Populations

This chapter has been previously been published in *Chen YC, *Allen SG, Ingram P, Buckanovich R, Merajver SD, Yoon E (2015) Single-cell migration chip for chemotaxis-based microfluidic selection of heterogeneous cell populations. Scientific Reports, 5, Article number: 9980.

Chapter Summary

The first two metastatic sieves a tumor cell must overcome are tumor cell migration toward and intravasation into capillaries, yet not all cancer cells are imbued with the same capability to do so. This heterogeneity within a tumor and the rarity of the successfully metastatic cells is a fundamental property of cancer. Tools to help us understand what molecular characteristics allow a certain subpopulation of cells to spread from the primary tumor and bypass the metastatic sieves are thus critical for overcoming metastasis. Conventional *in vitro* migration platforms treat populations in aggregate, which leads to a masking of intrinsic differences among cells. Some migration assays reported recently have single-cell resolution, but these platforms do not provide for selective retrieval of the distinct migrating and non-migrating cell populations for further analysis. Thus, to study the intrinsic differences in cells responsible for

chemotactic heterogeneity, we developed a single-cell migration platform so that individual cells' migration behavior can be studied and the heterogeneous population sorted based upon chemotactic phenotype. Furthermore, after migration, the highly chemotactic and non-chemotactic cells were retrieved and proved viable for later molecular analysis of their differences. Moreover, we modified the migration channel to resemble lymphatic capillaries to better understand how certain cancer cells are able to move through geometrically confining spaces.

Introduction

Cell migration is an essential process in angiogenesis, cancer metastasis, wound healing, inflammation, and embryogenesis. In particular, significant attention has been paid to the migration of cancer cells since cancer metastases account for more than 90% of cancer-related mortality.[1,2] Cancer metastases result from a multi-step process with significant attrition of viable cells at each stage in the metastatic series of sieves. One such rate-limiting step is the chemotactic migration and intravasation of tumor cells from the tumor stroma to a capillary bed or lymphatic vessels.[1-4] The study of the intravasation step has been hampered though by the lack of accessible *in vitro* techniques. Additionally, the regulation of certain metastasis-related genes also modulates the occurrence and burden of metastases. Although several genes have been discovered and may be potential targets for therapeutics,[5-7] the study of these metastasis-related genes still largely depends on xenograft or tail-vein injection mouse models,

which focus on global differences in large cell populations and require considerable time and expense thereby precluding their adaptation or input into personalized therapy.[2,4,8] Furthermore, single-cell resolution of mechanical differences and direct visualization are also at present impractical in xenograft-based experiments in which typically only metastatic growth endpoints are assessed rather than the interceding steps. Hence, there is a need to develop *in vitro* devices which can realistically emulate critical steps of the metastatic sieves – especially the confining geometry of intravasation into and migration through blood and lymphatic capillaries – and allow for the direct visualization of the process as well as allowing for the separation and further characterization of cells with differing chemotactic properties.[2,3]

Popular long-standing approaches for studying cell motility and invasion *in vitro* such as wound healing and transwell assays have significant limitations.[9,10] Wound healing assays present challenges both in the reproducibility of the scratch and in the inability to discern and separate the more motile from the less motile cells within a population.[11] Transwell assays provide quantitative binary motility results in large cell populations, but imaging of the actual migration process of the individual cells is not possible. These fundamental limitations preclude the use of these assays to understand in detail the migration of cancer cells under conditions that more closely mimic the series of metastatic sieves. Realizing these limitations and taking advantage of modern microfabrication technologies, a number of studies have employed microfluidic channels to study

cell migration more effectively.[12-16] In some studies, different channel cross-sectional sizes and geometries have been used to study the effects of geometry on cell migration,[15,17-20] while in others the migration channel was filled with hydrogel or extra-cellular matrix components in order to simulate the cancer invasion process through stroma.[21,22] In yet other approaches, two or more cell types were co-cultured in microfluidic channels to approximate the cellular diversity in the tissue micro-environment.[23-25] However, these previous microfluidic approaches that study collective migration behaviors lack the concurrent capabilities to trace in detail a single cell's behavior, capture migrating cells, and investigate cell population heterogeneity with regards to chemotaxis. Furthermore, the geometry-based studies were not on the biological scale of pre-lymphatics and lymphatic capillaries.[15,26-28]

Cellular heterogeneity is a key characteristic of cancer and cancer cell populations are diverse within a tumor mass.[1,29,30] Due to genetic differences as well as differing epigenetic and metabolic regulation, subgroups of cancer cells in a tumor have distinct growth advantages as the conditions change and thus diverse phenotypes with differing migration and metastatic capability evolve in a tumor mass over time.[30,31] As researchers have begun to recognize the importance of cellular heterogeneity contributing to metastasis, several studies have reported on techniques to study the migration behavior of individual cancer cells.[32-37] These prior platforms have a low capture efficiency, typically loading many cells yet only investigating a small portion. This inefficiency proves critically

unfavorable for applications that use rare samples such as primary tumor analysis. More importantly, these platforms, as with other microfluidic migration devices, do not allow for the retrieval of cells after the migration assay. This re-harvesting of the cells after the migration assay for further downstream analysis is of the utmost importance for an understanding of the fundamental causes of increased chemotaxis in some cells within a population that is otherwise the same. Although recently one study has demonstrated the separation of a cancer cell line population based on chemotactic phenotype, it did not enrich for increased chemotaxis in the selected subpopulation as compared to the parent population and required the loading of thousands of cells.[16]

Therefore, to overcome these and other limitations, we designed a single-cell migration platform that allows for the post-migration collection and analysis of differing chemotactic subpopulations of cells and that can be modified to geometrically mimic the tight spaces in the pre-lymphatic and lymphatic capillaries that a cancer cell must navigate on its way to metastasize.[3,26,28] Our platform incorporates a single-cell capture scheme which positions one cell at the entrance of each migration channel, so the chemotactic behavior of each individual cell can be specifically traced and delineated over time. Using this cell positioning technique, assays are performed by monitoring 20 captured cells in each device, making the platform favorable for future use with primary tumor samples and other rare cells in contrast to prior devices. Importantly, after the migration assays, the highly chemotactic cells can be retrieved for further

downstream molecular and phenotypic analysis in comparison to the non-chemotactic subpopulation.

We show that the highly chemotactic subpopulation of MDA-MB-231 breast cancer cells selected through the migration assay maintain this migratory phenotype after harvesting and reintroduction to the migration assay. Furthermore, the chemotactic cells have a more mesenchymal morphology compared to the non-chemotactic residual cells and also express significantly greater amounts of the mitogen activator of protein kinase (MAPK) isoform p38γ and Ras-homology (Rho) GTPase isoform RhoC, both critical modulators of mesenchymal motility in MDA-MB-231 cells.[38] Lastly, using our lymphatic capillary *in vitro* mimic, we corroborate our prior *in vivo* results that showed p38γ was necessary for contralateral lymph node metastasis.[38] We customized the migration channels in our device to include choke points on the geometric scale of the constricting lymphatic capillary dimensions *in vivo* in order to allow our study *ex vivo* of the capillary intravasation step of cancer metastasis to the lymph nodes.[26] Using p38γ shRNA knockdown and scrambled vector control breast cancer cells in our newly developed lymphatic-mimetic device, we show that the knockdown p38γ cells are unable to effectively traverse choke points at the critical size of 6 μm x 10 μm, which is the size of lymphatic vessels *in vivo*.[26] Our present device can thus be used to directly visualize one of the critical steps of the metastatic series of sieves in order to reveal further insights into what

molecular underpinnings allow certain cancer cells within a heterogeneous tumor to intravasate into capillaries and subsequently metastasize.

Results

Design of the single-cell capture scheme

The microfluidic device consists of single-cell capture sites and migration channels. Fig. 2.1 (A) shows a schematic diagram of the described chip and fabrication processes. To achieve single-cell resolution, cells are loaded by gravity flow and hydrodynamically captured at each capture site (Fig. 2.1(B)). We incorporated the capture area directly adjacent to the entrance of the narrow migration channel, an innovative feature as compared to other devices.[39-41] As shown in Fig. 2.1 (C), two paths are created: a shorter central path and a longer serpentine path. The flow rate of each path is inversely proportional to its hydrodynamic resistance. A long serpentine structure increases the hydrodynamic resistance (R_S), so the serpentine flow resistance is larger than that of the central path. Therefore, the serpentine flow (Q_S) is less than the central flow (Q_C), and cells will more likely follow the central path. As the opening of the central path is slightly smaller (height: 20 μm, width: 10 μm) than the size of cancer cells (e.g., SKOV3 cells has an average diameter of 14.1 μm, SD ±3.2 μm) and funnel-shaped, the captured cell consistently plugs the gap and blocks the flow through the central path (cell valving). Thus, the remainder of the cells travel through the serpentine path and are subsequently captured in the downstream capture sites (Fig. 2.S1).

In order to optimize the length of the serpentine path and achieve a high cell capture rate, we simulated the pressure and velocity field for various channel geometries. Fig. 2.S2 shows the simulation of the pressure and flow velocity under varying serpentine lengths ranging from 200 μm to 800 μm. Ideally, the larger the hydrodynamic resistance of the serpentine path is (R_S, which is proportional to the serpentine length) the higher the capture rate. However, when the serpentine length is longer than 800 μm, the hydrodynamic resistance of the serpentine path (R_S) becomes so large that the flow velocity drops significantly. In this case, cells may get stuck along the serpentine path resulting in clogging. As a result, there is a large standard deviation of capture rates observed in chips with very long serpentine lengths (Fig. 2.1 (D)). A similar problem arises under gravity flow when many more than 20 migration channels are incorporated (data not shown). To further optimize the cell capture rate in this asymmetric capturing design, the media volume in the right inlet during loading (80 μL) is slightly less than that in the left inlet (100 μL). The resulting weak gravity flow rightward into the migration channel guides the cells closer to the capture site to increase the capture probability. From simulations, the optimal serpentine length was determined to be 600 μm, to achieve high capture rates of over 94% (capturing nearly exactly one cell per each migration channel) (Fig. 2.1 (D)). A video demonstrating the cell capturing process can be found at https://youtu.be/_2TGZMbfnLE.

The stiffness of the cells of interest is also critical for optimal cell capture. More elastic cells yield higher capture rates since they deform more easily and plug the central path, sealing the capture site better than stiffer cells do. Based on the particular cancer cell types used in the experiments, the geometry of serpentine lengths and path openings were modified to improve capture efficiency, as described in more detail in the supplementary methods. Extensive studies were performed on various cell types including SKOV3, A2780DK, C2C12, MDA-MB-231, and PC3 cell lines, and we have achieved capture rates greater than 85% in all the tested cell types (Table 2.1). These experimental data demonstrate that the proposed single-cell capture mechanism is reliable and robust for a broad spectrum of cell types, and thus amenable to the study of individual cancer cells' migration.

Chemical gradient generation

The migration of cancer cells can be driven by chemotaxis whereby differences in the concentration of growth factors or other chemokines can induce tumor cells to intravasate into the circulatory system.[42-44] To model this *in vivo* condition, the migration channels in our device (width: 40 μm, height: 10 μm, length: 1 mm) are designed to specifically study the movement of cells with a concentration gradient profile generated by diffusion.[45] To generate this chemical concentration profile, serum-free culture media with chemoattractant is pipetted into the right inlet and serum-free culture media is pipetted into the left inlet. Due to the nature of diffusion, the concentration of the chemoattractant in the migration channels

increases linearly along the channel from left to right, as simulated in Fig. 2.S3. The generated chemical profile projected in the simulation was confirmed experimentally using a fluorescent dye (Fluorescein 5(6)-isothiocyanate, F3651, Sigma-Aldrich). The fluorescent intensity was measured and plotted in Fig. 2.1 (E). The measured fluorescent concentration profile agrees with simulation results (COMSOL 3.5), verifying that concentration profiles can be successfully generated. Additional simulations were performed to investigate whether a migrating cell in the channel would affect the gradient profile. A pseudo-cell (10 μm width by 10 μm height and 40 μm length) was added to the model to simulate a potentially blocked channel. However, since the channel cross-section (40 μm by 10 μm) is much larger than that of a cell (10 μm by 10 μm), the gradient was only minimally changed (<2% difference), as shown in Fig. 2.S4.

Single-cell migration assay

Cancer metastases are caused by a multi-step process which begins with the escape of tumor cells from the primary tumor through the basement membrane and the subsequent intravasation of cancer cells into capillary vessels under the influence of chemoattractants and cellular signals generated by cell-cell junctions.[2,42] In order to validate the utility of the fabricated migration chip as an *in vitro* model of migration, we investigated the chemotaxis of SKOV3 ovarian cancer cells toward a higher concentration of hepatocyte growth factor (HGF), which is a well-known chemoattractant across many cell types.[46]

Fig. 2.2 illustrates the single-cell migration tests in the platform. After cell loading utilizing gravity-driven flow, all the captured SKOV3 cells were positioned at the capture sites along the left side, as shown in Fig. 2.2 (A). The captured cells attached to the substrate within three hours and chemotaxis was monitored over 24 hours at single-cell resolution, as shown in Fig. 2.2 (B). After cell loading, media in the right inlet was replaced with serum-free media supplemented with 50 ng/mL HGF, which induces SKOV3 cell migration.[47] Serum-free media without HGF was pipetted into the left inlet, creating a linear concentration gradient of HGF along the migration channel. After 24 hours, we observed that more cells migrated to the right side when exposed to the HGF concentration gradient, while under the control conditions (applying serum-free culture media to both inlets) the cells did not show any directional migration (Fig. 2.2 (A)). This increase in chemotaxis was dependent on HGF concentration and is plotted in Fig. 2.2 (C). These data demonstrate that our platform is suitable for studies relying on single-cell chemotaxis as a read-out.

Selective subpopulation harvesting for downstream cellular heterogeneity analysis

Cellular heterogeneity is a key characteristic of cancer. Subpopulations or even single cells in a primary tumor or within a cancer cell line may have their own distinct phenotype due to genomic mutations or differential genetic and epigenetic regulation.[1,29-31] In our single-cell migration platform, we can not only monitor the movement of each cell but also selectively harvest the highly

chemotactic and the non-chemotactic subpopulations for downstream analysis after the migration assay. This additional capability grants the opportunity to analyze the intrinsic differences within cell populations which contribute to the observed heterogeneity in motility.

Although MDA-MB-231 is an aggressive breast cancer cell line, some cells within this line exhibit yet a greater chemotactic potential than others in that we observe not all cells migrate equally toward a chemoattractant stimulant (data not shown). To understand the differences even within a traditionally presumed "homogenous" cell line that could lead to this phenotypic dissimilarity, we sought to collect and further characterize the highly chemotactic MDA-MB-231 population in comparison to the cancer cells that remained on the cell-loading side of the device and were not stimulated by the gradient to directionally migrate. After a migration assay using 10% fetal bovine serum as the chemoattractant, both highly chemotactic and non-chemotactic MDA-MB-231 cells were retrieved as illustrated in Fig. 2.3 (A-E). Fig. 2.3 (B) shows a highly chemotactic MDA-MB-231 cell, which had migrated all the way to the serpentine channel on the right side of the device within 24 hours. To selectively harvest these cell populations, we must use a different protocol than for cell seeding. For cell loading at the start of a migration experiment, we utilize only gravity-driven flow by adding 100 µL of cell-containing media into the inlets with no liquid in the outlets to achieve a pressure difference of around 50-100 Pa. For cell retrieval, trypsin is flowed from the outlets to the inlets, detaching and directing

chemotactic cells to the right inlet and the non-chemotactic cells to left inlet. Additionally, we apply a negative pressure of about 1,000 Pa via pipet bulb on the inlet reservoirs as trypsin flows from the outlet reservoirs. This pressure gradient generates a flow rate strong enough to overcome the slight diameter difference between a cell (~13 μm) and the central path capture site (20 μm x 10 μm) so that the cells deform and flow through the capture channel and toward the collecting inlets, without incurring damage. After 5 minutes of trypsinization under negative pressure, the target cell populations were detached, retrieved from the inlet, and then re-plated into 60 mm petri dishes for recovery and propagation (Fig. 2.3 (C, D, E)). After 12 hours of recovery, scanning electron microscope images of the retrieved cells revealed that the highly chemotactic cells were more elongated with a distinct mesenchymal morphology whereas the non-chemotactic cells were rounded with an epithelial-like morphology (Fig. 2.3 (F,G)).[48-50]

In order to evaluate the two populations further, we allowed the harvested cells to grow in tissue culture for 4 days after retrieval. The collected cells grew into distinct colonies each containing about 30-40 cells as shown in Fig. 2.4 (A, B, D). We found that the harvested highly chemotactic cells maintained their mesenchymal morphology, even after forming a colony over 4 days, while in comparison, the non-chemotactic cells remained tightly clustered and epithelial in appearance (Fig. 2.4 (A, B)). In the chemotactic colonies, all daughter cells were also spread over a larger area than those in colonies formed by non-chemotactic cells. There was a significant difference in the colony radius between the two

groups (Fig. 2.4 (C)), with no observed difference in the proliferation rate (Fig. 2.4 (D)). The cells of a chemotactic colony also had significantly greater aspect ratios than cells in a non-chemotactic colony, indicating maintenance of the mesenchymal and epithelial morphologies, respectively (Fig. 2.4 (E)).

To examine whether the difference in chemotaxis was maintained after cell retrieval and culture, single-cell migration assays were performed on the daughter cells from the chemotactic and non-chemotactic clusters. Despite only having a limited (<1,000) number of descendant cells from the even smaller number of harvested chemotactic and non-chemotactic cells, our single-cell migration chip could efficiently handle such limited quantities due to a high capture efficiency. The progeny of the highly chemotactic cells remained significantly more migratory than those of either the harvested non-chemotactic cells or the non-migration-sorted bulk population (Fig. 2.4 (F)), while no significant difference was observed between the descendants of the non-chemotactic cells and unsorted MDA-MB-231 cells. These results demonstrate that the distinct characteristics of sorted cells are maintained after the harvesting and limited propagation process, allowing further studies on the differences between these highly chemotactic and non-chemotactic cells to be reliably interpreted.

Taking advantage of this fact and to further ascertain what molecular differences between these two populations within the same cell line might account for their

different migration behavior, we harvested the chemotactic and non-chemotactic populations from a separate set of migration devices and cultured them for 4 days as before. We then isolated RNA from the chemotactic and non-chemotactic cells as well as from bulk MDA-MB-231 cells plated in the similar numbers to the quantity harvested from the migration devices. We performed RT-qPCR on samples from 3 separate chemotaxis-sorting experiments and found that the chemotactic cells expressed significantly higher amounts of RhoC GTPase and p38γ mRNA as compared to the non-chemotactic cell population that remained on the cell-loading side of the device (Fig. 2.4 (G)). Both of these proteins have been shown in previous studies to be important mediators of cancer cell motility and higher expression correlated with advanced cancer stage and worse prognosis.[38,51-54]

Customized migration channel for mimicking lymphatic capillary geometry

Capillary intravasation is a critical step in the metastasis of cancer to the lymph nodes,[3] yet limited devices at present allow for the ideal *in vitro* study of this process.[15] To address this gap, we designed a device with migration channels with a series of choke points in order to mimic the geometric constraints of lymphatic capillaries within our migration chip.[26]

In previous work, we studied mitogen activator of protein kinase (MAPK) family member, p38γ, which has a known role as a motility regulator in aggressive breast cancer cells.[38] In that study, MDA-MB-231 breast cancer cells transfected

with shRNA targeting the p38γ isoform, p38γ knockdown (GKD) cells, had a rounded morphology and decreased or eliminated mesenchymal migration. These cells were more epithelial and had dysfunctional actin cytoskeleton cycling leading to ineffective random walk in 2-dimensional migration when compared to cells transfected with a scrambled shRNA control plasmid (SCR).[38] Importantly, these results had been modeled previously by us *in silico* and, for the p38γ knock-down cells, the endpoint of decreased lymph metastases have been observed *in vivo*. Now, we wished to test whether our newly developed device in our present work would reliably approximate lymphatic invasion as a rapid and convenient *in vitro* mimic. Thus, to characterize the migration capability of MDA-MB-231 breast cancer cells in a 3D geometric model of lymphatic capillaries, we altered our single-cell migration chip to contain multiple migration resistance choke points (Fig. 2.5 (A,B)) and successfully demonstrated the capability of tracing single cells in this lymphatic capillary invasion assay (Fig. 2.5 (C,D)). The size variation of the migration channels and choke points are illustrated in Fig. 2.5 (B) and represent the continuum of mechanical stresses a cancer cell would encounter *in vivo*, with the narrowest choke point corresponding to the average diameter of lymphatic vessels draining to axillary lymph nodes.[26-28]

The qualitative effects of p38γ knockdown on migration through choke points can be seen in Fig. 2.5 (C). Fig. 2.5 (C) shows the representative morphologies of the scrambled vector (SCR) cells and p38γ knockdown (GKD) cells within the narrowest choke point channels (6 μm x 10 μm). F-actin fibers are labeled with

red fluorescence protein (RFP) and stably transfected cells are labeled with green fluoresecence protein (GFP) through their respective expressing plasmids. SCR cells are able to form long pseudopodia that can reach past the choke point in a mesenchymal-like manner to form an attachment beyond the narrowing; thus, these cells are successful in migrating through the lymphatic-capillary mimics by contraction of their stress fibers in the typical “rubber band-like” fashion (Fig. 2.5 (C)). In contrast, the GKD cells ineffectively cycle their cytoskeleton in a basket-weave configuration, as demonstrated previously,[38] and thus are only able to squeeze into the narrow channel but can travel no further, with the actin evenly distributed around the periphery of the cell (Fig. 2.5 (C)).

To quantify this observation further, we measured the cell migration distance (as a function of “passed choke points” or relative distance in the channels) for multiple choke point geometries, as plotted in Fig. 2.5 (D). We observed that SCR and GKD cells have equivalent chemotactic potential in response to a serum gradient when the migration channel is wide (30 μm x 10 μm) and without choke points, but the number of traversed choke points of GKD cells significantly diminishes when the migration is obstructed by the narrowest choke points (6 μm x 10 μm). To verify the decreased migration efficiency of p38γ knockdown cells, the migration velocity of MDA-MB-231 cells in the narrowest choke point channels was measured and shown in Fig. S5. While the variation is large, the migration velocity of SCR cells is almost double that of GKD cells. This result supports the hypothesis that the motility of GKD cells is decreased due to

unproductive actin cytoskeletal cycling as previously reported,[38] but also allows, for the first time, direct visualization of what might be happening *in vivo* at the critical intravasation step for lymph node metastases that caused the GKD cells to have decreased contralateral lymph node metastases in mice.[38]

Discussion

Many microfluidic devices for cell migration have been reported in recent years.[14-16,25,32-37,40,41] Although multiple approaches have been designed to exploit the advantages of microfluidics (small volumes and precise micro-environment control), most assays still measure an average behavior over large numbers of cells with an underlying implicit assumption that all cells are essentially identical. However, as cellular heterogeneity is increasingly recognized as a key aspect of the evolution of cancers and of the genesis of inherent resistance to treatment and recurrence,[29] there is a need to leverage microfluidics for the study of tumor heterogeneity. In this work, we have developed, characterized, and tested a tool that has the capability to select highly chemotactic cells for study and to enable their recovery for further characterization of this subpopulation's differences from its non-chemotactic counterpart population. Given that only certain cells within a tumor are the key metastases-initiating cells,[1,2] we anticipate that this tool has the potential to greatly advance our detailed molecular studies of the multiple cellular subpopulations comprising a primary or a metastatic tumor. Understanding specific differences that lead some cancer cells to successfully bypass the

metastatic sieves and leave the primary tumor and seed metastases is of great benefit to develop and test anti-metastatic strategies. Here, we demonstrated single-cell migration and investigation of the individual chemotactic profile of each cell rather than their average aggregate behavior. Moreover, following the assays, cell populations of different chemotactic potential extremes were selectively retrieved for further downstream analysis to better query the inherent differences in these subpopulations.

The presented migration device reliably positions exactly one cell next to the migration channel, granting the advantages of using a small number of cells and allowing for easy tracing of single-cell migration behavior. We incorporated a hydrodynamic scheme within the migration channel that, through optimization, achieved near an 85% capture rate in 5 different mammalian cell lines. In order to achieve this high single cell capture efficiency, precise control of the hydrodynamic resistances was necessitated not just for the individual channel subsections (serpentine channel vs. central channel) but also across the whole migration device. When more than 20 migration channels (and thus 20+ serpentine channels and 20+ central channels) were incorporated, the gravity-driven flow rate with the volumes used for cell seeding was too slow and cell clogging occurred. However, even with just 20 migration channels, the assays can be performed on the limited inputs of cells as demonstrated by our post-assay recovery and re-assessment of migration properties of less than 1,000 cells. In addition, a chemoattractant gradient can be reliably generated in the

narrow migration channels with a limited effect on the concentration profile by a migrating cell.

Using the described platform, we have successfully demonstrated three single-cell migration assays: tracing SKOV3 cell chemotaxis induced by HGF, determining molecular differences between the highly chemotactic and non-chemotactic populations of MDA-MB-231 breast cancer cells, and studying a metastasis-related gene (p38γ) by evaluating its effect on cancer cell migration through channels mimicking the geometric constraints of lymphatic capillary intravasation. Our prior work revealed the differences between GKD and SCR cells in their actin cytoskeleton oscillations and random-walk migration via computer modeling and demonstrated reduced lymphatic metastases *in vivo* in mice.[38] With our newly developed single-cell migration chip, we are able to directly visualize how the GKD cells are mechanically less capable of lymphatic intravasation. This experiment demonstrated the potential of the proposed single-cell platform for studying models of cell migration *in vitro* in devices that can geometrically mimic critical steps in the metastatic process and the ability to discern cellular motility differences as a result of specifically induced or native signaling characteristics. Furthermore, evaluation of the motility and indirect metastatic potential of certain cell fractions *in vitro* has the potential to enable targeting specific cell subpopulations *in vivo* so as to eliminate them preferentially before they may have a chance to metastasize.

Our platform also provides a method for chemotactic-based selection. Highly chemotactic and non-chemotactic cells were selectively retrieved after the migration assay for further propagation and analysis. While a previously reported device also allows for the chemotactic selection of cells,[16] this device suffers from the necessity of loading thousands of cells precluding its potential use with small tumor biopsy samples. Utilizing our device and with loading only hundreds of cells, we demonstrate that the distinct characteristics of migration-sorted cells are maintained after harvesting and limited expansion in tissue culture. This allows for reliable interpretation of further downstream studies to distinguish the differences between the highly chemotactic and non-chemotactic cell populations within a given "homogenous" sample. Thus, the present platform provides the capability to correlate the migration phenotype of the highly chemotactic cells with a molecular signature of gene expression within this subpopulation. Although a recent study demonstrated poor correlation between the speed of mother and daughter cells in the immediate 6 hours after cell division, this was for cells from the entire spectrum of migration speeds.[14] In our work, we select for the highly chemotactic subpopulation and show that for these cells this migration and mesenchymal morphology phenotype is heritable, at least over limited generations. Furthermore, this same population of cells also expresses greater amounts of mRNA of two known migration and metastasis-associated genes, RhoC and p38γ, than the non-chemotactic subpopulation does.[38,51-54] Therefore, our present device has the capability of selecting cancer cells based upon their chemotactic phenotype and then enabling the harvest and assessment of what

molecular underpinnings might be responsible for the difference in chemotaxis. We believe our study sets the stage for the investigation of motility heterogeneity and metastatic potential within cancers on a broader scale and can yield new insights as to the mechanical and molecular basis of why certain tumor cells in a patient are able to metastasize.

Materials and Methods

Device Fabrication and Assembly

The migration devices were formed from a single layer of PDMS (polydimethlysiloxane), which was fabricated on a silicon substrate by standard soft lithography, and a glass slide. Three masks were used to fabricate the multiple heights for the serpentine channel region (40 µm height), the capture gap (20 µm height), and the migration channel (10 µm height). Channel widths were 40 µm unless otherwise stated (choke points and central path). The PDMS layer was bonded to the glass slide after activated by oxygen plasma treatment (80 Watts, 60 seconds) to form a complete fluidic channel. Before cell loading, collagen (Collagen Type 1, 354236, BD Biosciences) solution (1.45mL Collagen, 0.1mL acetic acid in 50mL DI Water) was flowed through the device for one hour to coat collagen on the substrate to enhance cell adhesion. Devices were then rinsed with PBS (Gibco 10082) for one hour to remove the residual collagen solution before use.

Cell Culture

SKOV3 (ovarian cancer) and A2780DK (ovarian cancer) cells were obtained from Dr. Ronald Buckanovich's lab (University of Michigan, MI, USA) and cultured in RPMI (Gibco 11875) with 10% FBS (Gibco 10082) and 1% penicillin/streptomycin (Gibco 15140). PC3 (prostate cancer) cells were obtained from Dr. Ken Pienta's lab (University of Michigan, now at Johns Hopkins University) and cultured in DMEM (Gibco 11965) with 10% FBS and 1% penicillin/streptomycin. MDA-MB-231 (breast cancer) cells were cultured in RPMI with 10% FBS and 1% penicillin/streptomycin. Cells were cultured at 5% CO_2. The p38γ knockdown MDA-MB-231 (GKD) cells were stably transfected in the Merajver lab with short hairpin RNA (shRNA) targeting p38γ and the scrambled vector (SCR) cells were transfected with a scrambled hairpin RNA as previously reported.[45]

Single-cell Migration Assay

Cells were harvested from culture plates with 0.05% Trypsin/EDTA (Gibco 25200) and centrifuged at 1000 rpm for 5 min. To improve the imaging quality, cells were stained by green fluorescent (Invitrogen, Cell tracker Green C2925) dye. Then, the cells were re-suspended in culture media to a concentration of $1x10^5$ cells/ml. 100 µL of this cell solution was pipetted into the left inlet, and 80 µL of media only was pipetted into the right inlet. After 10 minutes, the cell solution in the left inlet was replaced with 100 µL serum-free culture media, and 100 µL serum-free media with the indicated chemoattractant was applied to the other inlet to induce chemotactic migration. Then, the entire chip was put into a

cell culture incubator. Migration distance was measured based on the final cell position after 24 hours of incubation without media replenishment. Only the migration channels having single cells were counted. The velocity of cells was measured by imaging cell positions every 30 minutes. Results presented represent means ± standard deviations. A two-tailed student t-test (unpaired) was used to measure significance.

Selective Subpopulation Retrieval

We selectively harvested the chemotactic and non-chemotactic cells after a 24 hour migration assay. The cells that remained in the left side (loading side) were considered non-chemotactic cells, while the cells that had migrated the entire 1 mm migration channel to the right side (chemoattractant side) within 24 hours were considered highly chemotactic cells (Fig. 2.3(A)). To avoid possible contamination, both the inlets and outlet were washed carefully with trypsin before cell harvesting. 100 µL of PBS was pipetted into the outlet and left for 5 minutes to wash away any residual serum or debris in the channel. Trypsin was then pipetted into each outlet and flowed from the outlet to the inlet for 5 minutes. In this manner, the highly motile cells were trypsinized and directed to the right inlet, while the non-motile cells were directed to the left inlet. A slight negative pressure (~1,000 Pa) was also applied to each collecting inlet to prevent cell capture by the central paths since with this increased flow rate the cells overcame the slight difference in diameter and deformed and flowed through the central path. The detached cells were pipetted into a 60 mm petri dish or 96-well

plate for recovery and propagation. As cells plated at an ultralow density (~ tens of cells) have poor viability, we cultured these cells in MDA-MB-231 conditioned media. Conditioned media was obtained by culturing 3 mL of RPMI supplemented with 10% FBS on a 80% confluent layer of MDA-MB-231 in a 60 mm dish for one day prior to harvesting. Three consecutive 10-minute, 2,000 rpm centrifuging processes removing and re-centrifuging the media supernatant were performed to remove possible cellular contamination from the conditioned media once it was removed from the cell conditioning plate. The triple-centrifuged conditioned media was further plated alone and cultured in an incubator as a control to verify that no residual MDA-MB-231 cells were introduced into our chemotactic and non-chemotactic cultures.

RNA Isolation and RT-qPCR

After selective subpopulation retrieval, the harvested chemotactic and non-chemotactic cells were plated into 96-well plates for 4 days of culture. MDA-MB-231 cells that had not been migration-sorted were plated in equal densities to the chemotactic and non-chemotactic populations and used as bulk control. Biological replicates were harvested from 3 separate migration sortings each comprising at least 10 devices. RNA was extracted using the Single Cell RNA Isolation Kit (Norgen Biotek Corp, Cat. 51800) according to the manufacturer's standard protocol. RNA was eluted in 9 µL. The cDNA was prepared using the Reverse Transcription System (Promega, Cat. A3500) according to the standard protocol using Oligo(dT) primers and the entirety of the harvested RNA (~7 µL)

was used in each 20 µL cDNA reaction. The reaction was incubated at 42°C for 45 minutes then inactivated at 95°C for 5 minutes before storing at -20°C until use. Template dilutions of the 20 µL cDNA reactions were made by mixing 10 µL of cDNA with 10 µL of RNase/DNase free water. Qiagen QuantiTect SYBR Green PCR Kit (Cat. 204143) was used for the qRT-PCR reaction according to the standard manufacturer's hot-start protocol. Primers were purchased from Integrated DNA Technologies: RPL22 (Hs.PT.51.607028), RPL30 (Hs.PT.51.3119226), RhoC (Hs.PT.56a.39081600), and p38γ (Hs.PT.58.45504579). Primers were diluted into 500 µL of TE buffer (20x). Each 20 µL reaction well contained 10 µL of mastermix, 8 µL of water, 1 µL of the 1:2 diluted cDNA, and 1 µL of 20x primer. Triplicate technical replicates were performed on each gene for each of the triplicate biological replicates. The reaction was run on a StepOnePlus Real-Time PCR System (Applied Biosystems) with melt curve analysis for specificity of products. Results were analyzed with REST 2009 software using both RPL22 and RPL30 for normalization and with 5,000 iterations.[55]

Statistical Analysis

Two-tailed, unpaired student's t-tests were used for all comparisons with a significance level of 0.05 considered statistically significant. For RT-qPCR results, REST 2009 analysis software was used to assess significance using both RPL22 and RPL30 for normalization and with 5,000 iterations.[55] Results are presented as mean ± SD.

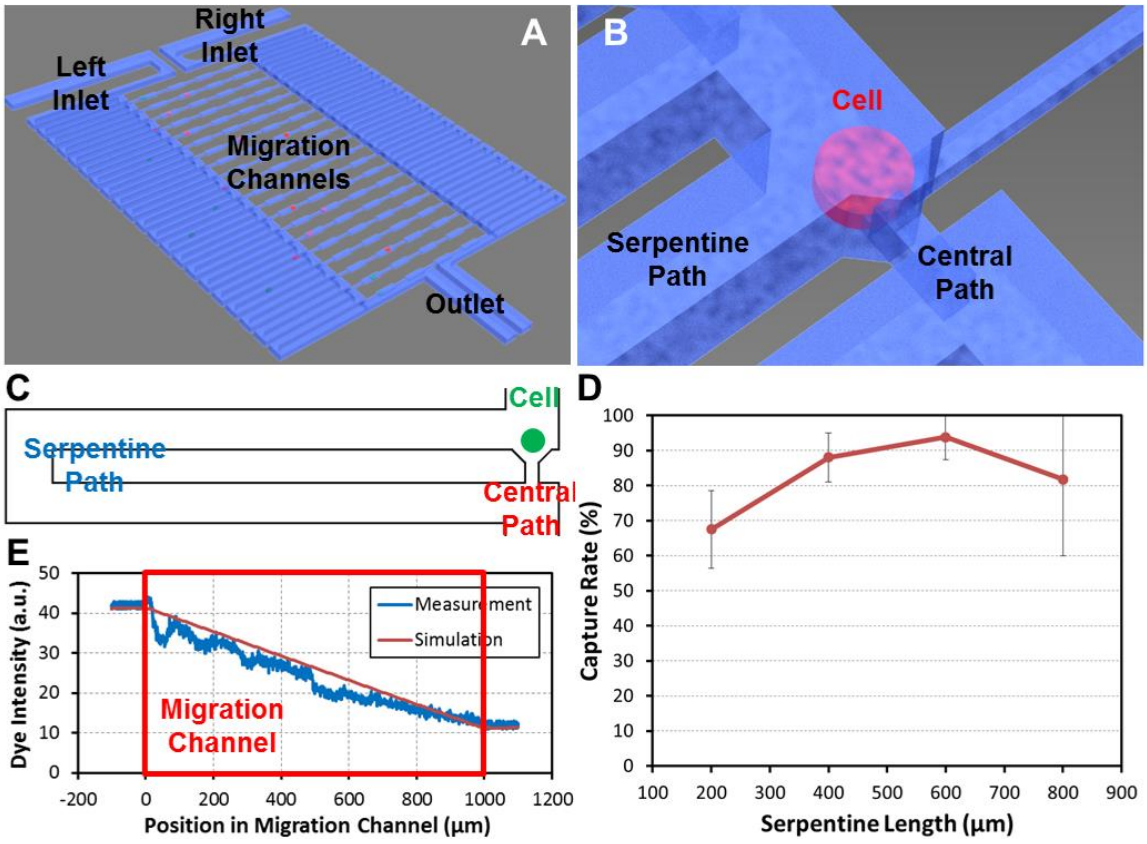

Figure 2.1. Proposed microfluidic chip for single-cell migration. (A) 3D schematic drawing of the chip. The cells are loaded in the left side, and the chemoattractant induces the migration through the migration channels toward the right. (B) Enlarged 3D schematic drawing of one cell capture site. (C) Schematic of the cell capture principle. (D) SKOV3 cell capture rate with different serpentine lengths (N= 4 devices). The optimal length determined from these experiments was 600 μm. (E) Concentration gradient of chemicals in the migration channel. The red line indicates the simulation result by COMSOL 3.5. The blue line is the measurement of the fluorescent dye intensity in the migration channel.

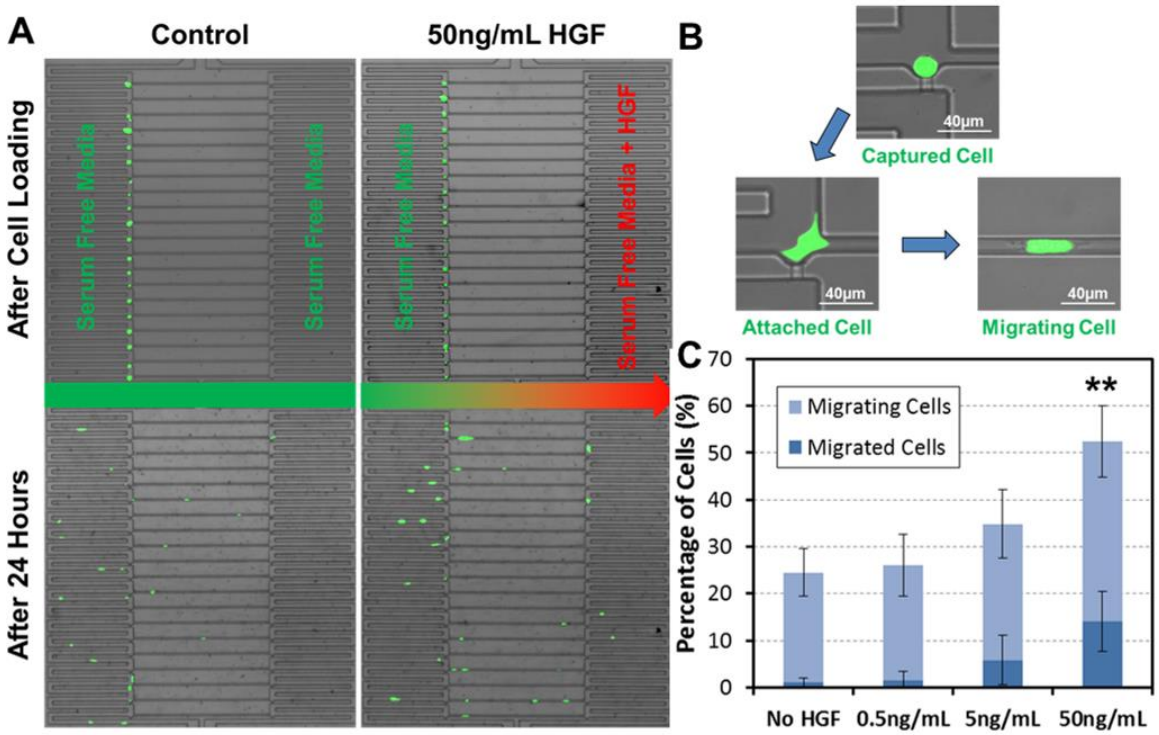

Figure 2.2. Single-cell migration assay using HGF as a chemoattractant for SKOV3 cells. (A) The images of the single-cell migration assay. The upper two images illustrate the single-cell distribution after cell loading (cells were loaded from the left channel). All captured cells are aligned along the left side of the migration channels. The lower two images illustrate the cell distribution after 24 hours without a chemoattractant (lower left, control) and with 50ng/mL of HGF in serum-free media added to the right inlet (lower right, stimulated). Compared to the control, the HGF induced cells to migrate further to the right. (B) The process of cell migration. First, a cell is captured by the hydrodynamic force from the cell solution. After 4-6 hours the cell attaches to the substrate and then it begins to move into the migration channel. (C) Result of the chemoattractant assays. The graph illustrates the relative ratio of migrated cells (all the way to the opposite side) and migrating cells (within the channel) vs. HGF concentration. The result confirms that the HGF is a strong chemoattractant for the SKOV3 cells. Data points represent means ± standard deviations (N= 4 devices), ** refers to $P < 0.01$ compared to the no HGF control.

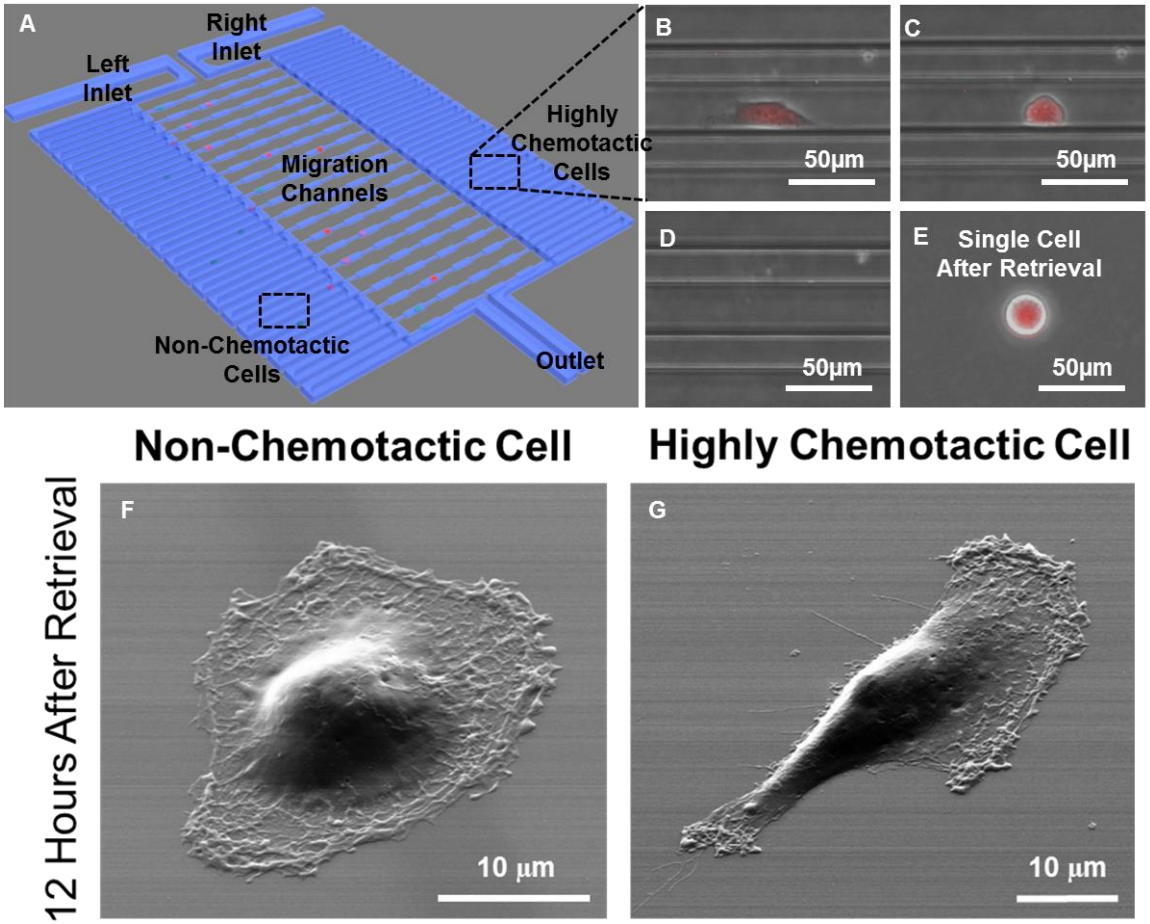

Figure 2.3. Selective retrieval and downstream analysis of the highly chemotactic cells. (A) The schematics for cell retrieval. (B) A representative highly chemotactic cell, which has migrated completely through the migration channel within 24 hours. (scale bar: 50 μm) (C) After 3 minutes of trypsinization, the cell became rounded in morphology. (scale bar: 50 μm) (D) After 5 minutes of trypsinization, the cell was successfully detached and flowed to the right inlet. (scale bar: 50 μm) (E) All detached cells were transferred to a 60mm petri-dish or 96-well plate. (scale bar: 50 μm) (F) Scanning electron microscope image of a non-chemotactic cell exhibiting epithelial morphology 12 hours after retrieval. (scale bar: 10 μm) (G) Scanning electron microscope image of a highly chemotactic cell exhibiting mesenchymal morphology 12 hours after retrieval. (scale bar: 10 μm)

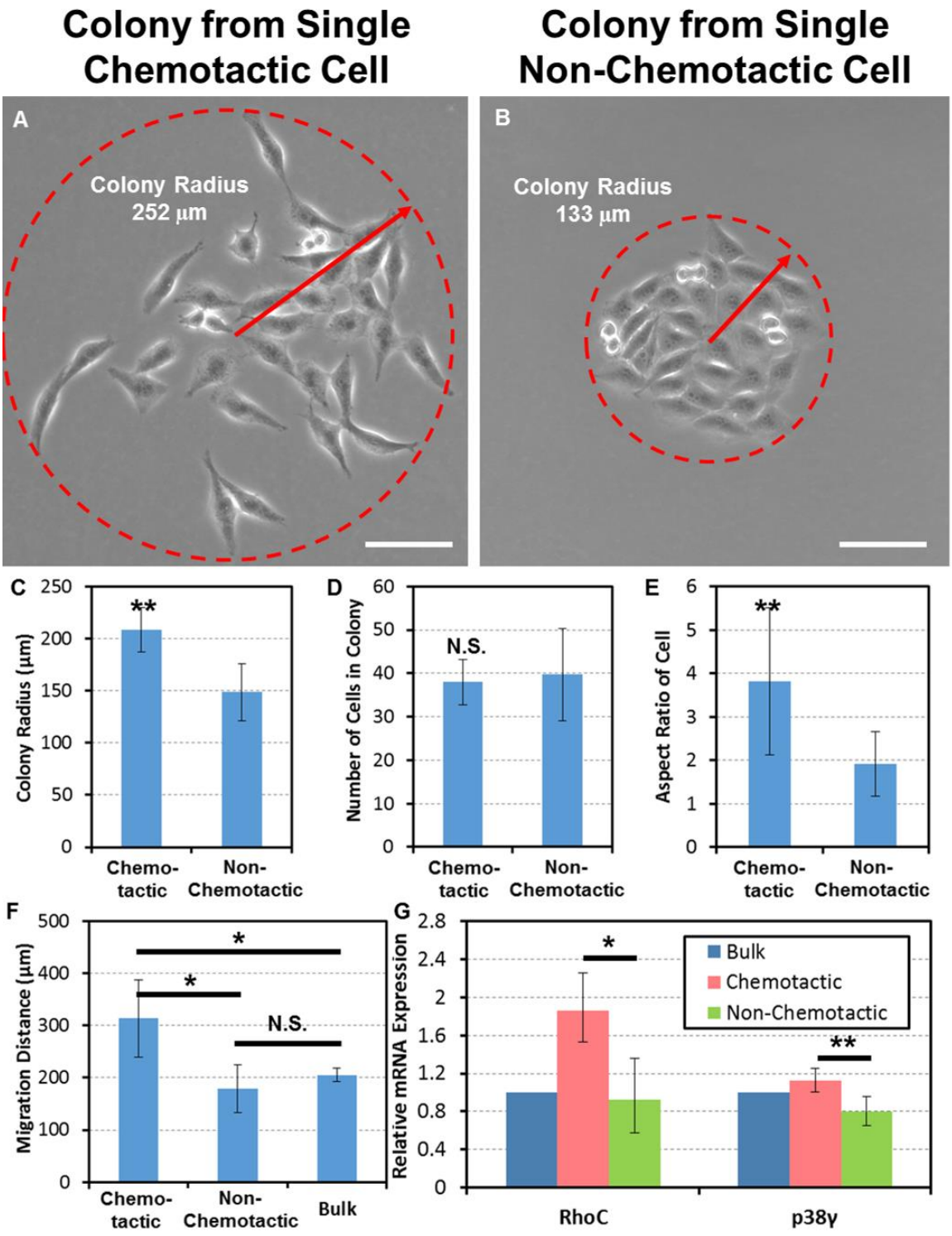

Figure 2.4 Characterization of the highly chemotactic subpopulation. (A) The colony formed by a single chemotactic cell after 4 days. The cells in the colony maintained an elongated (mesenchymal-like) shape and spread over a wide area. (scale bar: 100 μm) (B) The colony formed by a single non-chemotactic cell after 4 days. The cells were epithelial in morphology and tightly clustered. (scale bar: 100 μm) (C) The comparison of the colony radius between

the highly chemotactic and non-chemotactic cell colonies. The colonies formed by chemotactic cells have a significantly larger radius (N = 8 colonies), ** refers to $P < 0.01$. (D) The comparison of the number of cells per colony between the highly chemotactic and non-chemotactic cell colonies. No significant difference was observed. (N = 8 colonies) (E) The descendant cells from chemotactic cells exhibit a significantly higher aspect ratio 4 days after retrieval, indicating persistence of the mesenchymal-like morphology (N = 8 colonies), ** refers to $P < 0.01$. (F) The migration distance of repeated single-cell migration assays. Descendants of highly chemotactic cells persisted to be more migratory than the descendants of non-chemotactic cells and the unsorted bulk MDA-MB-231 cells (N = 5 devices), * refers to $P < 0.05$. (G) The chemotactic cells exhibited a higher expression of mRNA as analyzed by qRT-PCR of the migration and metastasis-associated genes RhoC and p38γ as compared to non-chemotactic cells; * refers to $P < 0.05$, and ** refers to $P < 0.01$, respectively.

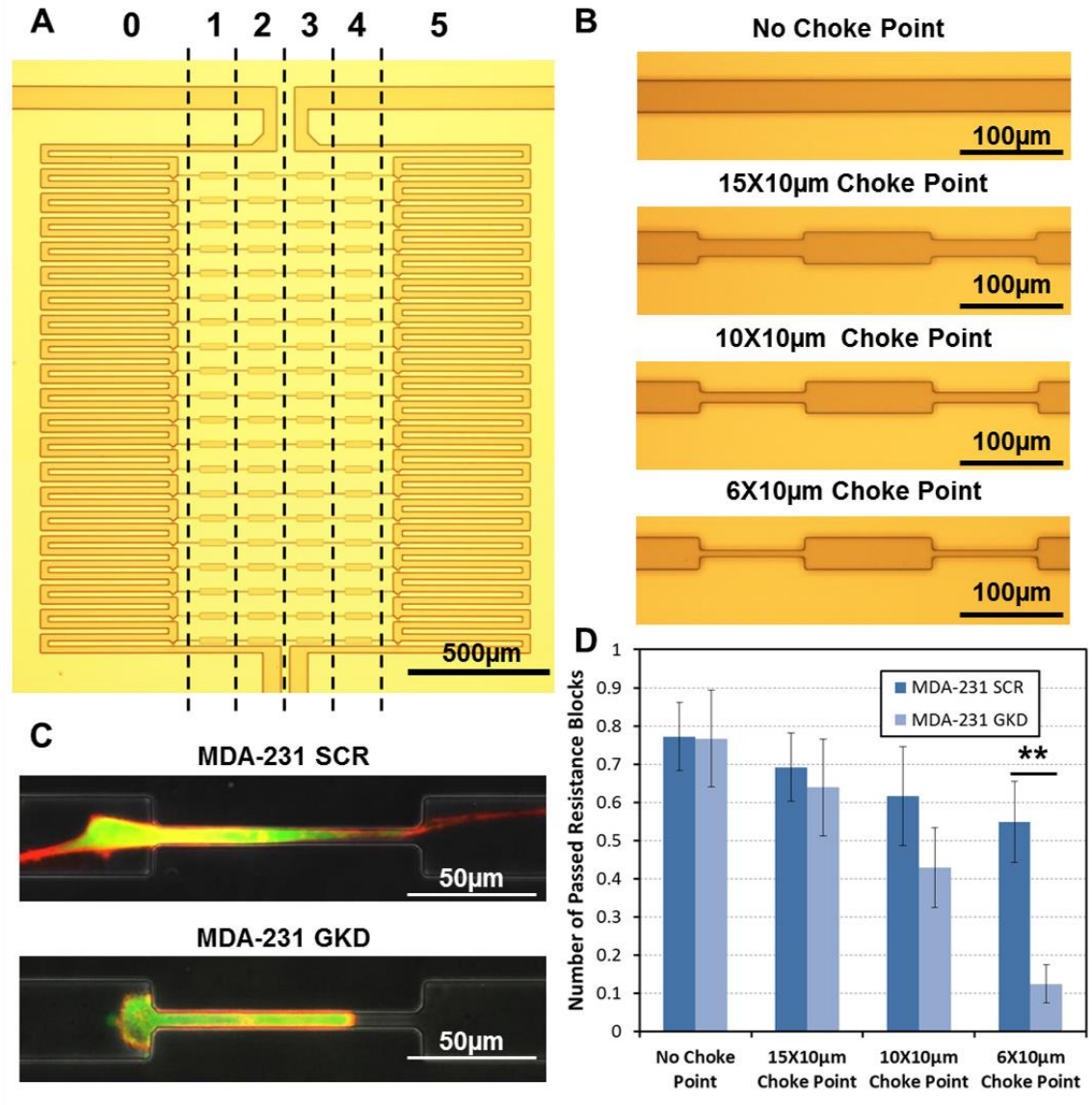

Figure 2.5. Customized migration channels for mimicking lymphatic capillary geometry. (A) Photomicrograph of the fabricated device. (B) Size variation of migration channels. The length of choke point is 100 μm, and the width of choke point varies from 6 μm (narrowest) to 30 μm (no choke point). (C) Qualitative observation of migration behavior of MDA-MB-231 cells in the 6 μm x 10 μm choke point. The scrambled control (SCR) cells can form a stable and long stress fiber to migrate through the choke point, while the p38γ knockdown (GKD) cells can only squeeze into the choke point. F-actin is labeled by RFP and GFP is expressed by the targeted or scrambled shRNA plasmid. (D) Single-cell migration assay on different channel geometries. The motilities of both cells are similar in the straight channels, but the SCR MDA-MB-231 cells are far more motile in narrower choke point channels. Data points represent means ± standard deviations (N = 8 devices), ** refers to $P < 0.01$.

	Cell Type	Capture Rate
Skov3	Ovarian cancer	93.8±6.4 %
A2780DK	Ovarian cancer	88.6±10.2 %
C2C12	Mouse muscle myoblast	92.2±4.5 %
MDA-MB-231	Breast cancer	91.5±7.2 %
PC3	Prostate cancer	85.1±9.7 %

Table 2.1. Capture rates of five cell lines. (N = 4 devices)

Supplemental Figures

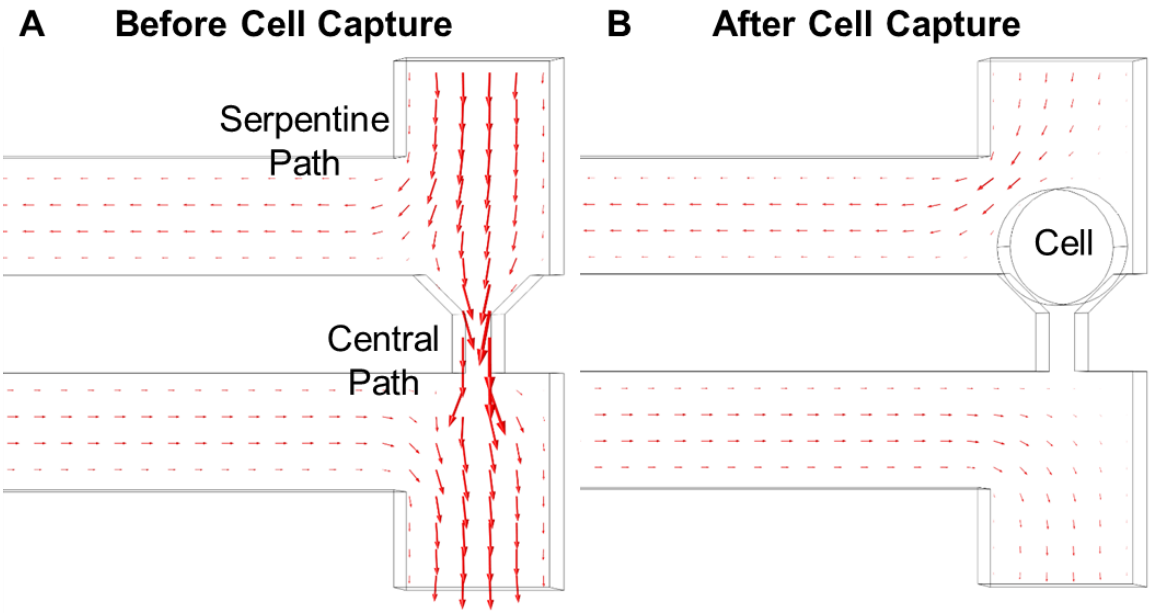

Figure 2.S1. Simulations of flow velocity before and after capturing one cell by COMSOL 4.3. (A) Before cell capture, simulation of flow velocity shows that the higher flow rate through the central path, so the cells will more likely follow the central path. (B) After capturing one cell, the captured cell plugs the gap and blocks the flow through the central path. Thus, the rest of the cells will travel through the serpentine path and will be subsequently captured in the downstream capture sites.

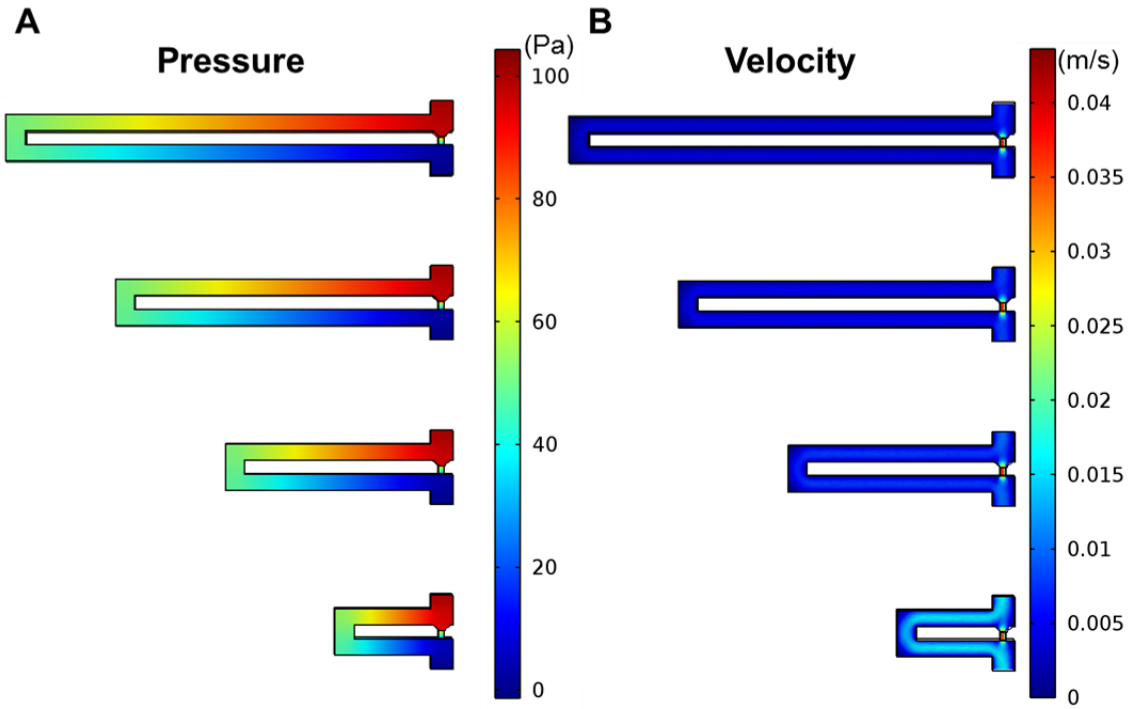

Figure 2.S2. Simulations of flow velocity and pressure on different serpentine lengths ranging from 200 μm to 800 μm by COMSOL 4.3. (A) Simulations of pressure distribution illustrates that the quick transition in the capture site leads to a high capture probability of single cells at the site. (B) Simulations of flow velocity indicates that when the serpentine structure is short, the flow rate through serpentine path becomes higher, which means that the cell is less likely to be driven to the capture gap.

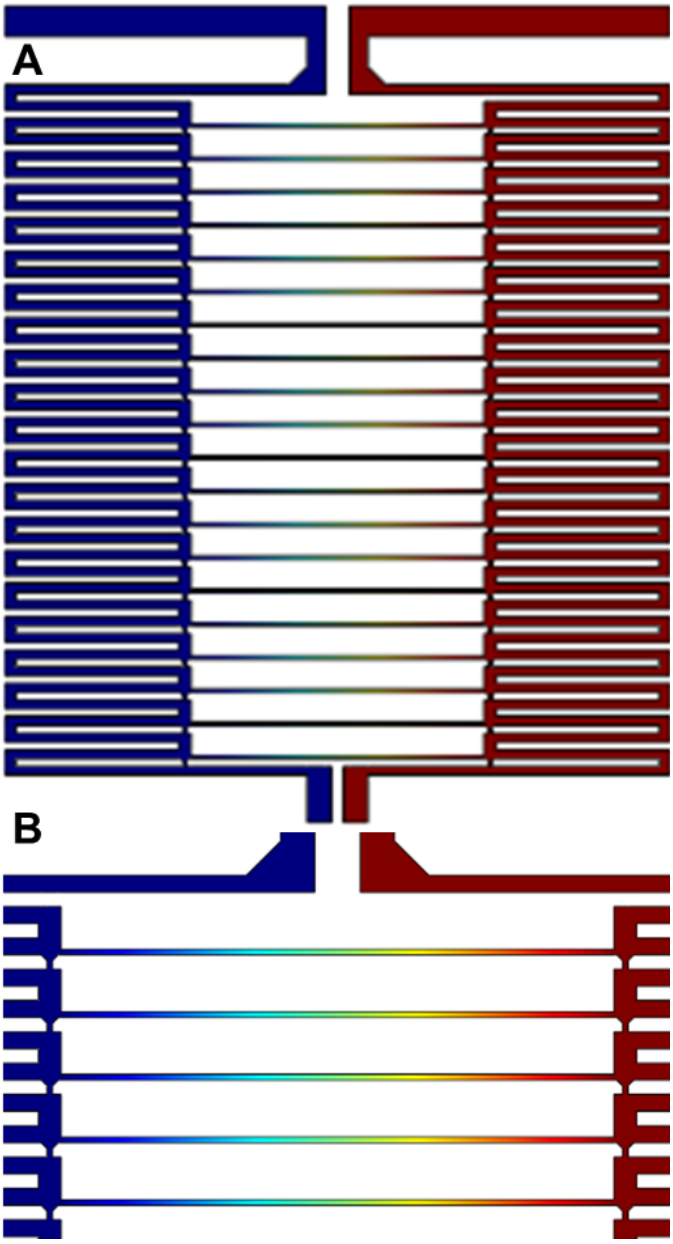

Figure 2.S3. Simulations of chemical concentration gradient generated in the device by COMSOL 3.5. (A) The simulation of the whole chip demonstrates that the chemical concentration is uniform from the upstream to the downstream channels since the diffusion is relatively slow. (B) Enlarged view of the first few channels. The simulated concentration profile shows the linear chemical gradient is formed in the migration channel. Concentrations are shown in color scale with red being 1 M chemokine and blue being 0 M chemokine.

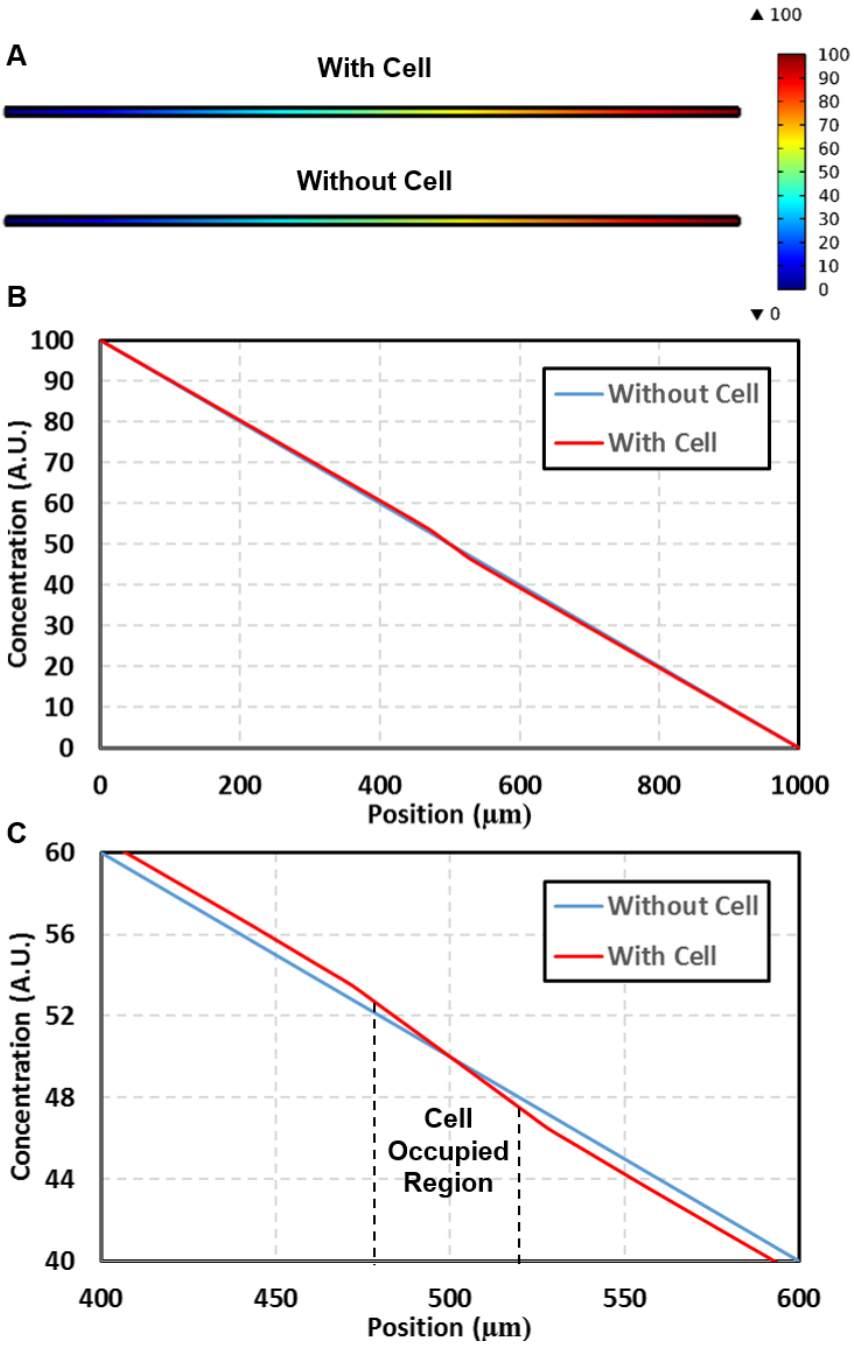

Figure 2.S4. Simulations of chemical concentration profile with and without cell migrating in the migration channel. (A) The simulation of the chemical concentration profile with and without cell migrating in the migration channel. The cell was emulated by adding a pseudo-cell (10 μm width by 10 μm height and 40 μm length) on the bottom of the channel to block diffusion. The cell was placed at the center (500 μm from the left) (B) The concentration profile in the channel. (C) Enlarged concentration profile in the channel from the 400 μm to 600 μm position. Since the channel cross-section (10 μm by 40 μm) is much larger than cell, the concentration is altered by less than 2%.

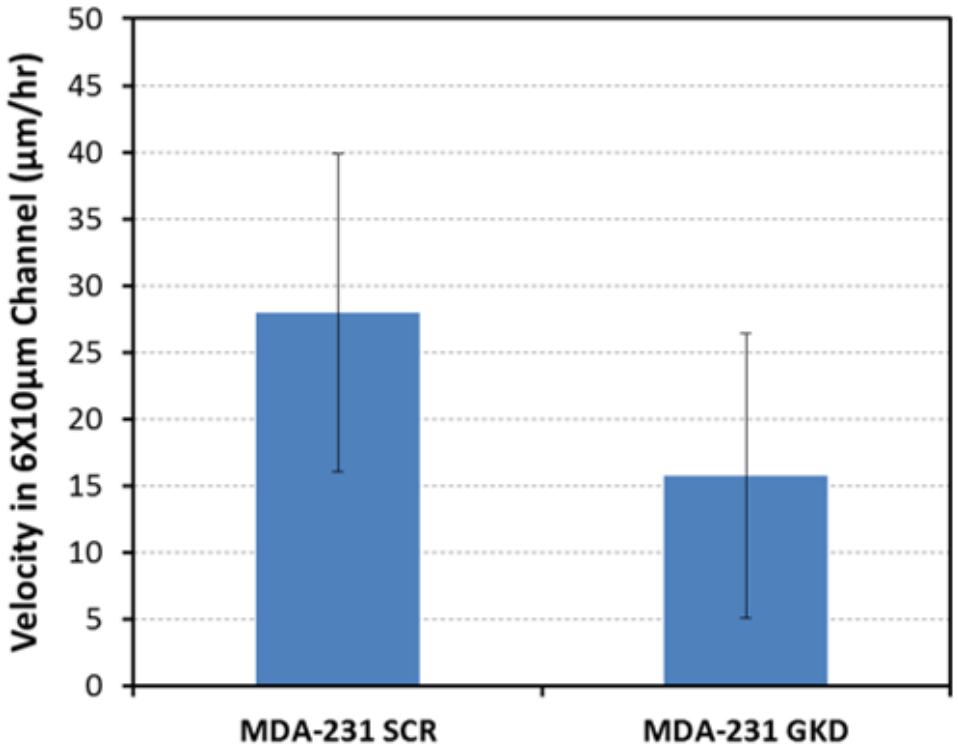

Figure 2.S5. The migration velocity of MDA-MB-231 cells in the 6 µm x 10 µm choke points. The scrambled control (SCR) cells can migrate more efficiently than the p38γ knockdown (GKD) cells through the choke point.

References

1. Hanahan, D. & Weinberg, R. A. Hallmarks of cancer: the next generation. *Cell* **144**, 646-674, (2011).
2. Steeg, P. S. Tumor metastasis: mechanistic insights and clinical challenges. *Nat Med* **12**, 895-904, (2006).
3. Nathanson, S. D. Insights into the mechanisms of lymph node metastasis. *Cancer* **98**, 413-423, (2003).
4. Sethi, N. & Kang, Y. Unravelling the complexity of metastasis - molecular understanding and targeted therapies. *Nat Rev Cancer* **11**, 735-748, (2011).
5. Yoshida, B. A., Sokoloff, M. M., Welch, D. R. & Rinker-Schaeffer, C. W. Metastasis-suppressor genes: a review and perspective on an emerging field. *J Natl Cancer Inst* **92**, 1717-1730, (2000).
6. Gobeil, S., Zhu, X., Doillon, C. J. & Green, M. R. A genome-wide shRNA screen identifies GAS1 as a novel melanoma metastasis suppressor gene. *Genes Dev* **22**, 2932-2940, (2008).
7. Shoushtari, A. N., Szmulewitz, R. Z. & Rinker-Schaeffer, C. W. Metastasis-suppressor genes in clinical practice: lost in translation? *Nat Rev Clin Oncol* **8**, 333-342, (2011).
8. Steeg, P. S. Metastasis suppressors alter the signal transduction of cancer cells. *Nat Rev Cancer* **3**, 55-63, (2003).
9. Rodriguez, L. G., Wu, X. & Guan, J. L. Wound-healing assay. *Methods Mol Biol* **294**, 23-29, (2005).
10. Chen, H. C. Boyden chamber assay. *Methods Mol Biol* **294**, 15-22, (2005).
11. Xie, Y. *et al.* A microchip-based model wound with multiple types of cells. *Lab Chip* **11**, 2819-2822, (2011).
12. Irimia, D., Charras, G., Agrawal, N., Mitchison, T. & Toner, M. Polar stimulation and constrained cell migration in microfluidic channels. *Lab Chip* **7**, 1783-1790, (2007).
13. Shin, M. K., Kim, S. K. & Jung, H. Integration of intra- and extravasation in one cell-based microfluidic chip for the study of cancer metastasis. *Lab Chip* **11**, 3880-3887, (2011).
14. Yan, J. & Irimia, D. Stochastic variations of migration speed between cells in clonal populations. *Technology (Singap World Sci)* **2**, 185-188, (2014).
15. Desai, S. P., Bhatia, S. N., Toner, M. & Irimia, D. Mitochondrial localization and the persistent migration of epithelial cancer cells. *Biophys J* **104**, 2077-2088, (2013).
16. Bajpai, S., Mitchell, M. J., King, M. R. & Reinhart-King, C. A. A microfluidic device to select for cells based on chemotactic phenotype. *Technology (Singap World Sci)* **2**, 101-105, (2014).
17. Irimia, D. & Toner, M. Spontaneous migration of cancer cells under conditions of mechanical confinement. *Integr Biol (Camb)* **1**, 506-512, (2009).
18. Mak, M., Reinhart-King, C. A. & Erickson, D. Microfabricated physical spatial gradients for investigating cell migration and invasion dynamics. *PLoS One* **6**, e20825, (2011).

19. Gallego-Perez, D. *et al.* Microfabricated mimics of in vivo structural cues for the study of guided tumor cell migration. *Lab Chip* **12**, 4424-4432, (2012).
20. Ko, Y. G., Co, C. C. & Ho, C. C. Gradient-free directional cell migration in continuous microchannels. *Soft Matter* **9**, 2467-2474, (2013).
21. Chung, S. *et al.* Cell migration into scaffolds under co-culture conditions in a microfluidic platform. *Lab Chip* **9**, 269-275, (2009).
22. De Cock, L. J. *et al.* Engineered 3D microporous gelatin scaffolds to study cell migration. *Chem Commun (Camb)* **48**, 3512-3514, (2012).
23. Chaw, K. C., Manimaran, M., Tay, E. H. & Swaminathan, S. Multi-step microfluidic device for studying cancer metastasis. *Lab Chip* **7**, 1041-1047, (2007).
24. Kaji, H., Yokoi, T., Kawashima, T. & Nishizawa, M. Controlled cocultures of HeLa cells and human umbilical vein endothelial cells on detachable substrates. *Lab Chip* **9**, 427-432, (2009).
25. Jeon, J. S., Zervantonakis, I. K., Chung, S., Kamm, R. D. & Charest, J. L. In vitro model of tumor cell extravasation. *PLoS One* **8**, e56910, (2013).
26. Culligan, K. *et al.* A detailed appraisal of mesocolic lymphangiology - an immunohistochemical and stereological analysis. *J Anat* **225**, 463-472, (2014).
27. Zhong, S. Q., Xu, Y. D., Zhang, Y. F., Hai, L. S. & Tang, F. C. Three-dimensional structure of lymphatics in rabbit stomach. *World J Gastroenterol* **4**, 550-552, (1998).
28. Nakayama, A., Ogawa, A., Fukuta, Y. & Kudo, K. Relation between lymphatic vessel diameter and clinicopathologic parameters in squamous cell carcinomas of the oral region. *Cancer* **86**, 200-206, (1999).
29. Altschuler, S. J. & Wu, L. F. Cellular heterogeneity: do differences make a difference? *Cell* **141**, 559-563, (2010).
30. Magee, J. A., Piskounova, E. & Morrison, S. J. Cancer stem cells: impact, heterogeneity, and uncertainty. *Cancer Cell* **21**, 283-296, (2012).
31. Negrini, S., Gorgoulis, V. G. & Halazonetis, T. D. Genomic instability--an evolving hallmark of cancer. *Nat Rev Mol Cell Biol* **11**, 220-228, (2010).
32. Hong, S., Pan, Q. & Lee, L. P. Single-cell level co-culture platform for intercellular communication. *Integr Biol (Camb)* **4**, 374-380, (2012).
33. Zheng, C. *et al.* Live cell imaging analysis of the epigenetic regulation of the human endothelial cell migration at single-cell resolution. *Lab Chip* **12**, 3063-3072, (2012).
34. Kraning-Rush, C. M., Carey, S. P., Lampi, M. C. & Reinhart-King, C. A. Microfabricated collagen tracks facilitate single cell metastatic invasion in 3D. *Integr Biol (Camb)* **5**, 606-616, (2013).
35. Mak, M. & Erickson, D. Mechanical decision trees for investigating and modulating single-cell cancer invasion dynamics. *Lab Chip* **14**, 964-971, (2014).
36. Pushkarsky, I. *et al.* Automated single-cell motility analysis on a chip using lensfree microscopy. *Sci Rep* **4**, 4717, (2014).
37. Stroka, K. M. *et al.* Water permeation drives tumor cell migration in confined microenvironments. *Cell* **157**, 611-623, (2014).

38. Rosenthal, D. T. *et al.* p38gamma promotes breast cancer cell motility and metastasis through regulation of RhoC GTPase, cytoskeletal architecture, and a novel leading edge behavior. *Cancer Res* **71**, 6338-6349, (2011).
39. Frimat, J. P. *et al.* A microfluidic array with cellular valving for single cell co-culture. *Lab Chip* **11**, 231-237, (2011).
40. Tan, W. H. & Takeuchi, S. A trap-and-release integrated microfluidic system for dynamic microarray applications. *Proc Natl Acad Sci U S A* **104**, 1146-1151, (2007).
41. Chen, Y. C. *et al.* Paired single cell co-culture microenvironments isolated by two-phase flow with continuous nutrient renewal. *Lab Chip* **14**, 2941-2947, (2014).
42. Joyce, J. A. & Pollard, J. W. Microenvironmental regulation of metastasis. *Nat Rev Cancer* **9**, 239-252, (2009).
43. Kakinuma, T. & Hwang, S. T. Chemokines, chemokine receptors, and cancer metastasis. *J Leukoc Biol* **79**, 639-651, (2006).
44. Koizumi, K., Hojo, S., Akashi, T., Yasumoto, K. & Saiki, I. Chemokine receptors in cancer metastasis and cancer cell-derived chemokines in host immune response. *Cancer Sci* **98**, 1652-1658, (2007).
45. Walker, G. M. *et al.* Effects of flow and diffusion on chemotaxis studies in a microfabricated gradient generator. *Lab Chip* **5**, 611-618, (2005).
46. Scarpino, S. *et al.* Hepatocyte growth factor (HGF) stimulates tumour invasiveness in papillary carcinoma of the thyroid. *J Pathol* **189**, 570-575, (1999).
47. Wei, W., Kong, B., Yang, Q. & Qu, X. Hepatocyte growth factor enhances ovarian cancer cell invasion through downregulation of thrombospondin-1. *Cancer Biol Ther* **9**, 79-87, (2010).
48. Yang, J. & Weinberg, R. A. Epithelial-mesenchymal transition: at the crossroads of development and tumor metastasis. *Dev Cell* **14**, 818-829, (2008).
49. Kalluri, R. & Weinberg, R. A. The basics of epithelial-mesenchymal transition. *J Clin Invest* **119**, 1420-1428, (2009).
50. Nieto, M. A. The ins and outs of the epithelial to mesenchymal transition in health and disease. *Annu Rev Cell Dev Biol* **27**, 347-376, (2011).
51. Rosenthal, D. T. *et al.* RhoC impacts the metastatic potential and abundance of breast cancer stem cells. *PLoS One* **7**, e40979, (2012).
52. Kleer, C. G. *et al.* RhoC-GTPase is a novel tissue biomarker associated with biologically aggressive carcinomas of the breast. *Breast Cancer Res Treat* **93**, 101-110, (2005).
53. Qi, X. *et al.* p38gamma mitogen-activated protein kinase integrates signaling crosstalk between Ras and estrogen receptor to increase breast cancer invasion. *Cancer Res* **66**, 7540-7547, (2006).
54. Lehman, H. L. *et al.* Regulation of inflammatory breast cancer cell invasion through Akt1/PKBalpha phosphorylation of RhoC GTPase. *Mol Cancer Res* **10**, 1306-1318, (2012).
55. Pfaffl, M. W., Horgan, G. W. & Dempfle, L. Relative expression software tool (REST) for group-wise comparison and statistical analysis of relative expression results in real-time PCR. *Nucleic Acids Res* **30**, e36, (2002).

Chapter 3

Macrophages Enhance Migration in Inflammatory Breast Cancer Cells via RhoC GTPase Signaling

Chapter Summary

In addition to discerning genetic molecular drivers of metastasis as in Chapter 2, it is equally important to characterize environmental cues that may stimulate potential metastatic cells and trigger them to bypass a metastatic sieve. A tumor does not grow in isolation; it is surrounded by non-cancerous stroma and also an infiltration of immune cells. Some of these immune cells are macrophages, termed tumor-associated macrophages, and have been shown to have a pro-tumorigenic and pro-metastatic effect. In this work, we study the effect of macrophage-conditioned media on inflammatory breast cancer. This is a rare and very aggressive subset of breast cancer nearly metastatic from its inception. We demonstrate that inflammatory breast cancer cells are hyper-responsive to macrophage-conditioned media, which stimulates an extreme migratory phenotype. We found that interleukins -6, -8, and -10 within the macrophage media are sufficient to induce this effect individually and that a Ras-homology GTPase is necessary for the extreme migration.

Introduction

Inflammatory breast cancer (IBC) is a rare and very aggressive form of breast cancer with the poorest prognosis[1-4]. IBC is characterized by a rapid onset – within 6 months by definition – of symptoms comprising breast erythema, edema which may cause a peau d'orange appearance of the overlying skin, and occasional ulceration[1-3]. A definitive diagnosis of IBC is made with these clinical symptoms and timeline coupled with pathologic confirmation of invasive carcinoma[3]. Although IBC has a low incidence (about 2% in the United States[1,2,4]), it is the most lethal form of breast cancer with a median survival of 3 years compared to >10 years for other non-inflammatory breast cancers[4-6]. A key characteristic of inflammatory breast cancer distinguishing it from non-inflammatory breast cancers (nIBC) is IBC's propensity for near immediate metastasis. About two-thirds of IBC patients present with lymph node involvement and one-third of patients already have distant metastasis at initial diagnosis[1,2,5,6]. The survival curves for metastatic nIBC and non-metastatic IBC are nearly identical the first five years post diagnosis, further highlighting IBC's characteristic lethality and rapid metastasis[7].

Many genetic profiling studies have been conducted to try and discern the specific differences between IBC and nIBC that drive the dramatic disparity in mortality[8-12]. However, the overarching conclusion of these studies is that no tumor molecular signature can be considered conclusive to adequately distinguish IBC and nIBC[2,8]. The 5 molecular subtypes of nIBC (luminal A,

luminal B, basal-like, HER2-enriched, and normal-like) are also represented in IBC and IBC patients have a poor prognosis regardless of the subtype[5,6,10,13,14]. A recent study determined that initial findings in differential gene expression between IBC and nIBC was in fact due to a difference in proportion of the 5 subtypes (IBC has fewer Luminal A and greater HER2-enriched cancers); when they directly compared subtypes, all IBC vs. nIBC expression differences disappeared[10]. Yet another study looked at histologic features in nIBC that can predict patient outcomes and found the markers had no such predictive effect in IBC leading the authors to conclude that IBC has a distinct biological behavior[15]. One of the few proteins that is continuously found to be differentially expressed between IBC and nIBC is the Ras homology GTPase isoform, RhoC[16-19]. Rho proteins are involved in the actin cytoskeleton turnover and are important for cell motility[20-22]. Rho GTPases also signal to a variety of downstream effectors to influence cell survival and proliferation[20,21]. While it is not a wholly specific marker for IBC as it is expressed in some late stage nIBCs due to its general importance in cancer cell migration[23,24], RhoC is overexpressed in over 90% of IBC cancers and has been shown to be a driver of IBC metastasis[18,19,25-27].

The focus on tumor-intrinsic features such as gene expression and the recent finding of a stromal gene signature associated with IBC have yielded helpful, but limited, explanatory power for the particularly aggressive nature of IBC[28]. Thus, we hypothesized that perhaps a tumor-*extrinsic* factor might further explain the differences in behavior of IBC and nIBC. Knowing the importance of the immune

components in the tumor microenvironment, we sought to determine if tumor-associated macrophages (TAMs) could promote IBC's extreme metastatic nature. TAMs have been shown to have a wide range of pro-tumor effects in many cancers including supporting angiogenesis, promotion of tumor cell invasion and migration, suppressing antitumor responses, and even promoting metastasis[29-32].

In this work, we show that the IBC cell lines SUM149 and SUM190 are hyper-responsive to macrophage-conditioned media as compared to the normal-like MCF10A breast cell line and the aggressive nIBC MDA-MB-231 breast cancer cell line. We further interrogate the enhanced IBC migratory phenotype to macrophage-conditioned media using a microfluidic migration device that allows for individual cell positional information yielding insights into the specific migration pattern. We determined that interleukins -6, -8, and -10 within the macrophage-conditioned media are sufficient to stimulate this enhanced IBC migration. Furthermore, we found that the known metastatic oncogene, RhoC GTPase, is necessary for the enhanced migration response and for the macrophage-conditioned media activation of the mitogen-activated protein kinase (MAPK) cascade.

Results

Macrophage-conditioned media enhances IBC migration

The normal-like MCF10A, aggressive non-inflammatory breast cancer MDA-MB-231, and inflammatory breast cancer SUM190 and SUM149 cell lines were evaluated for their migration potential to serum and macrophage-conditioned media (MCM) in transwell migration chambers. MCM was generated from phorbol 12-myristate 13-acetate (PMA) differentiated U937 cells as described in the methods section. MCF10A and MDA-MB-231 cells did not migrate more than the negative control (serum free media in the top and bottom chambers, SFM – SFM) when exposed to MCM in the bottom chamber (SFM – MCM) or both chambers (MCM – MCM) (columns 1, 2 and 3) (Fig. 3.1 A,B). The two cell lines had similar migration toward a serum gradient in the presence or absence of MCM (columns 4 and 5) (Fig. 3.1 A, B). In contrast, the IBC cell line, SUM190, was more motile merely in the presence of MCM without a concentration gradient (column 2) and MCM induced an eight-fold greater increase in migration over the 10% serum gradient positive control (column 5) (Fig. 3.1 C). SUM149 cells also were more responsive to the MCM than were MCF10A or MDA-MB-231 cells. SUM149 cells had significantly enhanced migration toward an MCM gradient and were more motile in the presence of MCM stimulation over SFM negative control (columns 2 and 3) (Fig. 3.1 D). Representative transwell migration membranes for each cell line and condition are shown in Figure 3.S1.

Given that the IBC cell lines were more responsive to the MCM than the non-IBC cell lines, we next sought to understand if a certain subpopulation of the IBC cells was responsible for this behavior. In order to facilitate the tracking of individual

cell migration paths, we utilized a microfluidic migration device with a series of horizontal migration channels that allowed us to determine single cell positional information throughout the migration experiment (Fig. 3.S2). In these devices, a passive diffusion concentration gradient can be generated from the left side of the device to the right side by loading the experimental media into the left and right reservoirs, respectively (Fig. 3.S2 B), much like the top and bottom chambers of a transwell assay. Cells are loaded down the left side of the device and then attracted to migrate toward the right side where there is a higher concentration of soluble factors. Using the microfluidic devices, we discovered that the increase in migration was not due to undirected increased chemomotility as might have been suggested by the transwell assays (MCM – MCM not different from SFM – SFM), but in fact due to a statistically significant enhanced capability of both SUM190 and SUM149 IBC cells to chemotax about twice the distance toward the serum gradient in the presence of MCM stimulation (MCM – MCM+10% serum greater than SFM – 10% serum) (Fig. 3.2 A, B). This distinction was likely only possible through having migration distance information on a per-cell basis rather than the binary output of a transwell assay. SUM190 and SUM149 cells also respectively migrated 1.3 and 1.5 times further toward an MCM gradient than toward the 10% serum gradient controls demonstrating that the MCM could also act as a chemoattractant (Fig. 3.2 A, B). A closer inspection of the distribution of cell migration distances reveals that this effect stems from two subpopulations of the IBC cell lines (Fig. 3.2 C, D). In the SFM – MCM conditions, a bimodal distribution of approximately equal percentages of cells is

apparent comprising of non-migratory cells (defined as those cells migrating less than the SFM – SFM average distance) and extreme migratory cells (defined as those cells migrating further than the SFM – 10% serum average distance) (Fig. 3.2 C, D). These two groups account for the vast majority, about 80 – 90%, of all the IBC cells. The significantly enhanced chemotaxis in the MCM – MCM+10% serum groups is subsequently explained then by the presence of the MCM on the left side of the device stimulating all the cells at the starting location which prompts the conversion of the non-migratory cell population into extreme migratory cells. In SUM149 cells, the non-migratory cell percentage dropped from 40% of the population to 10% and the extreme migrators increased proportionately from 50% to 80% when comparing the SFM – MCM and MCM – MCM+10% serum conditions (Fig. 3.2 D). While not as pronounced, a similar trend of a decreasing percentage of non-migratory and a proportionate increasing percentage of extreme migratory cells was seen in the SUM190 cells as well (Fig. 3.2 C). This led us to conclude that it was not necessarily a specific factor in the conditioned media acting as the chemoattractant leading to enhance migration in the MCM – MCM+10% serum groups, but that the cytokine milieu might serve to “prime” the IBC cells’ cellular machinery in order to become hyper-responsive to the serum chemoattractant.

Interleukins -6, -8, and -10 are sufficient to enhance IBC migration

In order to determine what molecular components of the macrophage-conditioned media were effecting the enhanced migration of the IBC cells, we

profiled the MCM and media conditioned by SUM190 and SUM149 cells using a bead-based 27-plex ELISA. The concentrations of selected cytokines are plotted in Figure 3.3 A and B with all 27 cytokines shown in Figure 3.S3 A. The first column represents the PMA-differentiated U937 MCM. The second and fourth columns show the basal secretion of cytokines by unstimulated SUM190 and SUM149 cells, respectively. The third and fifth columns represent SUM190 and SUM149 cells stimulated with MCM. In accordance with prior findings[33], we found that SUM149 cells basally secrete high amounts (77 ng/mL) of interleukin (IL) -8. Interestingly, in the presence of MCM, SUM190 and SUM149 cells were both stimulated to produce chemokine C-C motif ligand 5 (CCL5), IL-6, vascular endothelial cell growth factor (VEGF), and chemokine C-C motif ligand 2 (CCL2) (Fig. 3.3 A, B). The concentrations of these cytokines increased over the levels found in the MCM and the only cellular production source were the IBC cells themselves for these conditions.

Cytokines IL-8, tumor necrosis factor α (TNFα), CCL5, IL-6, VEGF, CCL2, and IL-10 were selected based on their high concentrations and suspected involvement in non-inflammatory breast cancer for transwell migration screening of enhanced migration[34]. For each cytokine, a no gradient control (equal concentrations of the cytokine in the top and bottom chambers: cytokine – cytokine) and a serum-spiked condition (cytokine – cytokine+10% serum) mimicking the MCM – MCM+10% serum condition were performed. Cytokines were used at similar concentrations as those measured in the MCM. In SUM190

cells, although all the tested cytokines trended toward increasing migration, only IL-6, IL-8, and IL-10 induced statistically significantly enhanced migration over the SFM – 10% serum control (Fig. 3.3 C). As SUM190 transwell migration was a good predictor of the microfluidic migration behavior (Fig. 3.1 and 3.2), these three cytokines were further profiled in the microfluidic devices. IL-6 and IL-10 stimulation of SUM149 cells also increased their migration over SFM – 10% serum control, although the effect was not statistically significant (Fig. 3.S3 B).

All three cytokines tested – IL-6, IL-8, and IL-10 – significantly enhanced migration over 10% serum gradient controls across both IBC cell lines in the microfluidic migration devices (Fig. 3.3 D, E). While the fold increase in migration was moderate at about 1.5 times that of the 10% serum condition for each cytokine, it was robust enough that in SUM149 cells the IL6 – IL6+10% serum condition there was no statistically significant difference from the MCM – MCM+10% serum condition and in SUM190 cells none of the cytokine – cytokine+10% serum conditions were statistically different from the MCM – MCM+10% serum condition (Fig. 3.3 D, E).

RhoC GTPase is necessary for the IBC extreme migration and MCM activation of the MAPK cascade

Given that RhoC GTPase has been shown to be a key driver of IBC metastasis in *in vivo* models[26] and it is differentially expressed between IBC and nIBC tumors across studies[16,17,19], we hypothesized that RhoC might play a role in the

enhanced migration response of IBC to the MCM. In support of this, both IBC cell lines, SUM190 and SUM149, had an increase in RhoC expression after stimulation with MCM while there was no change in RhoC expression in either MCF10A or MDA-MB-231 cell lines (Fig. 3.4 A). To further test the function of RhoC, we generated a CRISPR construct targeting RhoC to knockout the gene in both SUM149 (149crRhoC) and SUM190 (190crRhoC) cell lines (Fig. 3.4 B). The knockout was specific to RhoC and did not have an effect on the expression of the closely related RhoA GTPase (Fig. 3.4 B). As seen in Figures 3.4 C and D, knocking out RhoC specifically and completely abolished the extreme migration of the MCM – MCM+10% serum condition in both 149crRhoC and 190crRhoC cells in the microfluidic migration assay. Verifying that the CRISPR RhoC effect was specific to the MCM enhanced migration and did not simply abrogate all migration, the 149crRhoC and 190crRhoC cells were still able to migrate to the 10% serum gradient as robustly as wildtype SUM149 and SUM190 (Fig. 3.S4).

The mitogen-activated protein kinase (MAPK) pathway has previously been shown to be important in RhoC signaling and therefore we investigated its role in MCM induced IBC cell migration[18]. MCM stimulation of wildtype SUM190 and SUM149 induces phosphorylation and activation of MEK, MAPK, and p38 (Fig. 3.5). In 149crRhoC cells, stimulation with MCM fails to phosphorylate any of these proteins in the absence of RhoC (Fig. 3.5). In 190crRhoC cells, MEK and MAPK are still activated in the absence of RhoC while p38 phosphorylation is

abrogated (Fig. 3.5). STAT3 phosphorylation also increases in both SUM190 and SUM149 cells with stimulation by MCM and its phosphorylation abrogated in the absence of RhoC.

Discussion

Many studies have sought to understand the genetic determinants of the IBC phenotype[8-10,15]. The research has demonstrated, however, IBC's genetic heterogeneity and molecular subtype similarity to nIBC and has failed to discover an IBC-specific genetic profile[2,10]. This led us to conjecture that factors extrinsic to the cancer cells themselves might explain IBC's pronounced metastatic propensity and tested whether tumor-associated macrophages could be contributing to the disease. A similar view, in accordance with our hypothesis, that breast parenchymal biology – altered by breastfeeding, pregnancy, and body-mass index – might provide the proper "soil" for IBC to flourish was also recently posited[7].

In this study, we found that two IBC cell lines, SUM190 and SUM149, were hyper-responsive to macrophage-conditioned media as compared to the normal-like MCF10A and nIBC MDA-MB-231 cell lines. To analyze this behavior further, we designed a microfluidic migration device that allowed us to follow individual cells and glean the precise magnitude of their response, something not possible with a traditional transwell assay. We demonstrated that stimulating the IBC cells with MCM enhances their migration to a serum gradient double that of the MCM-

unstimulated cells. The MCM itself is not the cue for the increased migration *per se* as in the extreme migratory condition there is no gradient to factors in the MCM, and the MCM – MCM condition alone did not increase migration over the SFM – SFM negative control. Therefore, we purport that components of the macrophage-conditioned media serve to “prime” the IBC cells in order to become hyper-responsive and extremely migratory when they do receive the directional chemoattractant signal from the serum gradient. Our microfluidic migration devices also allowed us to discern that within SUM190 and SUM149, there exists a population of cells that are intrinsic extreme migrators to an MCM gradient. Upon stimulation with MCM on both sides of the device, thus removing this gradient, and superimposing a serum gradient (MCM – MCM+10% serum), many of the previous would-be non-migratory cells were converted to extreme migratory cells.

When we profiled the secreted factors in the macrophage-conditioned media and screened them for increasing the IBC migration potential, we found that interleukins -6, -8, and -10 alone were sufficient to recapitulate the enhanced migration effect. When exposed to a non-gradient condition for these cytokines superimposed with a serum gradient (cytokine – cytokine+10% serum), both SUM190 and SUM149 had significantly increased migration over the serum gradient control alone (SFM – 10% serum). While significant, this increase in migration was more modest compared to the doubling of migration seen with the total MCM. Likely this is due a mixture of cytokines found in the MCM acting in

concert to induce the extreme migration effect. However, the combinatorics of 27+ factors found in the MCM precluded experimentation. Our finding that these three cytokines – IL-6, IL-8, and IL-10 – might contribute to IBC's metastatic phenotype is in agreement with another study that showed in a canine model of IBC tissue homogenate levels of IL-6, IL-8, and IL-10 were significantly higher than in canine nIBC[35]. Furthermore, in nIBC, patient serum levels of IL-6, IL-8, and IL-10 all increase with increasing stage supporting their association with invasion and metastasis[34,36].

Our results are also in keeping with other recent studies that profiled the effect of macrophages on inflammatory breast cancer[37-39]. One group studied the epithelial-mesenchymal transition in IBC cell lines and found IL-6 to be one essential driver of the transition as measured by qRT-PCR of a standard gene panel[37]. A second group in a series of experiments investigated the effect of conditioned media from undifferentiated U937 cells on SUM149 and later isolated CD14+ leukocytes directly from the draining blood vessels supplying IBC and nIBC tumors during surgery[38,39]. This patient-based study showed that not only do IBC patients have greater staining in tumor sections for CD14+ monocytes, but that IL-8 and IL-10 were among the cytokines significantly differently expressed between IBC and nIBC macrophages[38].

We now add to this nascent body of work investigating the role of the microenvironment on IBC our own results utilizing two IBC cell lines and yield

insights into how the macrophage-secreted cytokines may be functioning. Rather than acting as bona fide chemoattractants themselves, we propose that the macrophage-conditioned media – and in it IL-6, IL-8, and IL-10 – "prime" the IBC cells to have a magnified migration response by increasing the expression of RhoC. Furthermore, we demonstrated a necessity for RhoC GTPase for the MCM-induced enhanced migration in both SUM190 and SUM149 and suggest it likely mediates the effect by signaling through the MAPK cascade. Using CRISPR RhoC knockouts of the IBC cell lines, the increased migration in the MCM – MCM+10% serum condition is completely abrogated and the CRISPR cell lines migrate no further than they do to SFM – 10% serum. MCM also increases phosphorylation of components of the MAPK pathway and STAT3 in both SUM190 and SUM149 cells. This pathway activation is completely abrogated in SUM149 cells in the absence of RhoC. In 190crRhoC cells, MAPK and MEK remained activated when treated with MCM, but p38 and STAT3 signaling are abolished. SUM190 cells have HER-2 overexpression and therefore may require minimal signal to initiate signal transduction in this pathway accounting for the differential signaling between SUM190 and SUM149 cells[40]. IBC is a heterogeneous disease as demonstrated by the difference in signaling between SUM190 and SUM149 cells. Yet while the precise patterns of phosphorylation and activation might differ between the two cell lines, the two IBC cell lines share the commonality of enhanced migration to macrophage-secreted cytokines through the common node of RhoC. Thus, our work reveals both a role for the microenvironment in tumor-associated macrophage secreted

cytokines and suggests RhoC as a potential target for therapeutic intervention aimed at preventing the metastasis of inflammatory breast cancer.

Materials and Methods

Cell culture

SUM149 and SUM190 cells were maintained in Ham's F-12 w/L-glutamine (Fisher Scientific) containing 0.5 µg mL-1 Fungizone, 5 µg mL-1 Gentamicin, 100 units mL-1 penicillin, and 100 µg mL-1 streptomycin (all Invitrogen). Additionally, SUM149 cells were supplemented with 5% fetal bovine serum, 5 µg mL-1 Insulin and 1 µg mL-1 Hydrocortisone (Sigma-Aldrich). SUM190 cells were supplemented with 0.1% bovine serum albumin, 5 µg mL-1 Insulin and 1 µg mL-1 Hydrocortisone (Sigma-Aldrich). MDA-MB-231 cells were cultured in RPMI with 10% FBS and 1% penicillin/streptomycin. SUM149 and SUM190 cells were maintained at 37ºC with 10% CO2 and all other cell lines at 37ºC with 5% CO2. Fresh 0.25% trypsin-EDTA in phosphate buffered saline (PBS) was used to re-suspend cells.

CRISPR cell line generation

SUM149 and SUM190 cell lines were transfected using the Nucleofector II system (Lonza) with pSpCas9(BB)-2A-GFP (PX458), which was a gift from Feng Zhang (Addgene plasmid # 48138), containing the target sequence AGGAAGACTATGATCGACTG against RhoC. Two days after transfection, single cells were sorted for GFP expression into 96 well plates. Following clonal

expansion, genomic DNA was isolated and clones were screened for RhoC mutations using SURVEYOR reactions (IDT) with the following primer pair: Forward-CTGTCTTTGCTTCATTCTCCCT and Reverse-CCAGAGCAGTCTTAGAAGCCAT. Positive clones were sequenced to identify specific mutational events and immunoblotted for RhoC and RhoA.

U937 differentiation and macrophage-conditioned media preparation

U937 cells were differentiated to macrophages as reported previously[41,42]. Briefly, 100 ng/mL of phorbol-12-myris-tate-12-acetate (PMA) (Thermo Fisher, BP685) was added to U937 cells in complete growth medium for 24 hours. Then, the differentiated U937 cells were rinsed and serum-free media (SFM) added and collected after another 24 hours. This macrophage-conditioned media was then centrifuged and concentrated using Amicon Ultra 3K filters (EMD Millipore, UFC900324) at 4C and rediluted with fresh SFM.

Transwell migration assay

Corning Costar Transwell supports (Corning, 3422) were used according the manufacturer's protocol. After trypsinization and counting, cells were aliquoted and resuspended in the appropriate media for the top insert and plated at 25,000 cells per insert. After incubation at 37C at either 5% or 10% CO2 for 24 hours, the inserts were removed and the top layer wiped with a cotton swab. Then the cells were fixed and stained with crystal violet. Images were taken at 2X of the

entire migration area and the area of purple color extracted from each image and used as a surrogate for cell number.

Microfluidic device fabrication and assembly

The migration devices were formed from a single layer of PDMS (polydimethlysiloxane), which was fabricated on a silicon substrate by standard soft lithography, and a glass slide. Channel widths were 40 µm and channel height was 10 µm. The PDMS layer was bonded to the glass slide after activation by oxygen plasma treatment (80 Watts, 60 seconds) to form a complete fluidic channel. Before cell loading, collagen I (BD Biosciences, 354236) solution (1.45mL collagen, 0.1mL acetic acid in 50mL deionized water) was flowed through the device for 18-24 hours in a tissue culture incubator to coat collagen on the substrate to enhance cell adhesion. Devices were then rinsed with HBSS for approximately one hour to remove the residual collagen solution before use.

Microfluidic migration assay

After rinsing the collagen coating, 100 µL of cells were loaded into the top left reservoir at 400,000 cells per mL and allowed to flow down the left vertical channel and align at the entrances to the horizontal migration channels. Residual cells were vacuumed and then rinsed away from the top left reservoir and complete culture medium added to all four reservoirs in a “no flow” condition for 6 hours to allow the cells to adhere to the migration device. After, the complete media was removed and serum-free media flowed over the attached

cells for approximately one hour. Then, the top left and right inlet reservoirs were changed to the appropriate media conditions and 0 hour images captured. The device was placed in a tissue culture incubator for 24 hours and the final migration images captured. Cell migration distance was calculated as the difference in horizontal position between the 24 hour and 0 hour images.

Measurement of cytokines in conditioned media

The Bioplex Pro Human Cytokine 27-plex assay (Biorad, M500KCAF0Y) was used to measure cytokine concentrations in the specified media per the manufacturer's protocol. Washing was carried out utilizing a handheld magnetic plate holder and plates were read on a Bioplex MAGPIX (Biorad) machine.

Immunoblotting

Cells were harvested in RIPA buffer (Thermo Scientific) with protease and phosphatase inhibitors (Roche Diagnostics). Immunoblotting was done after sodium dodecyl sulfate (SDS)-polyacrylamide gel electrophoresis (PAGE) on gradient 4-15% gels (Biorad) at 30 µg protein and transfer to polyvinylidene fluoride (PVDF) membranes. All antibodies besides the secondary horseradish peroxidase-conjugated antibody (Santa Cruz Biotechnology) were purchased from Cell Signaling Technologies: phospho-MAPK (Thr202/Tyr204), MAPK, phospho-p38 (Thr180/ Tyr182), p38, phospho- MEK (Ser 217/221), MEK, phospho- STAT3 (Tyr705 and Ser727), STAT3, RhoC, RhoA, ß-actin.

SuperSignal West Pico Luminol/Enchancer Solution was purchased from Thermo Scientific.

Statistical Analysis

Two-tailed, unpaired student's t-tests were used for all comparisons with a significance level of 0.05 considered statistically significant. In Figures, * refers to $P < 0.05$, ** to $P < 0.01$, and *** to $P < 0.001$.

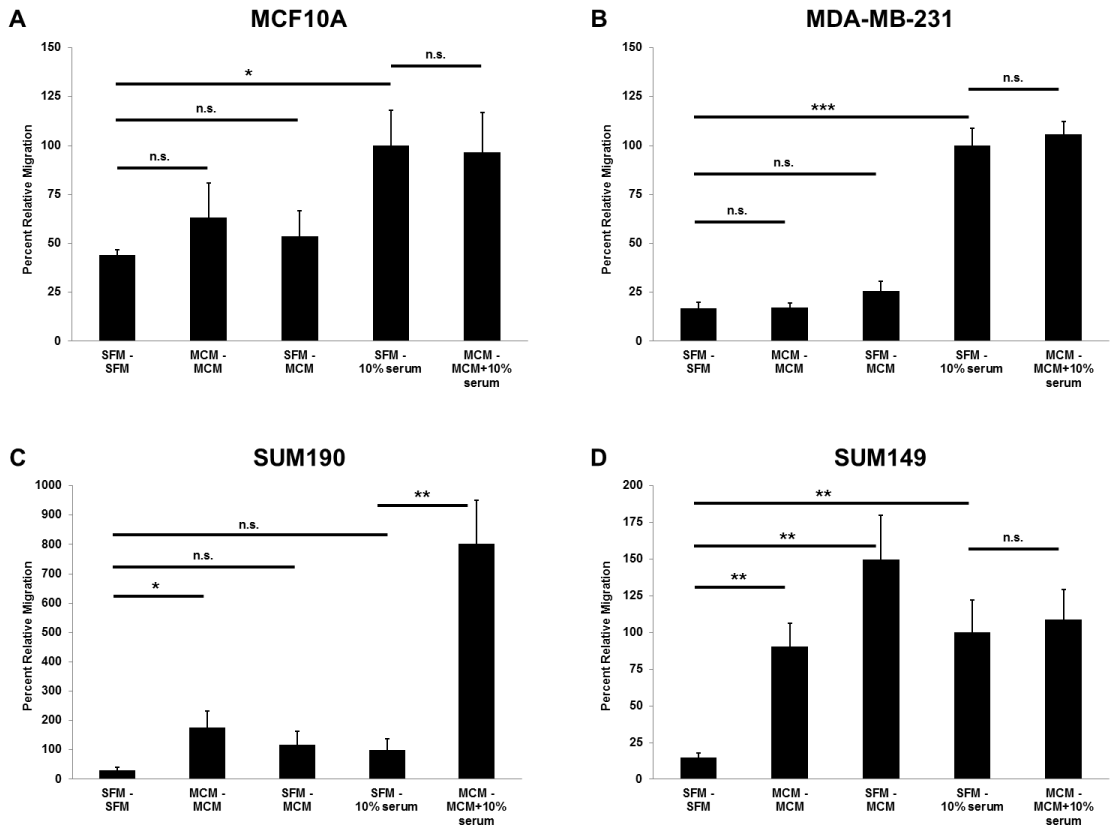

Figure 3.1. Inflammatory breast cancer cells are hyper-responsive to macrophage conditioned media. Transwell migration assays of (A) MCF10A, (B) MDA-MB-231, (C) SUM190, and (D) SUM149 cells. MCF10A and MDA-MB-231 migrated similarly to the SFM – SFM or SFM – 10% serum control conditions when exposed to the MCM. SUM190 migrated 8-fold more when stimulated with MCM in conjunction with a serum gradient. SUM149 was more migratory over the SFM – SFM condition when exposed to MCM – MCM or SFM – MCM. The entire transwell membrane was imaged and the area of migrated cells calculated. All conditions were normalized to the SFM – 10% serum condition as 100% migration. Error bars represent s.e.m.

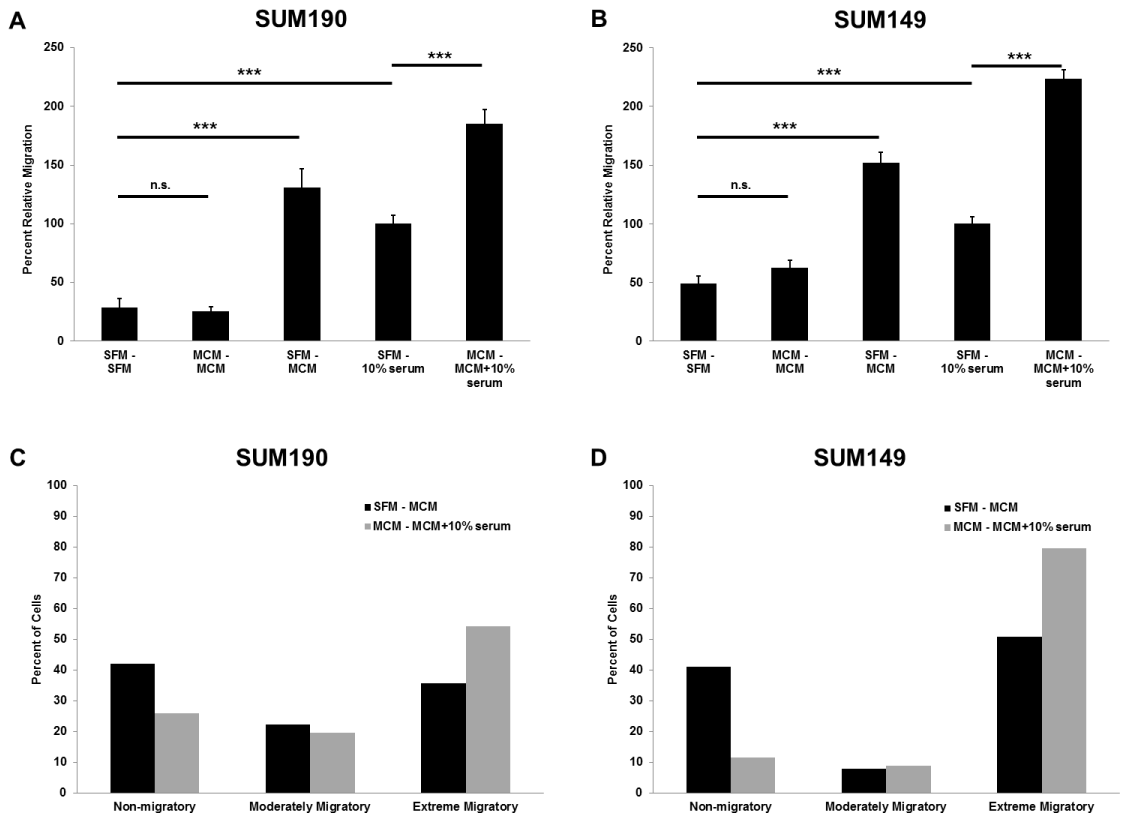

Figure 3.2. Macrophage conditioned media induces extreme migration in inflammatory breast cancer cells. Microfluidic migration device assays of (A) SUM190 and (B) SUM149 cells. Both SUM190 and SUM149 had a 2-fold enhanced migration to the MCM – MCM+10% serum condition over SFM – 10% serum positive control. For (C) and (D), SUM190 and SUM149 cells were separated into 3 groups: non-migratory were cells with a migration distance less than the SFM – SFM average distance, extreme migratory cells were those with a migration distance greater than the SFM – 10% serum average, and moderately migratory cells had distances between these averages. The percentage of total cells for each group is plotted. The MCM – MCM+10% serum condition stimulated non-migratory cells to become extreme migratory cells in SUM190 and SUM149. Error bars represent s.e.m.

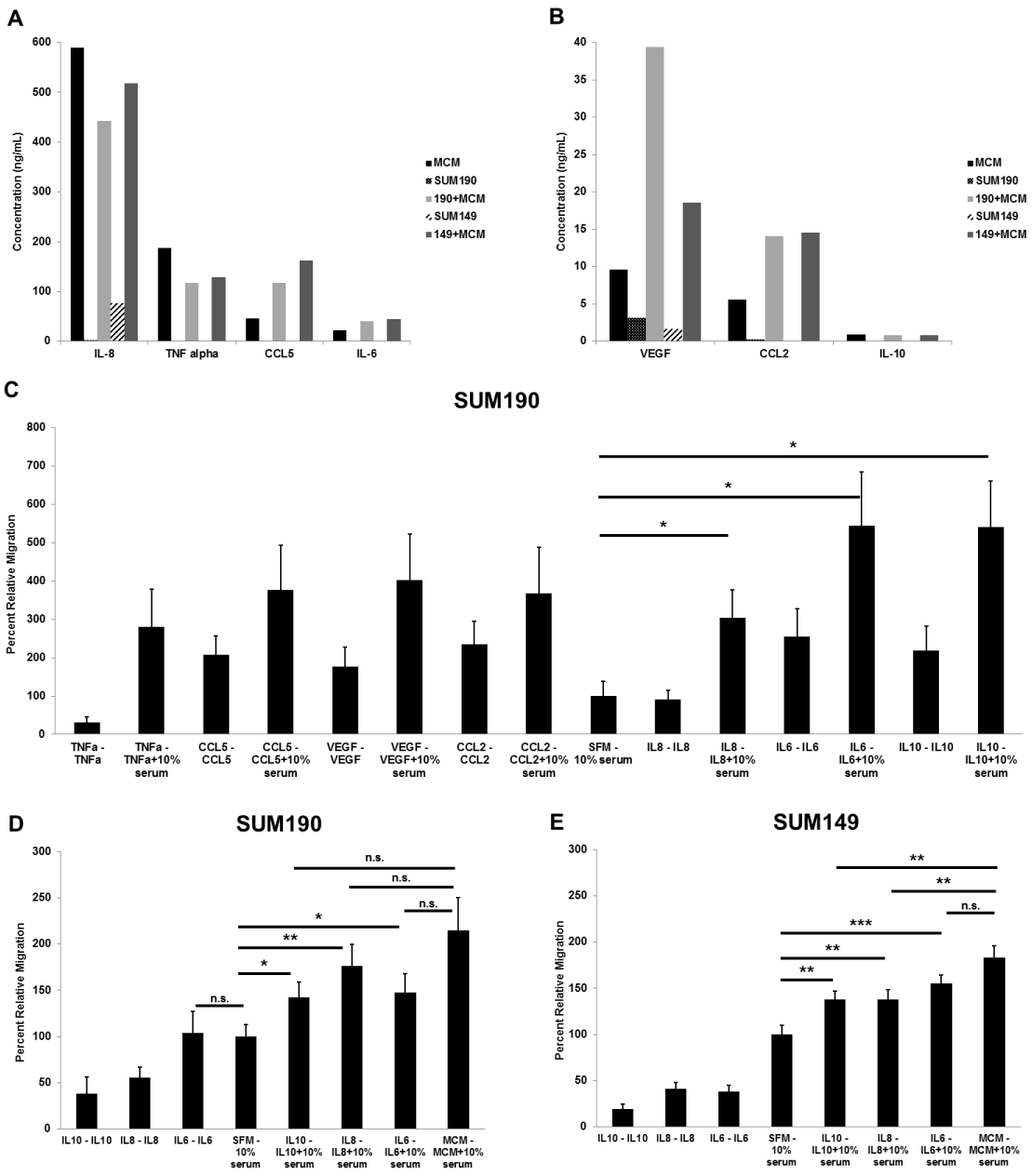

Figure 3.3. IL-6, IL-8, and IL-10 enhance inflammatory breast cancer migration. The concentration of selected cytokines in different media conditions is plotted in (A) and (B). The percent migration relative to the SFM – 10% serum condition for each cytokine stimulation conditions of SUM190 transwell migration is graphed in (C). IL-6, IL-8, and IL-10 significantly increased SUM190 transwell migration. In (D) and (E), microfluidic migration to cytokine conditions is plotted for SUM190 and SUM149 cells, respectively. IL-6, IL-8, and IL-10 significantly enhanced migration in both cell lines over SFM – 10% serum control. Error bars represent s.e.m.

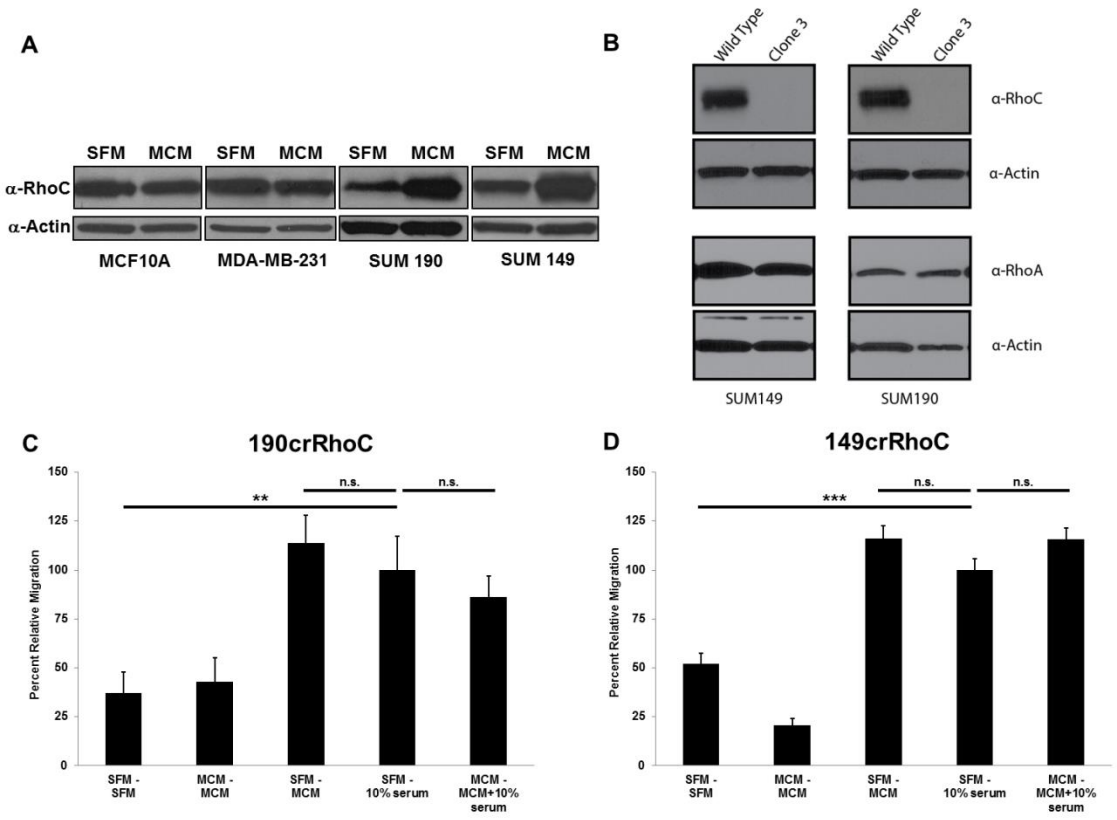

Figure 3.4. RhoC is necessary for the inflammatory breast cancer migration response to macrophage conditioned media. (A) MCM increased the expression of RhoC in SUM190 and SUM149 but not in MCF10A or MDA-MB-231 cells. (B) Immunoblotting confirmation of CRISPR knockout of RhoC and not of RhoA. In (C) and (D), microfluidic migration of the SUM190 and SUM149 CRISPR RhoC knockout cell lines, respectively. RhoC is necessary for the enhanced migration effect as MCM – MCM+10% serum migration is not different from SFM – 10% serum control. Error bars represent s.e.m.

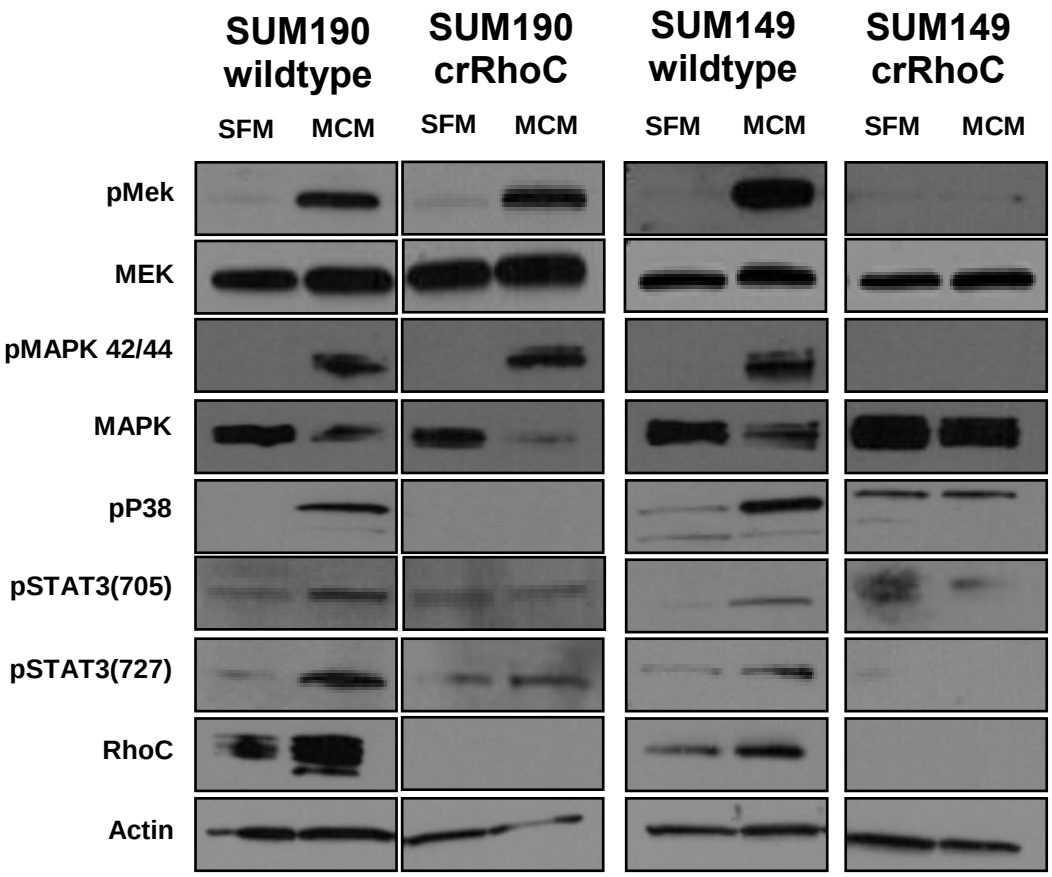

Figure 3.5. Macrophage conditioned media activates the MAPK cascade in inflammatory breast cancer cells. Immunoblotting for the indicated phospho-proteins and total proteins. RhoC was necessary for the MCM-induced phosphorylation of MEK, MAPK, p38, and STAT3 in SUM149 cells and RhoC was necessary for the MCM-induced phosphorylation of p38 and STAT3 in SUM190 cells. Immunoblots shown are representative of 3 separate experiments.

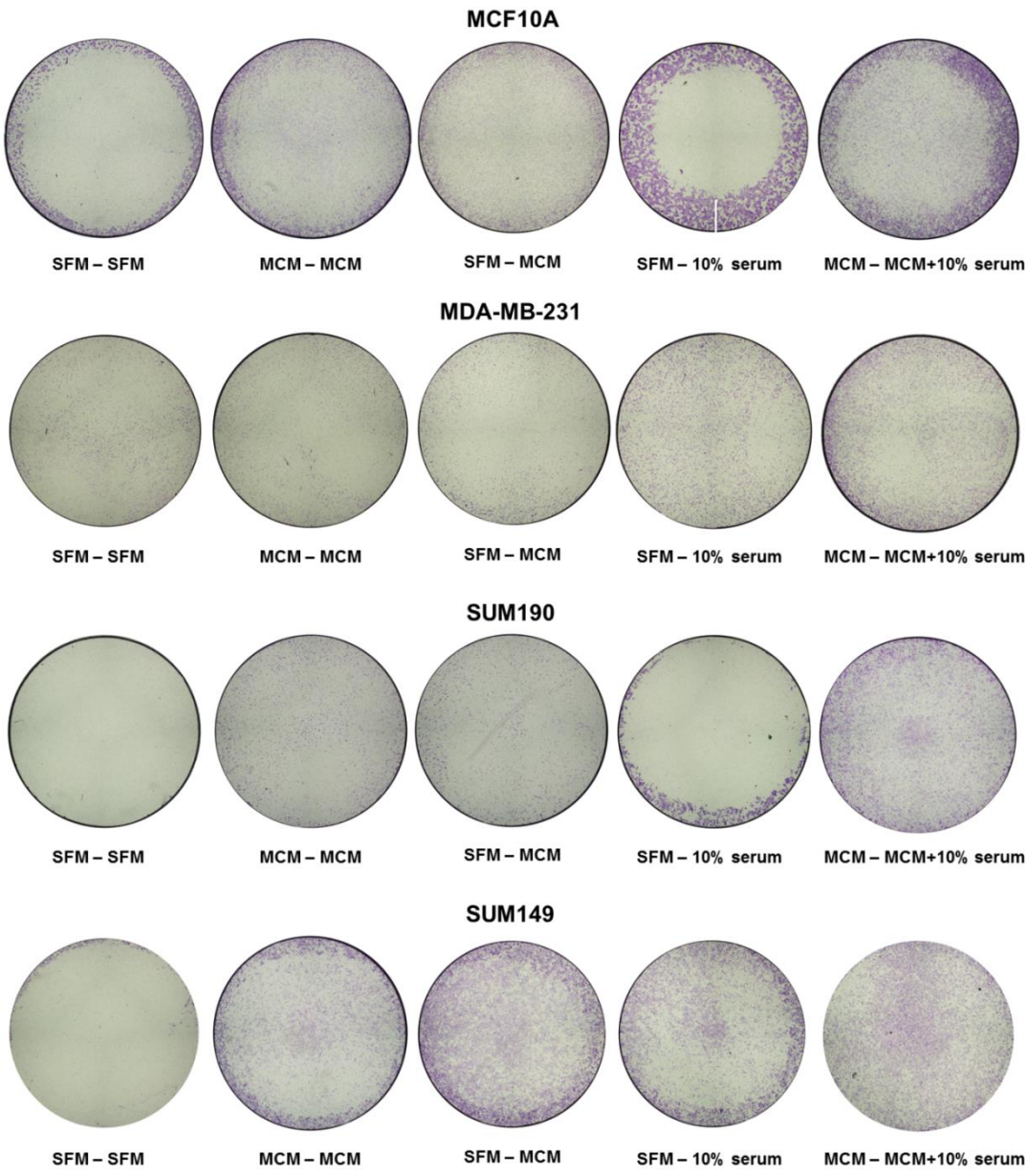

Figure 3.S1. MCF10A, MDA-MB-231, SUM190, and SUM149 transwell migration to macrophage-conditioned media. Representative images of transwell membranes used to calculate percent migration for Figure 1. Cells were stained with crystal violet and the area of purple color extracted from each image and used as a surrogate for cell number. The area of each cell line's SFM – 10% serum condition was used to normalize values.

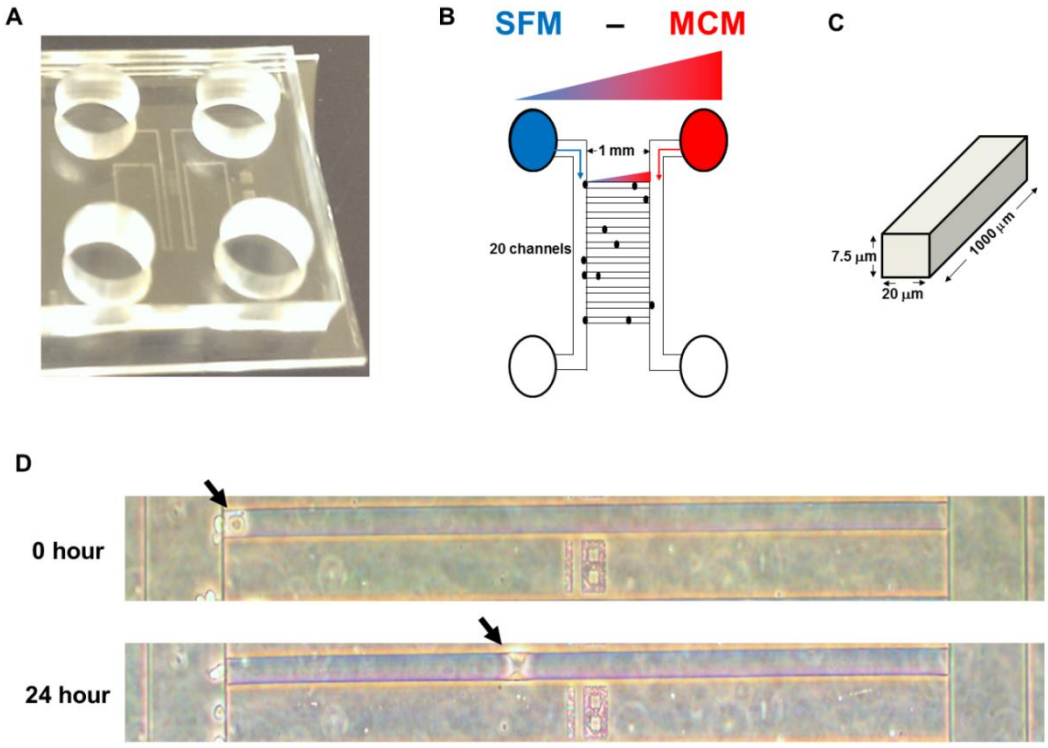

Figure 3.S2. Schematic of the microfluidic migration device. (A) Photograph of the microfluidic migration device depicting the 2 inlet (top) and 2 outlet (bottom) reservoirs. The serpentine loading channels can be seen running vertically with the horizontal migration channels, too small to be appreciated here, running perpendicularly between them. The device is bonded to a standard glass slide. (B) and (C) are schematics of the migration channels and geometry. By loading different media conditions into the left and right inlet reservoirs, a diffusion gradient is created along the axis of the horizontal migration channels. (D) Photomicrographs of one channel and a migrating cell at the 0 hour and 24 hour time points. Migration distance was calculated as the difference between the 24 hour and 0 hour locations.

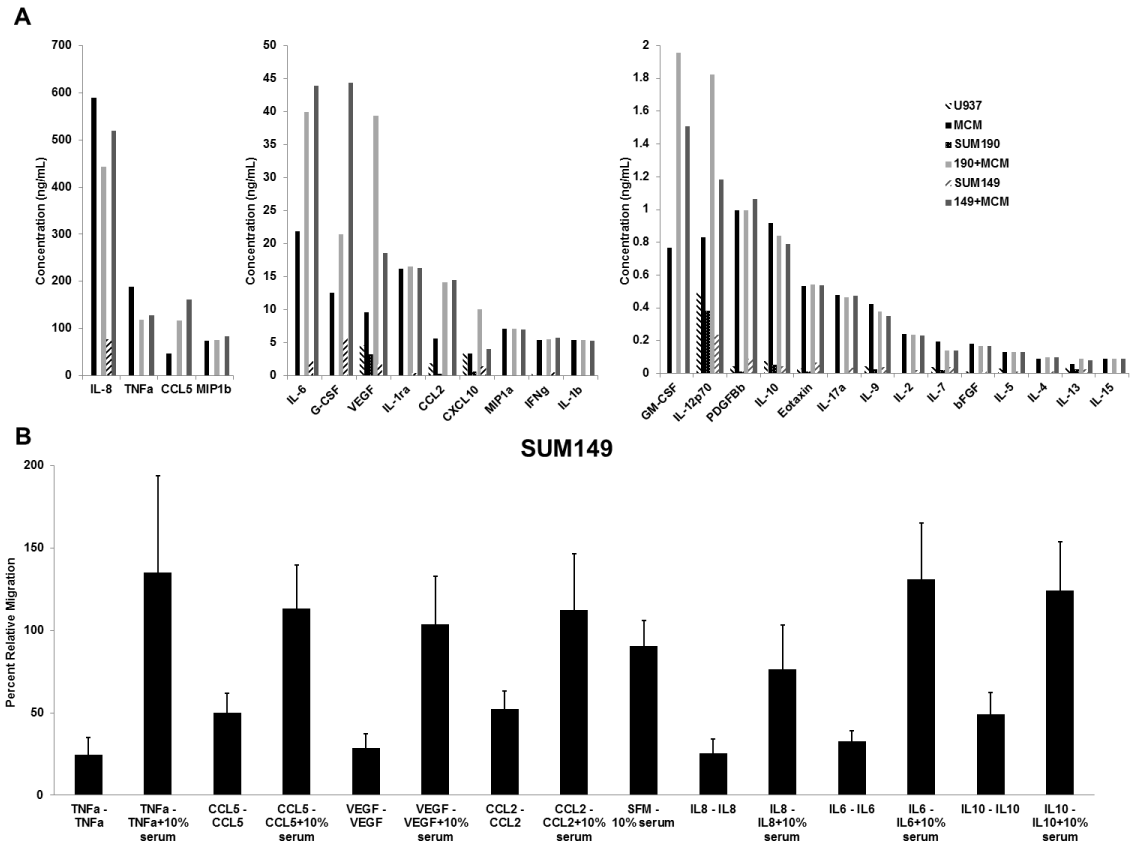

Figure 3.S3. Macrophage-conditioned media cytokines. The concentration of all measured 27 cytokines in different media conditions is plotted in (A). The U937 bar represents undifferentiated U937 monocyte conditioned media. (B) The percent migration relative to the SFM – 10% serum condition for each cytokine stimulation conditions of SUM149 transwell migration.

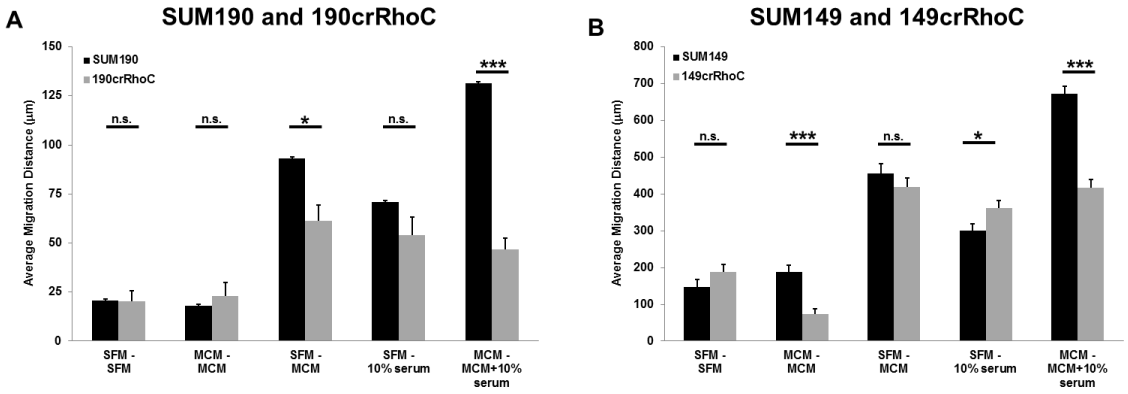

Figure 3.S4. SUM149, 149crRhoC, SUM190, and 190crRhoC average microfluidic migration. Average microfluidic migration distances for (A) SUM190 and 190crRhoC and (B) SUM149 and 149crRhoC cells. SUM190 and 190crRhoC cells did not migrate differently to SFM – 10% serum control, but the absence of RhoC in 190crRhoC cells completely abrogated the enhanced migration response to MCM – MCM+10% serum. 149crRhoC cells migrated further to the SFM – 10% serum condition than SUM149 cells. This would have decreased the likelihood of finding a difference in the extreme migration condition, however the absence of RhoC still completely abrogated the enhanced migration effect in 149crRhoC cells.

References

1. Robertson, F. M. *et al.* Inflammatory breast cancer: the disease, the biology, the treatment. *CA Cancer J Clin* **60**, 351-375, (2010).
2. Yamauchi, H. *et al.* Inflammatory breast cancer: what we know and what we need to learn. *Oncologist* **17**, 891-899, (2012).
3. Dawood, S. *et al.* International expert panel on inflammatory breast cancer: consensus statement for standardized diagnosis and treatment. *Ann Oncol* **22**, 515-523, (2011).
4. Hance, K. W., Anderson, W. F., Devesa, S. S., Young, H. A. & Levine, P. H. Trends in inflammatory breast carcinoma incidence and survival: the surveillance, epidemiology, and end results program at the National Cancer Institute. *J Natl Cancer Inst* **97**, 966-975, (2005).
5. Diessner, J. *et al.* Identifying the impact of inflammatory breast cancer on survival: a retrospective multi-center cohort study. *Arch Gynecol Obstet* **292**, 655-664, (2015).
6. Warren, L. E. *et al.* Inflammatory Breast Cancer: Patterns of Failure and the Case for Aggressive Locoregional Management. *Ann Surg Oncol* **22**, 2483-2491, (2015).
7. Woodward, W. A. Inflammatory breast cancer: unique biological and therapeutic considerations. *Lancet Oncol* **16**, e568-576, (2015).
8. Bertucci, F., Finetti, P., Birnbaum, D. & Viens, P. Gene expression profiling of inflammatory breast cancer. *Cancer* **116**, 2783-2793, (2010).
9. Bertucci, F. *et al.* Gene expression profiles of inflammatory breast cancer: correlation with response to neoadjuvant chemotherapy and metastasis-free survival. *Ann Oncol* **25**, 358-365, (2014).
10. Van Laere, S. J. *et al.* Uncovering the molecular secrets of inflammatory breast cancer biology: an integrated analysis of three distinct affymetrix gene expression datasets. *Clin Cancer Res* **19**, 4685-4696, (2013).
11. Nguyen, D. M. *et al.* Molecular heterogeneity of inflammatory breast cancer: a hyperproliferative phenotype. *Clin Cancer Res* **12**, 5047-5054, (2006).
12. Dressman, H. K. *et al.* Gene expression profiles of multiple breast cancer phenotypes and response to neoadjuvant chemotherapy. *Clin Cancer Res* **12**, 819-826, (2006).
13. Masuda, H. *et al.* Comparison of molecular subtype distribution in triple-negative inflammatory and non-inflammatory breast cancers. *Breast Cancer Res* **15**, R112, (2013).
14. Masuda, H. *et al.* Long-term treatment efficacy in primary inflammatory breast cancer by hormonal receptor- and HER2-defined subtypes. *Ann Oncol* **25**, 384-391, (2014).
15. Raghav, K. *et al.* Inflammatory Breast Cancer: A Distinct Clinicopathological Entity Transcending Histological Distinction. *PLoS One* **11**, e0145534, (2016).
16. Marrakchi, R. *et al.* Expression of WISP3 and RhoC genes at mRNA and protein levels in inflammatory and noninflammatory breast cancer in Tunisian patients. *Cancer Invest* **28**, 399-407, (2010).

17. van Golen, K. L. *et al.* A novel putative low-affinity insulin-like growth factor-binding protein, LIBC (lost in inflammatory breast cancer), and RhoC GTPase correlate with the inflammatory breast cancer phenotype. *Clin Cancer Res* **5**, 2511-2519, (1999).
18. van Golen, K. L. *et al.* Mitogen activated protein kinase pathway is involved in RhoC GTPase induced motility, invasion and angiogenesis in inflammatory breast cancer. *Clin Exp Metastasis* **19**, 301-311, (2002).
19. Van den Eynden, G. G. *et al.* Validation of a tissue microarray to study differential protein expression in inflammatory and non-inflammatory breast cancer. *Breast Cancer Res Treat* **85**, 13-22, (2004).
20. Ridley, A. J. Rho proteins and cancer. *Breast Cancer Res Treat* **84**, 13-19, (2004).
21. Ridley, A. J. RhoA, RhoB and RhoC have different roles in cancer cell migration. *J Microsc* **251**, 242-249, (2013).
22. Narumiya, S., Tanji, M. & Ishizaki, T. Rho signaling, ROCK and mDia1, in transformation, metastasis and invasion. *Cancer Metastasis Rev* **28**, 65-76, (2009).
23. Roussos, E. T., Condeelis, J. S. & Patsialou, A. Chemotaxis in cancer. *Nat Rev Cancer* **11**, 573-587, (2011).
24. Kleer, C. G. *et al.* RhoC-GTPase is a novel tissue biomarker associated with biologically aggressive carcinomas of the breast. *Breast Cancer Res Treat* **93**, 101-110, (2005).
25. Wu, M., Wu, Z. F., Rosenthal, D. T., Rhee, E. M. & Merajver, S. D. Characterization of the roles of RHOC and RHOA GTPases in invasion, motility, and matrix adhesion in inflammatory and aggressive breast cancers. *Cancer* **116**, 2768-2782, (2010).
26. Rosenthal, D. T. *et al.* RhoC impacts the metastatic potential and abundance of breast cancer stem cells. *PLoS One* **7**, e40979, (2012).
27. Joglekar, M., Elbazanti, W. O., Weitzman, M. D., Lehman, H. L. & van Golen, K. L. Caveolin-1 mediates inflammatory breast cancer cell invasion via the Akt1 pathway and RhoC GTPase. *J Cell Biochem* **116**, 923-933, (2015).
28. Boersma, B. J. *et al.* A stromal gene signature associated with inflammatory breast cancer. *Int J Cancer* **122**, 1324-1332, (2008).
29. Mantovani, A. & Sica, A. Macrophages, innate immunity and cancer: balance, tolerance, and diversity. *Curr Opin Immunol* **22**, 231-237, (2010).
30. Qian, B. Z. & Pollard, J. W. Macrophage diversity enhances tumor progression and metastasis. *Cell* **141**, 39-51, (2010).
31. Condeelis, J. & Pollard, J. W. Macrophages: obligate partners for tumor cell migration, invasion, and metastasis. *Cell* **124**, 263-266, (2006).
32. Joyce, J. A. & Pollard, J. W. Microenvironmental regulation of metastasis. *Nat Rev Cancer* **9**, 239-252, (2009).
33. van Golen, K. L., Wu, Z. F., Qiao, X. T., Bao, L. & Merajver, S. D. RhoC GTPase overexpression modulates induction of angiogenic factors in breast cells. *Neoplasia* **2**, 418-425, (2000).

34. Seruga, B., Zhang, H., Bernstein, L. J. & Tannock, I. F. Cytokines and their relationship to the symptoms and outcome of cancer. *Nat Rev Cancer* **8**, 887-899, (2008).
35. de Andres, P. J. *et al.* Increased levels of interleukins 8 and 10 as findings of canine inflammatory mammary cancer. *Vet Immunol Immunopathol* **152**, 245-251, (2013).
36. Kozlowski, L., Zakrzewska, I., Tokajuk, P. & Wojtukiewicz, M. Z. Concentration of interleukin-6 (IL-6), interleukin-8 (IL-8) and interleukin-10 (IL-10) in blood serum of breast cancer patients. *Rocz Akad Med Bialymst* **48**, 82-84, (2003).
37. Cohen, E. N. *et al.* Inflammation Mediated Metastasis: Immune Induced Epithelial-To-Mesenchymal Transition in Inflammatory Breast Cancer Cells. *PLoS One* **10**, e0132710, (2015).
38. Mohamed, M. M. *et al.* Cytokines secreted by macrophages isolated from tumor microenvironment of inflammatory breast cancer patients possess chemotactic properties. *Int J Biochem Cell Biol* **46**, 138-147, (2014).
39. Mohamed, M. M., Al-Raawi, D., Sabet, S. F. & El-Shinawi, M. Inflammatory breast cancer: New factors contribute to disease etiology: A review. *J Adv Res* **5**, 525-536, (2014).
40. Kao, J. *et al.* Molecular profiling of breast cancer cell lines defines relevant tumor models and provides a resource for cancer gene discovery. *PLoS One* **4**, e6146, (2009).
41. Radzun, H. J., Parwaresch, M. R., Sundstrom, C., Nilsson, K. & Eissner, M. Monocytic origin of the human hematopoietic cell line U-937 and its convertibility to macrophages evidenced by isoenzyme mapping. *Int J Cancer* **31**, 181-186, (1983).
42. Yue, H. H. *et al.* Expression of CD147 on phorbol-12-myristate-13-acetate (PMA)-treated U937 cells differentiating into foam cells. *Arch Biochem Biophys* **485**, 30-34, (2009).

Chapter 4

Nanoroughened Adhesion-based Capture of Circulating Tumor Cells with Heterogeneous Expression and Metastatic Characteristics

This chapter has been accepted for publication in BMC Cancer.

Chapter Summary

After cancer cells successfully intravasate, they enter the circulation. At this state in the metastatic series of sieves, they are called circulating tumor cells (CTCs) and are relatively easy to access for study via a simple blood draw. However, the challenge resides in their isolation as they are by far the rarest cell found in whole blood. Since intravasation and other metastatic sieves are mechanical in nature, in Chapter 4 we explore the possibility of harnessing physical property differences between the cancer cells and normal blood cells as a means for their capture. CTCs have shown prognostic relevance in many cancer types. However, the majority of current CTC capture methods rely on positive selection techniques that require a priori knowledge about the surface protein expression of disseminated CTCs, which are known to be a dynamic population. We developed a microfluidic CTC capture chip that incorporated a nanoroughened glass substrate for capturing CTCs from blood samples. Our

CTC capture chip utilized the differential adhesion preference of cancer cells to nanoroughened etched glass surfaces as compared to normal blood cells and thus did not depend on the physical size or surface protein expression of CTCs. The microfluidic CTC capture chip was able to achieve a superior capture yield for both EpCAM+ and EpCAM- cancer cells in blood samples. Additionally, the microfluidic CTC chip captured CTCs undergoing TGF-β-induced epithelial to mesenchymal transition with dynamically down-regulated EpCAM expression. In a mouse model of human breast cancer using EpCAM positive and negative cell lines, the number of CTCs captured correlated positively with the size of the primary tumor and was independent of their EpCAM expression. Furthermore, in a syngeneic mouse model of lung cancer using cell lines with differential metastasis capability, CTCs were captured from all mice with detectable primary tumors independent of the cell lines' metastatic ability.

Introduction

While progress has been made on the prevention and treatment of primary cancers, metastases to distant sites remain a major clinical challenge and the main cause of death for the majority of cancer patients [1]. Thus attention has shifted toward a better understanding of the metastatic process in order to address the mortality of patients with metastatic lesions. The spread of cancer systemically relies upon the critical step of the hematogenous spread of cancer cells [2]. These circulating tumor cells (CTCs) in the bloodstream are shed from primary and metastatic lesions and are believed to be key agents in the

metastatic process [2-4]. Therefore, capturing CTCs is not only important to understand the determinants of the metastatic fate of cancer cells, but also directly yields clinically relevant information as studies on CTCs have shown a general, but not complete, negative association between CTC counts and clinic outcomes [5-7]. The challenge being as a tumor progresses through the metastatic series of sieves, cancer cells are known to express diverse molecular phenotypes in a dynamic fashion, which complicates the isolation of CTCs for further study [6,8-13]. Moreover, other cells such as fibroblasts and non-cancerous epithelial cells are also shed into the circulation further complicating the identification of the true potentially metastatic cells.

The most widely used methods for CTC capture have relied upon tumors' cell of origin and utilized antibodies against tissue specific surface markers, notably epithelial cell adhesion molecule (EpCAM), which is expressed by epithelial cells [14-21]. However, numerous studies have demonstrated that the EpCAM antibody-based positive selection method is imperfect, as EpCAM expression on cancer cells varies not only from patient to patient but also within the same patient over time [6,8,9,11,12]. Furthermore, studies have demonstrated that epithelial-specific markers are selectively partially or completely down-regulated over the course of tumor dissemination through the epithelial-to-mesenchymal transition (EMT) [10,13]. Other CTC capture methods utilize size-based selection, as cancer cells are believed to be generally larger than hematopoietic and other shed cells and thus amenable to filtration or centrifugation. However, CTCs of various sizes,

including some smaller than leukocytes, have been reported recently [22-24]. The major challenge of CTC isolation is the extreme rarity of CTCs, even in patients with advanced cancer. This is especially evident when using negative selection techniques which deplete the undesired leukocyte population using antibodies against CD45, a leukocyte cell surface marker. Thus, because of the rarity of CTCs, it is difficult for negative selection techniques alone to achieve satisfactory yields for CTC capture [25,26].

Along the complex and dynamic progression through the series of metastatic sieves there is however an important point of convergence. The intravasation step into blood vessels by certain cancer cells within a tumor is a mechanically focused process by its very nature, and only those cells capable of behaving in a precise biomechanical way will successfully enter the bloodstream as live cells [27-29]. The mechanical phenotype of a cancer cell results from the integration of multidimensional and heterogeneous factors such as cell intrinsic genetic expression and epigenetic regulation and cancer cell extrinsic signals from cytokines, growth factors, and extracellular matrix proteins as well as interactions involving non-cancerous immune and stromal cells [27,30]. Given these complex inputs into the cancer cell phenotype, we set out to develop a method for CTC capture that does not rely upon any one single facet of this complex set of determinants, such as surface marker expression, but instead relies upon an output that reflects the integration of the multitude of signaling pathways experienced by a spreading cancer cell.

To this end, we developed a method that captures CTCs based on their differential capability to selectively adhere to a nanoroughened glass surface as compared to normal blood cells. In our prior work [31], we described that a nanorough glass substrate generated by reactive-ion etching (RIE) without any positive-selection antibodies exhibits significantly improved cancer cell capture efficiency owing to enhanced adherent interactions between the nanoscale topological features on the glass substrate and the nanoscale cellular adhesion apparatus. In our prior work, this nanoroughened glass substrate was employed to recover cancer cells spiked in blood samples, in a fixed device setting, with capture efficiencies of over 90% for different cancer cell lines [31]. Expanding on this proof-of-concept work, we hypothesized that further improvements in CTC capture performance and blood sample throughput could be achieved by using a confining microfluidic environment around the nanoroughened glass substrate to promote cell-substrate interactions for highly efficient CTC capture.

Herein we introduce our new microfluidic CTC capture platform and demonstrate its utility in recovering cancer cells with heterogeneous molecular properties and those obtained from two mouse models of cancer. Our microfluidic CTC capture platform integrates two functional components: 1) a RIE-generated nanoroughened glass substrate with nanoscale topological structures to enhance adherent interactions between the glass substrate and cancer cells, and 2) an overlaid polydimethylsiloxane (PDMS) chip with a low profile microfluidic capture

chamber that promotes CTC-substrate contact frequency. In this work we showed that the microfluidic CTC capture chip could capture > 80% of breast and lung cancer cells spiked in whole blood samples independent of the cell lines' EpCAM expression. The microfluidic CTC capture chip also captured equally well A549 lung cancer cells in their epithelial- or mesenchymal-like state before and after transforming growth factor beta (TGF-β)-induced EMT. To further demonstrate the clinical utility of the microfluidic CTC capture chip, we collected whole blood from mice with breast cancer orthotopic xenografts and demonstrated excellent label-free CTC capture efficiency by the microfluidic CTC capture chip. More importantly, in a syngeneic mouse model of lung cancer utilizing cell lines with known metastatic and non-metastatic capabilities, CTCs were detected in all the mice with a detectable primary tumor independent of the metastatic propensity of the cell line implanted. This highlights the fact that not all CTCs are capable of forming and proliferating as metastases and our newly developed microfluidic CTC capture device is able to recover this less metastatically potent population as well.

Results

Capture of cancer cells independent of surface protein expression

We have recently developed a simple yet precisely controlled method to generate random nanoroughness on glass surfaces using reactive ion etching (RIE) [32]. RIE-based nanoscale roughening of glass surfaces is consistent with a process of ion-enhanced chemical reaction and physical sputtering [33]. In our

previous work, we have shown that bare glass surfaces treated with RIE for different periods of time can acquire different levels of roughness (as characterized by the root-mean-square roughness R_q; R_q = 1 - 150 nm) with a nanoscale resolution (Fig. 4.S1) [32]. To validate the efficiency of RIE-generated nanorough glass surfaces (Fig. 4.1 a) for the capture of cancer cells with different surface protein expression, three breast cancer cell lines, MCF-7 (EpCAM-positive, or EpCAM+), SUM-149 (EpCAM+), and MDA-MB-231 (EpCAM-negative, or EpCAM-) [34-36] spiked in minute amounts in culture medium (1,000 cells in 1 mL medium) as single cells were injected into the microfluidic CTC capture chip with either a smooth glass surface (R_q = 1 nm) or a nanoroughened glass surface (R_q = 150 nm) for 30 min. Quantitative analysis revealed that the capture yield of cancer cells, defined as the ratio of the number of cancer cells captured on the glass surface to the total number of cells initially seeded, was 85.7%, 80.9%, and 86.5% for MCF-7, SUM-149, and MDA-MB-231, respectively, for the nanorough glass surface with R_q = 150 nm (Fig. 4.1 b). In distinct contrast, experiments using the smooth glass surface with R_q = 1 nm showed drastically lower capture yields for MCF-7, SUM-149, or MDA-MB-231 cells (6.7% for MCF-7, 8.0% for SUM-149, and 8.7% for MDA-MB-231) (Fig. 4.1 b). We further performed cell capture assays using the EpCAM+ A549 lung cancer cell line [37] and observed a similarly significant enhancement of cancer cell capture yield by the nanoroughened glass surface (Fig. 4.1 b). Together, our results in Fig. 4.1 suggest a very strong propensity for cancer cells to adhere to RIE-generated nanorough glass surfaces regardless of the cells' EpCAM expression status, and

further support a superior efficiency of the label-free nanoroughened glass substrate for capturing CTCs.

Capture of cancer cells before and after TGF-β-induced epithelial-mesenchymal transition

Through the metastatic process, tumor cells are posited to undergo an EMT, which alters adhesive surface protein expression along with many other aspects of cellular behaviors [38,39]. During this EMT, in addition to acquiring a migratory and invasive phenotype, tumor cells express mesenchymal proteins and concomitantly lose epithelial markers including the expression of EpCAM [40]. To demonstrate specifically that the capture of cancer cells by the RIE-generated nanorough glass substrate was independent of a cancer cell's epithelial or mesenchymal state, we used the A549 cell culture model of TGF-β-induced EMT and spiked known quantities of pre- and post-EMT A549 cells (n = 40 - 10,000) into 500 μL lysed human blood (Fig. 4.2 a). After culture with TGF-β for 72 hr, A549 cells express significantly reduced levels of EpCAM mRNA (Fig. 4.S2) [41]. Yet despite these lung cancer cells' dynamic EpCAM expression, high capture yields were achieved when seeding the cells for 1 hr in the microfluidic CTC capture chip with a nanoroughened glass surface (R_q = 150 nm) for both pre- and post-EMT A549 lung cancer cells, even at extremely low cancer cell concentrations (80 cells mL^{-1}) (Fig. 4.2 b,c). Strong linear correlations between the number of cancer cells captured *vs.* the number of cancer cells initially loaded (n = 40 - 900) were observed for both pre- and post-EMT A549 cells (Fig.

4.2 b). Averaged across all cell concentrations assayed (80 - 20,000 cells mL^{-1}), capture yields were 89.4% ± 5.3% for post-EMT A549 cells and 89.2% ± 2.2% for pre-EMT A549 cells (Fig. 4.2 c, Fig. 4.S2). We further examined the effect of admixtures of pre- and post-EMT A549 cells on capture efficiency by varying the ratio of pre- and post-EMT A549 cells spiked in the same blood sample. Here 1,000 post-EMT A549 cells were mixed with 500 - 4,000 pre-EMT cells in 500 µL lysed blood to achieve a cell ratio from 2 : 1 to 1 : 4 (Fig. 4.2 d). Cell capture assays using the microfluidic CTC capture chip for 1 hr revealed that capture yield was not significantly affected by the relative proportions of pre- or post-EMT A549 cells with differing EpCAM expression and remained constant over the entire range of cell ratios of pre- and post-EMT A549 cells (Fig. 4.2 d). Together, our results in Fig. 4.2 support that the RIE-generated nanorough glass surfaces can achieve efficient capture of CTCs independently of the cancer cell's epithelial or mesenchymal state or EpCAM expression, demonstrating the applicability of the microfluidic CTC capture device for the capture and enumeration of rare tumor cells from heterogeneous cell samples and throughout a tumor's metastatic progression, even in the setting of a dynamic EMT process.

Capture of CTCs from a human breast cancer orthotopic xenograft mouse model

We next assayed the microfluidic CTC capture chip with a nanoroughened glass surface (R_q = 150 nm) using an orthotopic xenograft mouse model of breast cancer. To generate tumor xenografts (Fig. 4.3 a), 1×10^6 MDA-MB-231 (EpCAM-) or SUM-149 (EpCAM+) breast cancer cells were injected into the left

inguinal mammary fat pad of female Ncr nude mice [42]. When mice were euthanized to assess for tumor burden between 3 - 7 weeks of xenograft time, nearly the entire mouse blood volume (300 - 800 µL) was collected by cardiac puncture of the left ventricle from each mouse before assayed using the microfluidic CTC capture chip. CTCs, as defined by cytokeratin+, CD45-, DAPI+ staining (Fig. 4.3 b), were successfully captured from 11 out of 12 mice bearing tumor xenografts of MDA-MB-231 cells and from all 5 mice with tumor xenografts of SUM-149 cells (Table 4.1). Data pooled from both EpCAM+ and EpCAM- breast cancer mouse models showed that the number of CTCs captured by the microfluidic CTC capture chip ranged from 13 to 4,664 cells per 100 µL of blood and increased drastically over the 9-week period during tumor progression, correlating positively with an increase in tumor weight (Fig. 4.3 c-e).

Capture of CTCs from metastatic and non-metastatic syngeneic mouse models of lung cancer

We next sought to assay the microfluidic CTC capture chip using a syngeneic mouse model of lung cancer. Two well-defined mouse lung cancer cell lines (344SQ and 393P) with different metastatic capabilities were subcutaneously implanted in a syngeneic host. Even though 344SQ and 393P lung cancer cells have distinct metastatic potential, both cell lines are derived from the same transgenic mouse model of lung cancer (p53 null, mutant Kras) [43,44]. The 344SQ lung cancer cells form metastatic lesions from spontaneous and experimental metastatic assays (subcutaneous implantation and tail vein injection), whereas

the 393P cell line does not metastasize by either assay [43]. However, both cell lines are capable of undergoing EMT in response to TGF-β with different kinetics and lose expression of epithelial markers [43,44].

After 6 weeks of subcutaneous tumor growth, mice were sacrificed and whole blood was collected *via* cardiac puncture before being processed with the microfluidic CTC capture chip with a nanoroughened glass surface (R_q = 150 nm) (Fig. 4.S3). Simultaneously, primary tumor volumes were measured and lungs were examined grossly for metastasis (Fig. 4.4 a). The 344SQ primary tumors grew significantly larger and shed more CTCs than metastasis-incompetent 393P tumors (Fig. 4.4 c-f). Using the microfluidic CTC capture chip, CTCs were detected in all 5 mice implanted with the metastatic 344SQ cell line (Fig. 4.4 d, Table 4.2). Similar to results from the breast cancer xenograft model, the number of CTCs detected using the microfluidic CTC capture chip showed a positive correlation with primary tumor size (Fig. 4.4 g). As expected, neither of the 2 mice implanted with the metastasis-incompetent 393P lung cancer cell line that formed palpable primary tumors (mice #6 and 7) had detectable metastatic lesions on their lungs (Fig. 4.4, Table 4.2). Surprisingly, however, we detected the presence of CTCs in all the mice, including those mice with metastasis incompetent 393P implants, with palpable primary tumors (Fig. 4.4 d). This observation clearly demonstrates that the presence of CTCs alone may not be indicative of the presence of metastatic disease.

Discussion

In this work, we have successfully developed a microfluidic CTC capture chip utilizing an RIE-generated nanorough glass surface as the substrate for efficient capture of CTCs regardless of cell size or surface protein expression. The microfluidic flow chamber incorporated on top of the nanorough glass surface promotes greater adhesive interactions of cancer cells with the nanorough glass substrate, thereby providing an effective strategy to achieve superior CTC capture efficiency. Other efforts that have been undertaken to isolate CTCs have primarily depended on either physical size differences between cancer cells and hematocytes or on the surface protein expression of either cancer cells or leukocytes [14-24]. In contrast, our CTC capture strategy leverages the differential adhesion preference to the RIE-generated nanorough glass surfaces between cancer cells and normal blood cells [31]. Mechanical properties of cancer cells represent a point of convergence in the metastatic series of sieves whereby only those cells within a tumor behaving in a precise biomechanical manner will successfully intravasate into the bloodstream. Since the mechanical phenotype of a cancer cell is the culmination of an array of heterogeneous factors both cell intrinsic and cell extrinsic [27,30], we posit that using a CTC capture system that is mechanically focused and adhesion-based will have greater success in detecting CTCs with different molecular signatures. This fact was supported by this present study as our adhesion-based microfluidic CTC capture chip was capable of capturing heterogeneous CTC populations independent of their EpCAM expression status or phenotypic state along the epithelial-mesenchymal

continuum. Specifically, with the microfluidic CTC capture device, we were able to achieve capture yields of > 80% for both EpCAM+ (MCF-7, SUM-149, A549) and EpCAM- (MDA-MB-231) cancer cell lines spiked in whole blood samples. Furthermore, the microfluidic CTC capture device attained high capture yields for both pre- and post-EMT lung cancer cells – and with equal affinity – in an *in vitro* model of induced EMT. Unbiased efficient capture of heterogeneous populations of CTCs regardless their EpCAM expression status is important, as EpCAM expression in tumor cells varies between patient to patient and within a patient over time as it is rapidly down-regulated during EMT. Similarly, many other surface markers on cancer cells are dynamically expressed over the course of tumor dissemination and metastatic progression [9-11,45,46]. Therefore, the precise surface marker expression of CTCs is a moving target during tumor progression, requiring capture methods targeting the whole CTC population to be independent of CTCs' surface marker expression.

Although there are several other microfluidic platforms capable of achieving high CTC capture efficiency, many of them depend on the use of positive selection agents (*i.e.* anti-EpCAM antibody or aptamer) [6,8,47,48]. These methods inherently require a priori assumption about the surface protein expression of CTCs that have been proven to be a dynamic and inconsistent population [6,8]. Some tumor cells may shed from the primary tumor and enter the bloodstream after undergoing the EMT process and losing their epithelial properties [39,49]. It has been proposed that the EMT process may additionally cause a series of other

CTC feature changes apart from the loss of epithelial properties, such as enhanced invasiveness and elevated resistance to apoptosis [50]. In agreement with this, a recent study has revealed dynamic changes of epithelial and mesenchymal compositions of CTCs with disease progression among patients with breast cancer [9]. Together, it is clear that some CTCs may experience phenotypic changes during tumor evolution and that the expression of EpCAM may be transient, so EpCAM expression based methods may potentially miss a substantial subset of CTCs [51,52]. Thus, any positive marker-based selection method can bias captured CTCs toward a population that is not representative of the CTCs in a patient [8,53]. The limited number of CTCs detected in patients even in late stages of metastases may well be a result of the use of CTC detection methods that heavily rely on EpCAM expression by CTCs [54-56]. New methods, like the microfluidic CTC capture chip using the label-free nanoroughened glass substrate, are critically needed to capture the entirety of heterogeneous CTC populations. In this work we have shown that by focusing on a biomechanical property dependent on a multitude of cellular signals, we can capture CTCs in different morphologic states and irrespective of EpCAM expression, thus our adhesion-based microfluidic CTC capture is marker and molecular independent.

To advance the clinical relevance of our microfluidic CTC capture chip further, we studied two *in vivo* models of breast and lung cancer. In orthotopic xenografts of EpCAM+ and EpCAM- breast cancer cell lines, clear correlations between tumor size and CTC number were observed for both MDA-MB-231 and SUM-149

xenografts, supporting the independence of our CTC capture methodology from cell surface marker expression. Our adhesion-based method for capturing heterogeneous CTC populations was further demonstrated by the use of a syngeneic lung cancer mouse model with differential metastatic capabilities. In this model, a positive correlation between primary tumor size and CTC number was observed. Interestingly, CTCs were also detected by our microfluidic CTC capture chip in 2 mice implanted with the non-metastatic 393P cell line. These mice did not grow overt lung metastases as did all the mice in the metastatic 344SQ cell line cohort. Thus, a population of CTCs incapable of forming metastases was detected by the microfluidic CTC capture chip, supporting that cellular signals and biological processes that allow for individual cell invasion and intravasation are not identical to those governing the seeding of fruitful metastases. It is important to understand the differences in the nature of these CTCs to determine their true significance in patient prognosis and in the clinical management of cancer, and our microfluidic CTC capture chip allows for both populations' study with its unbiased capture method based on the selective adhesion of cancer cells.

Materials and Methods

Cell culture

MCF-7 cells were maintained in high-glucose DMEM (Invitrogen); MDA-MB-231, 344SQ, and 393P cells in RPMI-1640 (Invitrogen); SUM-149 cells in Ham's F-12 w/L-glutamine (Fisher Scientific); and A549 cells in DMEM/F12 (Invitrogen).

MCF-7, MDA-MB-231, and SUM-149 media contained 0.5 μg mL^{-1} Fungizone, 5 μg mL^{-1} Gentamicin, 100 units mL^{-1} penicillin, and 100 μg mL^{-1} streptomycin (all Invitrogen). Additionally, SUM-149 cells were supplemented with 5 μg mL^{-1} Insulin and 1 μg mL^{-1} Hydrocortisone (both Sigma-Aldrich). A549, 344SQ, and 393P were supplemented with penicillin and streptomycin as above [43,44]. All media contained 10% fetal bovine serum (Atlanta Biological) except SUM-149 media which had 5%. SUM-149 cells were maintained at 37ºC with 10% CO_2 and all other cell lines at 37ºC with 5% CO_2. Fresh 0.25% trypsin-EDTA in phosphate buffered saline (PBS) was used to re-suspend cells. To induce the EMT, A549 cells were cultured with TGF-β at 5 ng mL^{-1} in serum free media for 72 hr. TGF-β is a potent inducer of EMT [57-60].

Chip fabrication

The microfluidic chip includes three components: a PDMS microfluidic chamber, an RIE-etched nanorough glass substrate, and a polyacrylate gadget to sandwich the chamber and substrate together. The microfluidic chamber was generated by replica molding using a Si mold fabricated using microfabrication. The detailed protocol for fabrication of the microfluidic CTC capture chip is described in the Supporting Materials Additional File.

Human blood specimens

Human blood specimens from healthy donors were collected in EDTA-containing vacutainers and were processed and assayed within 6 hr of collection. RBC

Lysis Buffer (eBioscience) was added to whole blood at a 10:1 *v*/*v* ratio. After incubation for 10 min at room temperature, the sample was diluted with 20 - 30 mL PBS to stop the lysing reaction and then centrifuged at 300 g for 10 min. After discarding the supernatant, the cell pellet was re-suspended in an equivalent volume of growth medium before use in CTC capture assays.

Mouse models of cancer

Care of animals and experimental procedures were according to the University of Michigan University Committee on Use and Care of Animals (UCUCA) approved protocols #PRO5314 and #PRO4116. To generate breast cancer xenografts, 1×10^6 MDA-MB-231 or SUM-149 cells were injected orthotopically into the left inguinal mammary fat pad of each female Ncr nude mouse (Taconic). The cells were suspended in 50 µL PBS and 50 µL Matrigel (Becton Dickinson). For the lung cancer studies, 1×10^6 cells of two mouse lung cancer cell lines (metastatic 344SQ and non-metastatic 393P) with differential metastatic capability [43,44] were subcutaneously implanted on either side of the dorsal flank in C57BL/6 mice (Taconic). Tumor growth was monitored weekly by caliper measurement with ellipsoid volumes calculated using ½ x length × width × height. Before euthanizing the mice, blood samples (0.3 - 0.8 mL) were collected *via* cardiac puncture under anesthesia to quantify CTCs.

CTC capture from in vitro spiked blood samples

Prior to CTC capture assays, cancer cells were first labeled with CellTracker Green (Invitrogen) before mixed with Δ9-DiI-stained (Invitrogen) leukocytes in lysed blood. The total cancer cell number in the blood sample was first quantified using a hemocytometer before the spiked sample was diluted using lysed whole blood to achieve the desired final CTC concentration. For the capture of pre- and post-EMT A549 cells in admixture, pre- and post-EMT A549 cells were first labeled with CellTracker Green (Invitrogen) and CellTracker Blue (Invitrogen), respectively, before mixed in cell culture medium.

The CTC capture chip was assembled and connected to a custom-built pressure control setup. The PDMS microfluidic chamber was washed with PBS for 5 min before 1.0 mL of spiked blood sample was loaded at a flow rate of 200 μL min^{-1} and incubated for 30 min - 1 hr at 37 °C with 5% CO_2. After the CTCs adhered, the chamber was washed with PBS then loaded with 4% paraformaldehyde (PFA; Electron Microscopy Sciences) in PBS for 20 min to fix captured CTCs. The nanorough glass substrate was then detached from the PDMS chamber and rinsed with PBS to remove floating cells. Adherent cells immobilized on the nanorough glass substrate were then imaged directly using a fluorescence microscope (Nikon Eclipse Ti-S, Nikon) equipped with an electron multiplying charge-coupled device (EMCCD) camera (Photometrics). To quantify CTC capture yield, the entire glass surface area was scanned on a motorized stage (ProScan III, Prior Scientific). Image processing software ImageJ (National Institutes of Health) was used to determine the number of CTCs.

CTC capture from in vivo mouse models

Capture of CTCs from mouse blood samples was performed using a procedure similar to the one employed for spiked blood samples. To visualize and quantify CTCs captured on the nanorough glass substrate, immunostaining was performed after the glass substrate was detached from the microfluidic chamber. After the PBS rinse as above, adherent cells were permeabilized with 0.25% Triton X-100 (Roche Applied Science) in PBS for 10 min. Fixed cells were incubated with 10% goat serum (Invitrogen) for 1 hr before another 1 hr incubation with primary antibodies to cytokeratin (FITC; BD Biosciences) and mouse CD45 (PE) and DAPI to identify cancer cells, leukocytes, and cell nuclei, respectively. CTCs were identified by: positive staining of anti-cytokeratin and DAPI; negative staining of anti-CD45; and appropriate morphometric characteristics including cell size, shape, and nuclear size. The researcher counting CTCs was blinded to the mouse group and tumor characteristics.

Statistical analysis

Student's two-sample, unpaired *t*-tests were calculated using GraphPad Prism software with *P*-values < 0.05 considered statistically significant.

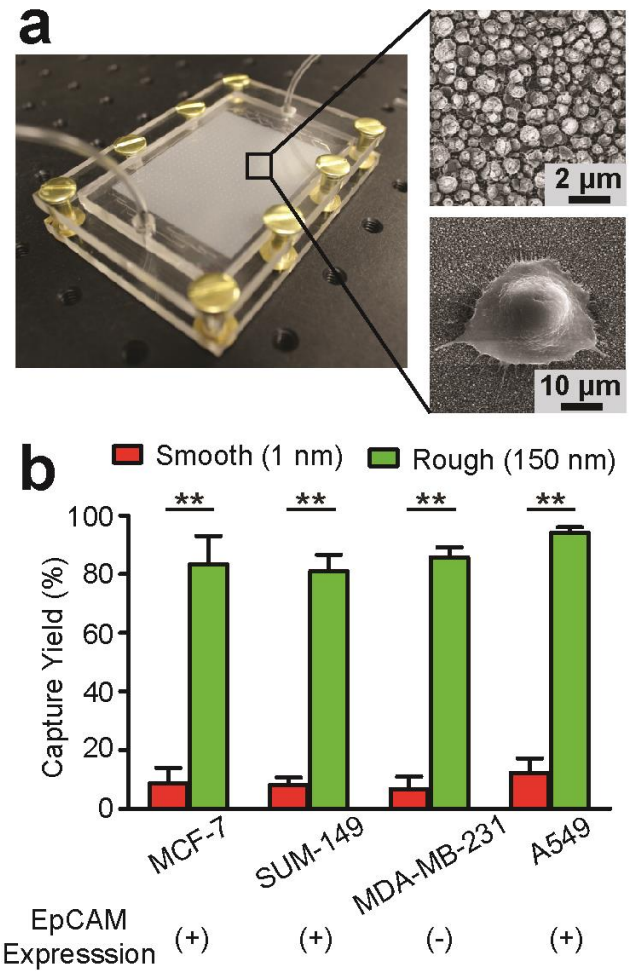

Figure 4.1. Nanotopography-based microfluidic chip for CTC capture. (a) Photo of the microfluidic CTC capture chip (left) and SEM images (right) showing the nanorough glass surface (top right, R_q = 150 nm) and a cancer cell adhered to the surface (bottom right). (b) Bar graph showing 30 min capture yield for breast cancer cells (MCF-7, MBA-MB-231, and SUM-149) and lung cancer cells (A549) using the capture chip with smooth (R_q = 1 nm) and nanorough (R_q = 150 nm) glass surfaces as indicated. For each cell type, 1,000 cells were spiked in 1 mL lysed human blood. EpCAM expression of each cell line is denoted below the graph. Error bars, s.e.m. (n = 4). **, $p < 0.01$.

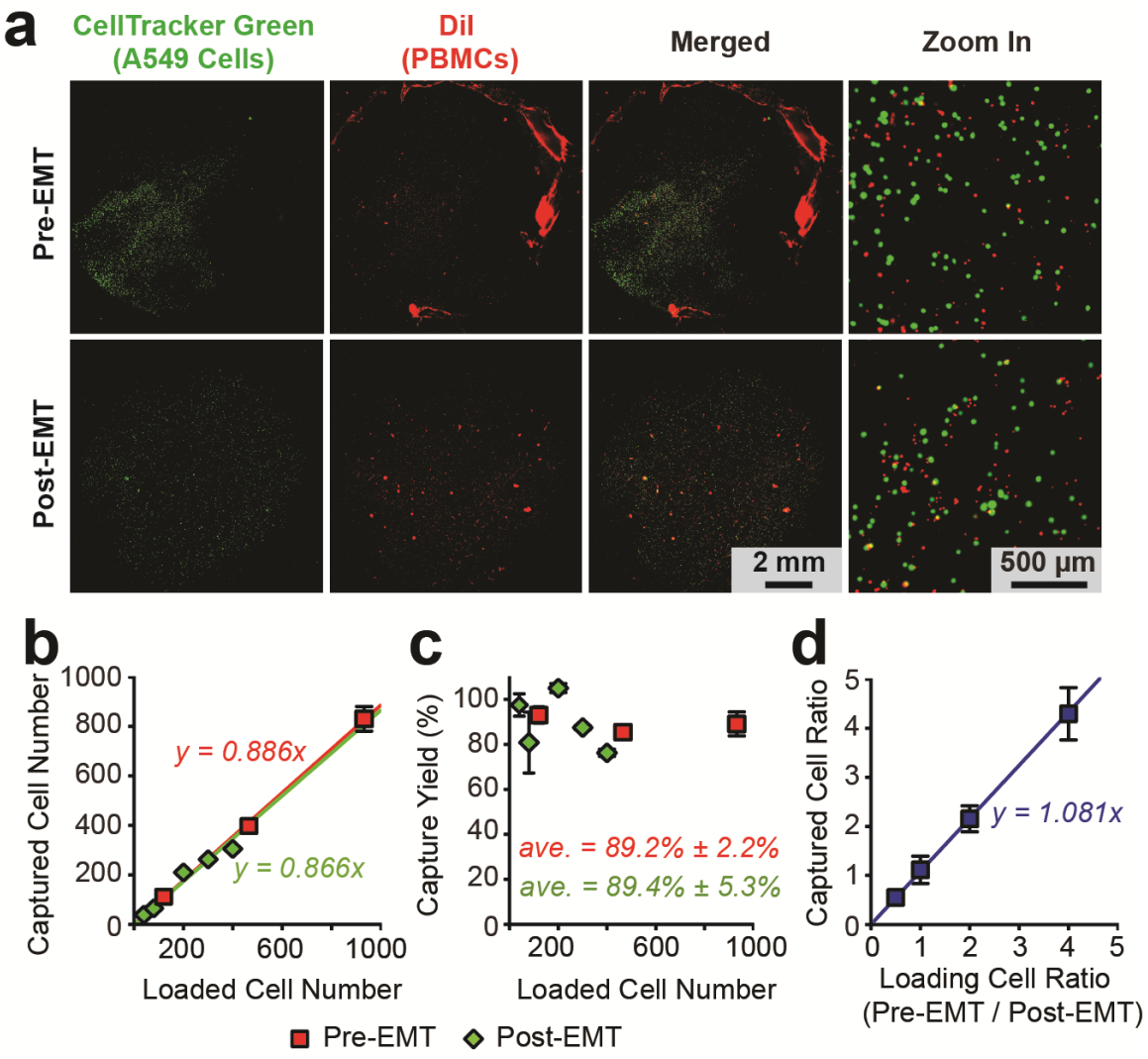

Figure 4.2. Capture of pre- and post-EMT lung cancer cells using the nanotopography-based microfluidic CTC capture chip. (a) Representative staining images showing pre- (top) and post-EMT (bottom) A549 cells captured on nanorough glass surfaces (R_q = 150 nm) 1 hr after cell seeding. 10,000 pre- and post-EMT A549 cells labeled with CellTracker Green were spiked in 500 μL lysed blood that was pre-stained with DiI to label peripheral blood mononuclear cells (PBMCs). (b,c) Regression analysis of 1 hr capture efficiency for pre- and post-EMT A549 cells (n = 40 - 900 spiked in 500 μL lysed blood) using the microfluidic CTC capture chip. The number of A549 cells captured (b) and the capture yield (c) is plotted as a function of the total number of A549 cells spiked in blood samples. (d) Ratio of pre- and post-EMT A549 cells captured 1 hr after cell seeding as a function of their ratio when spiked in blood samples. 1,000 post-EMT A549 cells were mixed with 500 - 4,000 pre-EMT cells in 500 μL lysed blood to achieve ratios from 2 : 1 to 1 : 4. Solid lines in b & d represent linear fitting. Error bars, s.e.m. (n > 4).

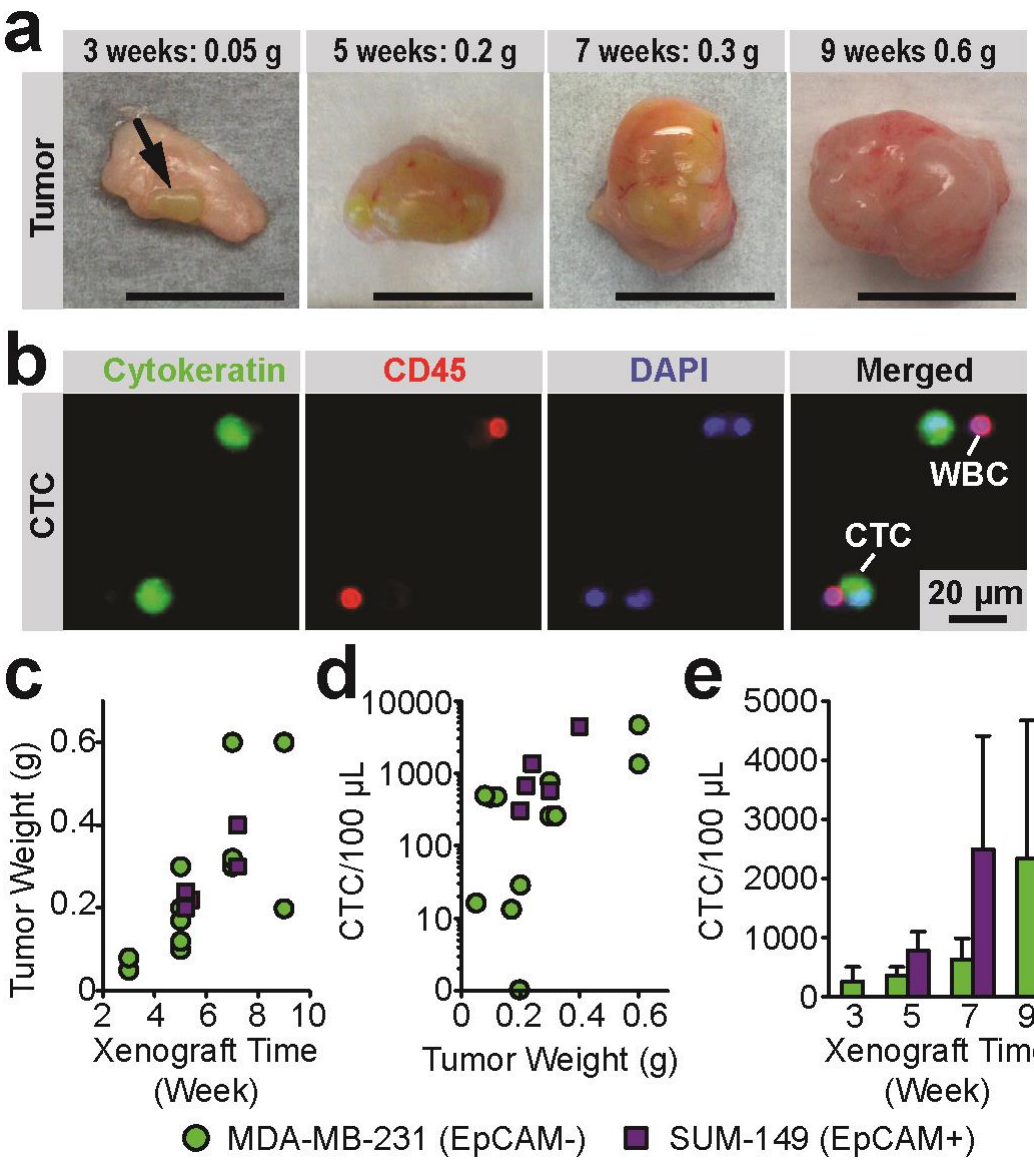

Figure 4.3. CTCs captured using the microfluidic CTC capture chip from mice with breast cancer orthotopic xenografts. (a) Photos of MDA-MB-231 xenografts, 1 cm scale bar. (b) Representative staining images showing CTCs captured on nanorough glass surfaces from mice with MDA-MB-231 tumor xenografts. Cells were co-stained for nuclei (DAPI; *blue*), cytokeratin (*green*), and CD45 (*red*). (c-e) Temporal changes in CTC number and tumor weight during tumor progression. Tumor weight (**c**) from mice with MDA-MB-231 and SUM-149 tumor xenografts as a function of xenograft time. Scatter plot (d) of CTC number per 100 µL blood *vs.* tumor weight. Bar plot (e) showing number of CTCs captured by the microfluidic CTC chip as a function of xenograft time. For each CTC capture assay, 300 - 800 µL blood samples were obtained *via* cardiac puncture. Error bars, s.e.m.

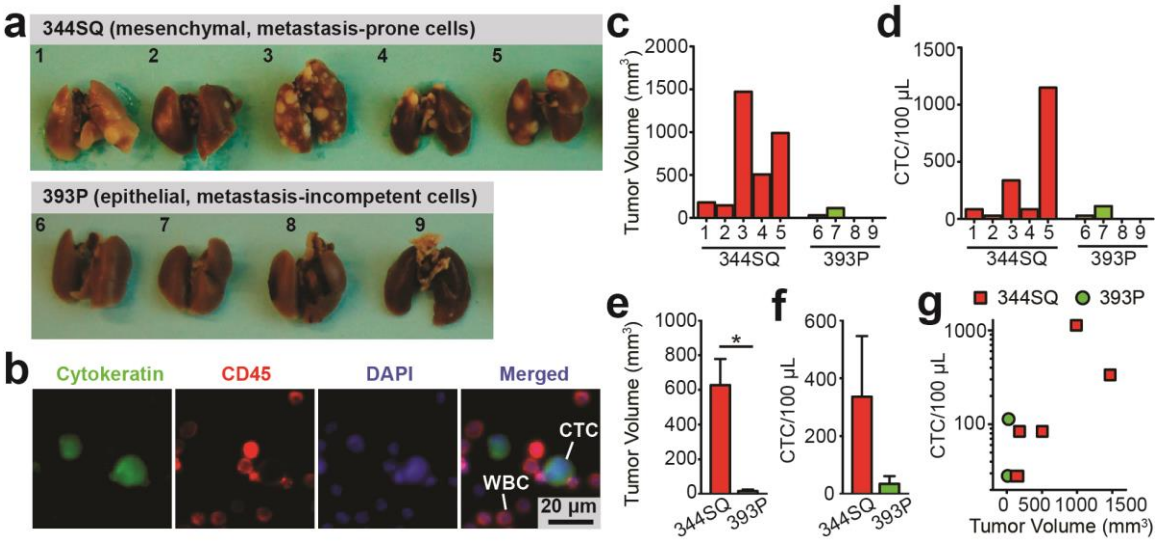

Figure 4.4. Capture of CTCs from metastatic and non-metastatic syngeneic mouse models of lung cancer. (a) Photos of lung metastases from 344SQ (top) and 393P (bottom) implants. Mouse 344SQ lung cancer cells are highly metastatic, while mouse 393P lung cancer cells are metastasis-incompetent. (b) Representative staining images showing CTCs captured on nanorough glass surfaces from mice implanted with 344SQ cells. Cells were co-stained for nuclei (DAPI; *blue*), cytokeratin (*green*), and CD45 (*red*). (c-g) Analysis of CTC number and tumor volume for mice with 344SQ and 393P tumor allografts. Bar plots show tumor volume (c) and CTC number per 100 µL blood (d) for individual mice. Bar plots showing average tumor volume (e) and average CTC number per 100 µL blood (f) of all mice. Scatter plot (g) of CTC number per 100 µL blood *vs.* tumor volume for mice with 344SQ and 393P tumor allografts. Mice were subcutaneously implanted with tumor allografts of 344SQ and 393P lung cancer cells. For each CTC capture assay, 350 - 600 µL blood samples were obtained *via* cardiac puncture. Error bars, s.e.m. *, $p < 0.05$.

Group	Sample	Xenograft Time	End tumor weight (g)	Collected blood volume (μL)	Captured CTCs (CTCs/100 μL)
MDA-MB-231	#1	3 weeks	0.05	800	16
	#2		0.08	800	498
	#3	5 weeks	0.20	800	29
	#4		0.17	800	13
	#5		0.30	800	772
	#6		0.10	800	468
	#7		0.12	500	478
	#8	7 weeks	0.60	800	1348
	#9		0.30	800	259
	#10		0.32	800	261
	#11	9 weeks	0.20	800	0
	#12		0.60	800	4664
SUM-149	#13	5 weeks	0.22	300	675
	#14		0.20	800	306
	#15		0.24	700	1366
	#16	7 weeks	0.30	500	579
	#17		0.40	700	4408

Table 4.1. Capture of CTCs from mice with orthotopic breast cancer xenografts.

MDA-MB-231 or SUM-149 xenografts of 1×10^6 cells were grown before blood collection and enumeration of CTCs.

Group	Sample	End tumor volume (mm^3)	Collected blood volume (µL)	Captured CTCs (CTCs/100 µL)
Metastasis-Prone (344SQ)	#1	179	500	84
	#2	144	500	28
	#3	1470	350	336
	#4	503.5	500	84
	#5	988	500	1148
Metastasis-Incompetent (393P)	#6	15.8	400	28
	#7	40	350	112
	#8	No tumor	500	0
	#9	No tumor	600	0

Table 4.2: Capture of CTCs from metastatic and non-metastatic syngeneic mouse models of lung cancer.

The metastasis-prone 344SQ or metastasis-incompetent 393P lung cancer cell lines were subcutaneously implanted into mice that were sacrificed 6 weeks after implantation with blood collected for circulating tumor cell quantification.

Supplemental Materials, Methods, and Figures

Fabrication of CTC capture chip

The CTC capture chip includes three components: a PDMS microfluidic chamber, a patterned nanorough glass substrate, and a polyacrylate gadget sandwiching the PDMS chamber and the patterned nanorough glass substrate. The glass substrate has dimensions of 50 mm × 76 mm and an effective nanoroughed region of 44 mm × 56 mm. The PDMS microfluidic chamber (height 400 μm, width 44 mm, length 56 mm) was produced by soft-lithography using a replicate on a silicon mold. Briefly, a silicon master for the microfluidic chamber was fabricated using photolithography and deep reactive ion etching (DRIE; STS Deep Silicon Etcher, Surface Technology Systems). The silicon master was then silanized with (tridecafluoro-1,1,2,2,-tetrahydrooctyl)-1-trichlorosilane vapor (United Chemical Technologies) for 4 hr under vacuum to facilitate subsequent release of the PDMS microfluidic chamber from the silicon master. PDMS prepolymer (Sylgard 184, Dow-Corning) was then prepared by thoroughly mixing the monomer with the curing agent (at a *w*/*w* ratio of 10:1), poured onto the silicon master and cured at 110 ºC for 1 hr. The fully cured PDMS chamber was peeled off from the silicon mold and the excess PDMS was trimmed using a razor blade and two through-holes were punched at the inlet and outlet for the tubing connections.

For the patterned nanorough glass substrates, a photoresist was first spin-coated on glass wafers (Borofloat 33, Plan Optik) and patterned using photolithography.

The glass wafer was then processed with RIE (LAM 9400, Lam Research) for different periods of time to generate nanoscale surface roughness (ranging from 1 nm to 150 nm) on the open regions of the glass wafer, where the photoresist had previously been developed and dissolved. The RIE process condition was selected as: SF_6 (8 sccm), C_4F_8 (50 sccm), He (50 sccm), Ar (50 sccm), chamber pressure (1.33 Pa), bias voltage (100 V), and radio frequency power (500 W), with the resulting glass etch rate as about 50 nm min^{-1}. After the RIE process, the photoresist was striped using solvents, and the glass wafer was cleaned using distilled water. The glass wafers were then cut into the designated size (50 mm × 76 mm) using an ADT7100 dicing saw (Advanced Dicing Technologies Ltd.).

To assemble the chip, a device holder composed of two polyacrylate plates was machined to sandwich the PDMS microfluidic chamber and the nanorough glass substrate using screws at the four corners and along the edges of the polyacrylate plates. Two through-holes were drilled on the top polyacrylate plate to align with the inlet and outlet holes of the PDMS microfluidic channel, thus allowing a convenient tubing connection to the microfluidic chamber. The complete assembly using the polyacrylate plates to hold the PDMS microfluidic chamber could withstand a pressure of about 50 psi without leaking.

SEM Specimen Preparation

Cell samples were washed three times with 50 mM Na-cacodylate buffer (pH 7.3; Sigma-Aldrich), fixed for 1 hr with 2% glutaraldehyde (Electron Microscopy

Sciences, Hatfield, PA) in 50 mM Na-cacodylate buffer, and dehydrated in a graded series of ethanol concentrations through 100% over a period of 1.5 hr. Dehydration in 100% ethanol was performed three times. Afterwards, dehydrated substrates were dried with liquid CO_2 using a super critical point dryer (Samdri®-PVT-3D, Tousimis, Rockville, MD). Samples were mounted on stubs, sputtered with gold palladium, observed and photographed under a Hitachi SU8000 Ultra-High Resolution SEM machine (Hitachi High Technologies America, Inc., Pleasanton, CA).

Surface Characterization Using Atomic Force Microscope

Nanoroughness of the glass surfaces was measured at room temperature with the Veeco NanoMan Atomic Force Microscope (AFM, Digital Instruments Inc., Santa Barbara, CA) using non-contact, tapping mode and standard Si tapping mode AFM tips with a scan rate of 1 Hz. The resulting map of the local surface height was represented using AFM topographs. The nanoroughness of each glass sample was characterized by the root mean square (RMS) roughness R_q of the local surface height over the scanned areas collected using the AFM topographs.

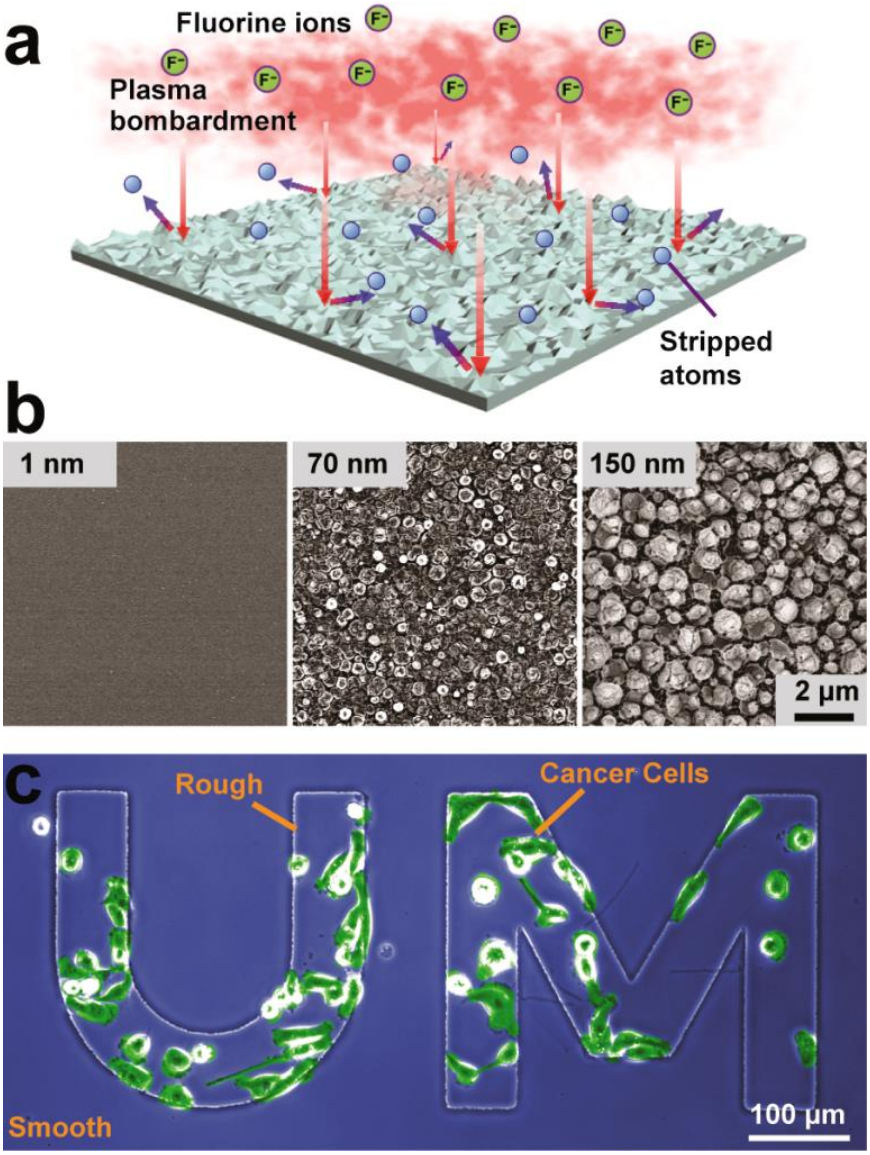

Figure 4.S1. Intrinsic nanotopological sensing for CTC capture. (a) Schematic of nanotopography generated by RIE on glass surfaces. (b) SEM images of glass surfaces with their RMS nanoroughness (R_q) indicated. (c) Phase-contrast micrograph showing MDA-MB-231 cells selectively adhering to patterned nanorough letters (UM; R_q = 70 nm) on the glass surface 24 hr after cell seeding.

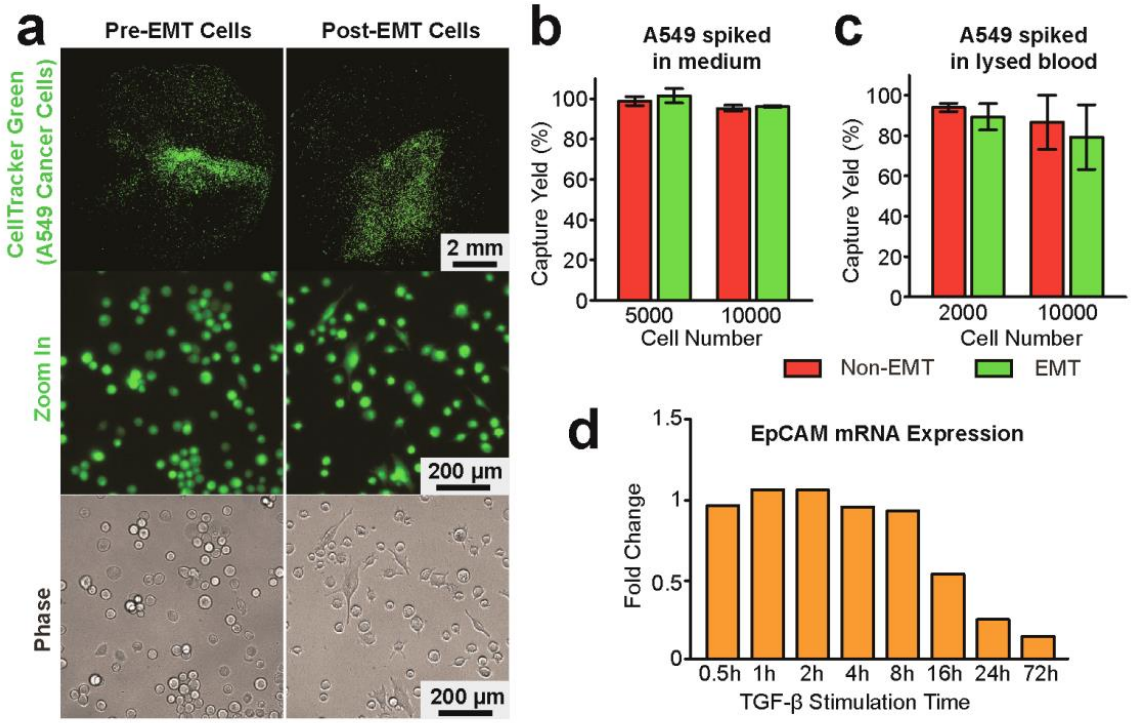

Figure 4.S2. Capture of pre-EMT and post-EMT lung cancer cells spiked in cell culture medium or lysed mouse blood. (a) Representative fluorescence images and zoom-in fluorescence and phase imgages showing known quantities (10,000) of pre-EMT and post-EMT cancer cells as indicated spiked in cell culture medium captured on nanorough glass surfaces (R_q = 150 nm) 1 hr after cell seeding. Target cancer cells were labeled with CellTracker Green before capture. (b) Capture yields of pre-EMT and post-EMT cancer cells in cell culture medium on nanorough glass surfaces (R_q = 150 nm) 1 hr after cell seeding. (c) Capture yields of pre-EMT and post-EMT cancer cells in lysed blood on nanorough glass surfaces (R_q = 150 nm) 1 hr after cell seeding. (d) Time-course of A549 EpCAM mRNA expression during TGF-□-induced EMT as assessed by microarray analysis using an Affymetrix U133 plus chip. Fold change shown relative to unstimulated cells. Error bars, s.e.m. (n > 4).

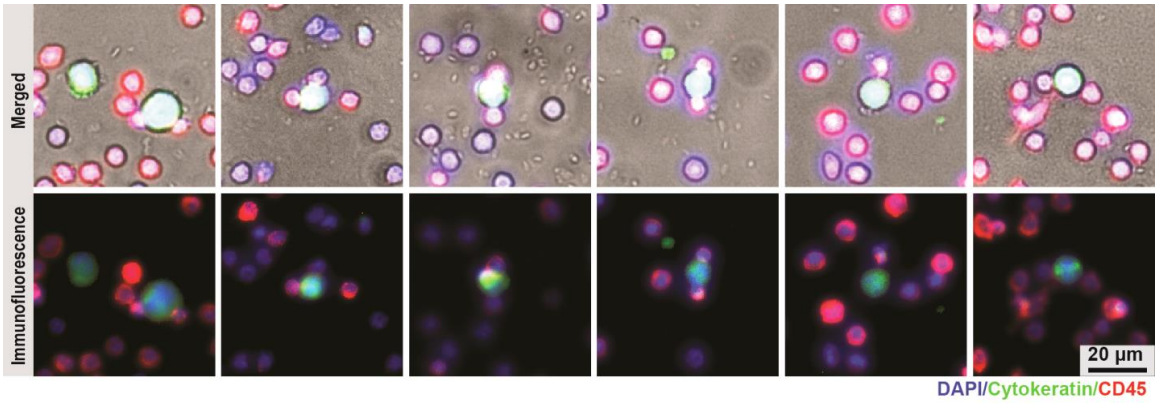

Figure 4.S3. Representative merged immunofluorescence and phase images of captured CTCs from mice with 344SQ lung tumor allografts. Cells were co-stained for nuclei (DAPI; *blue*), cytokeratin (*green*), and CD45 (*red*).

References

1. Siegel, R. L., Miller, K. D. & Jemal, A. Cancer statistics, 2015. *CA Cancer J Clin* **65**, 5-29, (2015).
2. Klein, C. A. Parallel progression of primary tumours and metastases. *Nature Reviews Cancer* **9**, 302-312, (2009).
3. Pantel, K., Alix-Panabières, C. & Riethdorf, S. Cancer micrometastases. *Nature reviews Clinical oncology* **6**, 339-351, (2009).
4. Ashworth, T. A case of cancer in which cells similar to those in the tumours were seen in the blood after death. *Aust Med J* **14**, 146-149, (1869).
5. Wicha, M. S. & Hayes, D. F. Circulating tumor cells: not all detected cells are bad and not all bad cells are detected. *Journal of Clinical Oncology* **29**, 1508-1511, (2011).
6. Pantel, K., Brakenhoff, R. H. & Brandt, B. Detection, clinical relevance and specific biological properties of disseminating tumour cells. *Nature Reviews Cancer* **8**, 329-340, (2008).
7. Smerage, J. B. *et al.* Circulating tumor cells and response to chemotherapy in metastatic breast cancer: SWOG S0500. *J Clin Oncol* **32**, 3483-3489, (2014).
8. Alix-Panabieres, C. & Pantel, K. Challenges in circulating tumour cell research. *Nat Rev Cancer* **14**, 623-631, (2014).
9. Yu, M. *et al.* Circulating breast tumor cells exhibit dynamic changes in epithelial and mesenchymal composition. *Science* **339**, 580-584, (2013).
10. Gorges, T. M. *et al.* Circulating tumour cells escape from EpCAM-based detection due to epithelial-to-mesenchymal transition. *BMC cancer* **12**, 178, (2012).
11. Rao, C. G. *et al.* Expression of epithelial cell adhesion molecule in carcinoma cells present in blood and primary and metastatic tumors. *Int J Oncol* **27**, 49-57, (2005).
12. Thurm, H. *et al.* Rare expression of epithelial cell adhesion molecule on residual micrometastatic breast cancer cells after adjuvant chemotherapy. *Clin Cancer Res* **9**, 2598-2604, (2003).
13. Kasimir-Bauer, S., Hoffmann, O., Wallwiener, D., Kimmig, R. & Fehm, T. Expression of stem cell and epithelial-mesenchymal transition markers in primary breast cancer patients with circulating tumor cells. *Breast Cancer Res* **14**, R15, (2012).
14. Nagrath, S. *et al.* Isolation of rare circulating tumour cells in cancer patients by microchip technology. *Nature* **450**, 1235-1239, (2007).
15. Talasaz, A. H. *et al.* Isolating highly enriched populations of circulating epithelial cells and other rare cells from blood using a magnetic sweeper device. *Proceedings of the National Academy of Sciences* **106**, 3970-3975, (2009).
16. Stott, S. L. *et al.* Isolation of circulating tumor cells using a microvortex-generating herringbone-chip. *Proceedings of the National Academy of Sciences* **107**, 18392-18397, (2010).

17. Wang, S. *et al.* Highly efficient capture of circulating tumor cells by using nanostructured silicon substrates with integrated chaotic micromixers. *Angewandte Chemie International Edition* **50**, 3084-3088, (2011).
18. Lee, S.-K. *et al.* Nanowire substrate-based laser scanning cytometry for quantitation of circulating tumor cells. *Nano letters* **12**, 2697-2704, (2012).
19. Adams, A. A. *et al.* Highly efficient circulating tumor cell isolation from whole blood and label-free enumeration using polymer-based microfluidics with an integrated conductivity sensor. *Journal of the American Chemical Society* **130**, 8633-8641, (2008).
20. Sekine, J. *et al.* Functionalized conducting polymer nanodots for enhanced cell capturing: the synergistic effect of capture agents and nanostructures. *Advanced Materials* **23**, 4788-4792, (2011).
21. Bichsel, C. A. *et al.* Diagnostic microchip to assay 3D colony-growth potential of captured circulating tumor cells. *Lab on a chip* **12**, 2313-2316, (2012).
22. Vona, G. *et al.* Isolation by size of epithelial tumor cells: a new method for the immunomorphological and molecular characterization of circulating tumor cells. *The American journal of pathology* **156**, 57-63, (2000).
23. Tan, S. J. *et al.* Versatile label free biochip for the detection of circulating tumor cells from peripheral blood in cancer patients. *Biosensors and Bioelectronics* **26**, 1701-1705, (2010).
24. Zheng, S. *et al.* 3D microfilter device for viable circulating tumor cell (CTC) enrichment from blood. *Biomedical microdevices* **13**, 203-213, (2011).
25. Yang, L. *et al.* Optimization of an enrichment process for circulating tumor cells from the blood of head and neck cancer patients through depletion of normal cells. *Biotechnology and bioengineering* **102**, 521-534, (2009).
26. Tkaczuk, K. H. R. *et al.* The significance of circulating epithelial cells in Breast Cancer patients by a novel negative selection method. *Breast cancer research and treatment* **111**, 355-364, (2008).
27. Wirtz, D., Konstantopoulos, K. & Searson, P. C. The physics of cancer: the role of physical interactions and mechanical forces in metastasis. *Nat Rev Cancer* **11**, 512-522, (2011).
28. Steeg, P. S. Tumor metastasis: mechanistic insights and clinical challenges. *Nat Med* **12**, 895-904, (2006).
29. Pantel, K. & Brakenhoff, R. H. Dissecting the metastatic cascade. *Nat Rev Cancer* **4**, 448-456, (2004).
30. Butcher, D. T., Alliston, T. & Weaver, V. M. A tense situation: forcing tumour progression. *Nat Rev Cancer* **9**, 108-122, (2009).
31. Chen, W. *et al.* Nanoroughened surfaces for efficient capture of circulating tumor cells without using capture antibodies. *ACS nano* **7**, 566-575, (2012).
32. Chen, W. *et al.* Nanotopography influences adhesion, spreading, and self-renewal of human embryonic stem cells. *ACS Nano* **6**, 4094-4103, (2012).
33. Metwalli, E. & Pantano, C. G. Reactive ion etching of glasses: Composition dependence. *Nuclear Instruments and Methods in Physics Research Section B: Beam Interactions with Materials and Atoms* **207**, 21-27, (2003).

34. Martowicz, A., Spizzo, G., Gastl, G. & Untergasser, G. Phenotype-dependent effects of EpCAM expression on growth and invasion of human breast cancer cell lines. *BMC cancer* **12**, 501, (2012).
35. Jordan, N. V. *et al.* SWI/SNF chromatin-remodeling factor Smarcd3/Baf60c controls epithelial-mesenchymal transition by inducing Wnt5a signaling. *Mol Cell Biol* **33**, 3011-3025, (2013).
36. Keller, P. J. *et al.* Mapping the cellular and molecular heterogeneity of normal and malignant breast tissues and cultured cell lines. *Breast Cancer Res* **12**, R87, (2010).
37. Watanabe, M. *et al.* A novel flow cytometry-based cell capture platform for the detection, capture and molecular characterization of rare tumor cells in blood. *J Transl Med* **12**, 143, (2014).
38. Thiery, J. P. Epithelial–mesenchymal transitions in tumour progression. *Nature Reviews Cancer* **2**, 442-454, (2002).
39. Kalluri, R. & Weinberg, R. A. The basics of epithelial-mesenchymal transition. *Journal of Clinical Investigation* **119**, 1420-1428, (2009).
40. Keshamouni, V. G. & Schiemann, W. P. Epithelial-mesenchymal transition in tumor metastasis: a method to the madness. *Future Oncol* **5**, 1109-1111, (2009).
41. Keshamouni, V. G. *et al.* Temporal quantitative proteomics by iTRAQ 2D-LC-MS/MS and corresponding mRNA expression analysis identify post-transcriptional modulation of actin-cytoskeleton regulators during TGF-beta-Induced epithelial-mesenchymal transition. *J Proteome Res* **8**, 35-47, (2009).
42. Eliane, J. P. *et al.* Monitoring serial changes in circulating human breast cancer cells in murine xenograft models. *Cancer Research* **68**, 5529-5532, (2008).
43. Gibbons, D. L. *et al.* Contextual extracellular cues promote tumor cell EMT and metastasis by regulating miR-200 family expression. *Genes & Development* **23**, 2140-2151, (2009).
44. Chen, L. *et al.* Metastasis is regulated via microRNA-200/ZEB1 axis control of tumour cell PD-L1 expression and intratumoral immunosuppression. *Nat Commun* **5**, 5241, (2014).
45. Longo, D. L. Tumor Heterogeneity and Personalized Medicine. *New England Journal of Medicine* **366**, 956-957, (2012).
46. Marusyk, A., Almendro, V. & Polyak, K. Intra-tumour heterogeneity: a looking glass for cancer? *Nature Reviews Cancer* **12**, 323-334, (2012).
47. Luo, X. *et al.* Isolation and molecular characterization of circulating melanoma cells. *Cell Rep* **7**, 645-653, (2014).
48. Yu, L. *et al.* Advances of lab-on-a-chip in isolation, detection and post-processing of circulating tumour cells. *Lab Chip* **13**, 3163-3182, (2013).
49. Kalluri, R. EMT: when epithelial cells decide to become mesenchymal-like cells. *Journal of Clinical Investigation* **119**, 1417-1419, (2009).
50. Kalluri, R. & Neilson, E. G. Epithelial-mesenchymal transition and its implications for fibrosis. *Journal of Clinical Investigation* **112**, 1776-1784, (2003).

51. Sieuwerts, A. M. *et al.* Anti-epithelial cell adhesion molecule antibodies and the detection of circulating normal-like breast tumor cells. *Journal of the National Cancer Institute* **101**, 61-66, (2009).
52. Van der Auwera, I. *et al.* Circulating tumour cell detection: a direct comparison between the CellSearch System, the AdnaTest and CK-19/mammaglobin RT-PCR in patients with metastatic breast cancer. *British Journal of Cancer* **102**, 276-284, (2009).
53. Baccelli, I. *et al.* Identification of a population of blood circulating tumor cells from breast cancer patients that initiates metastasis in a xenograft assay. *Nature biotechnology* **31**, 539-544, (2013).
54. Hayes, D. F. *et al.* Circulating tumor cells at each follow-up time point during therapy of metastatic breast cancer patients predict progression-free and overall survival. *Clin Cancer Res* **12**, 4218-4224, (2006).
55. Hartkopf, A. D., Wagner, P., Wallwiener, D., Fehm, T. & Rothmund, R. Changing levels of circulating tumor cells in monitoring chemotherapy response in patients with metastatic breast cancer. *Anticancer Res* **31**, 979-984, (2011).
56. Giuliano, M. *et al.* Circulating tumor cells as prognostic and predictive markers in metastatic breast cancer patients receiving first-line systemic treatment. *Breast Cancer Res* **13**, R67, (2011).
57. Kasai, H., Allen, J. T., Mason, R. M., Kamimura, T. & Zhang, Z. TGF-beta1 induces human alveolar epithelial to mesenchymal cell transition (EMT). *Respir Res* **6**, 56, (2005).
58. Kim, J. H. *et al.* Transforming growth factor beta1 induces epithelial-to-mesenchymal transition of A549 cells. *J Korean Med Sci* **22**, 898-904, (2007).
59. Chen, X. F. *et al.* Transforming growth factor-beta1 induces epithelial-to-mesenchymal transition in human lung cancer cells via PI3K/Akt and MEK/Erk1/2 signaling pathways. *Mol Biol Rep* **39**, 3549-3556, (2012).
60. Keshamouni, V. G. *et al.* Differential protein expression profiling by iTRAQ-2DLC-MS/MS of lung cancer cells undergoing epithelial-mesenchymal transition reveals a migratory/invasive phenotype. *J Proteome Res* **5**, 1143-1154, (2006).

Chapter 5

Functional and Biophysical Phenotyping of Inflammatory Breast Cancer Stem Cells

Chapter Summary

At each step in the metastatic series of sieves, cancer cells are required to behave in a precise mechanical manner if they are to successfully traverse to the next stage. Therefore, we hypothesized there could be a defining overarching biomechanical phenotype of these most aggressive cells that form metastasis. A distinct subpopulation of the cells that can effectively move through each metastatic sieve is composed of cancer stem cells (CSCs). CSCs, as defined through specific marker expression methods, have been shown to initiate tumorigenesis, have the capacity to self-renew, and initiate cancer metastasis in many cancer types. Although identification of CSCs through marker expression helps separate and define the CSC compartment, it does not directly provide information on how or why this cancer cell subpopulation is more tumorigenic and capable of bypassing the restrictive metastatic sieves. In this study, we comprehensively profiled the functional as well as biophysical characteristics of inflammatory breast cancer (IBC) CSCs at the single-cell level using multiple microengineered tools and traditional *in vitro* studies to delineate the live cell

phenotypic characteristics of the model of the most metastatic breast cancer subtype. IBC is the most aggressive and lethal form of breast cancer with two-thirds of patients presenting with axillary lymph node involvement and up to one-third of patients having distant metastases at initial diagnosis. Characterizing the functional behaviors of IBC CSCs such as cell migration, growth, adhesion, invasion, self-renewal, and differentiation is a direct approach to describe and understand IBC CSCs based upon their intrinsic properties, thus paving the way to determine therapeutic approaches to this most lethal subpopulation within IBC. Distinct biophysical properties of IBC CSCs such as cell deformability, adhesion strength, and traction force provide physical insights into why IBC has an enhanced propensity to metastasize compared to other breast cancers. Our multiparametric cellular phenotyping of functional and biophysical characteristics of IBC CSCs yields a new understanding of IBC's metastatic properties and how they might develop and be targeted for therapeutic interventions.

Introduction

Increasing evidence indicates that cancer cells with stem cell-like properties, termed "cancer stem cells" (CSCs), have the potential for self-renewal, differentiation, and tumorigenicity and play a major role in cancer recurrence and metastasis (Fig. 5.1 A)[1-3]. CSCs have been shown to initiate tumorigenesis in numerous cancer types[4-6], and recent studies have begun to define a role for CSCs in cancer metastasis as well[7-10]. CSCs have been characterized on the basis of their expression of particular surface markers[11,12] - such as CD133 and

CD44 - and also on the basis of cell adhesion molecules[13], cytoprotective enzymes (*e.g.* aldehyde dehydrogenase, ALDH)[14], and drug-efflux pumps (*e.g.* ABC transporters)[15]. CSCs, defined as the high ALDH-expressing subpopulation, have been shown to play a role in inflammatory and aggressive breast cancers[10]. Inflammatory breast cancer (IBC) is the most lethal form of breast cancer with 20 - 30% of patients presenting with metastasis at initial diagnosis[16,17]. Although RhoC GTPase and anaplastic lymphoma kinase (ALK) are implicated in the IBC phenotype, the underlying detailed mechanisms that allow IBC to be so aggressively metastatic from its inception are still under study, some of which have been explored in Chapter 3. In order to advance the field, an understanding of the physical attributes of CSCs that underlie their ability to execute the multiple events of metastases is important and has not been previously undertaken.

Here we analyzed both the intrinsic functional capabilities of IBC's CSC compartment as well as these cells' inherent biophysical properties that make them capable of early metastasis, essentially from the tumor's inception. During metastatic progression, cancer cells encounter complex biophysical environments consisting of different degrees of extracellular matrix (ECM) cross-linking[18], a differing ECM topology[19-21], mechanical heterogeneity within the ECM[20,22,23], as well as being exposed to shear flow and interstitial pressure[24-26]. In response, metastatic cancer cells must acquire unique biophysical characteristics in order to navigate through this dynamic microenvironment to

reach and proliferate in distant sites. As CSCs are believed to play critical roles in metastasis, it is highly possible that CSCs too will develop biophysical properties - such as increased deformability and decreased adhesion strength - necessary to traverse this environment and be capable, for example, of repopulating tumor masses following treatment.

Cell deformability (*i.e.* compliance under an applied load) has been postulated to play key roles in cancer cell invasiveness[24,27-30]. Cytoskeletal changes have been suggested to underlie mechanical differences observed in invasive cancer cells, consistent with a process of selection for cells that are able to squeeze into vessels by traversing walls (intravasate)[24,31,32]. Many studies have demonstrated a significantly higher degree of cell deformability for both cancer cell lines and primary tumors when compared to normal epithelial cells[27-29]. In the case of breast and ovarian cancers, the subpopulation of cancer cells with increased cell deformability has been shown to have a more malignant phenotype compared to stiffer cells[27,33]. Cell traction force is another key mechanical factor that has previously been shown to mediate cell functions[34-37] (*e.g.* migration, adhesion, and proliferation) as well as mechanotransduction. Therefore, cell traction forces may also be involved in cancer progression.

Previous studies have convincingly established the usefulness of biophysical characteristics for identifying more aggressive cancer cells in a label-free manner that is independent of current immunohistological methods[24,27,31,32,38,39]. Given

that IBC is the most aggressive and metastatic breast cancer, we sought to utilize quantitative techniques to characterize the IBC CSC compartment using a panel of assays to specifically profile the functional as well as biophysical characteristics of CSCs at the single-cell level. Such comprehensive, multiparametric phenotypic profiling of CSCs can provide useful insights into the qualities of IBC CSCs that increase their aggressiveness and propensity for tumorigenesis and metastasis as well as allow for studies of novel therapeutic interventions targeting CSCs functions.

Results

Functional phenotyping of IBC CSCs

High activity of ALDH within tumors has been associated with a poor prognosis in many cancers including breast[10,12,40,41], lung[42,43], liver[44], colon[14,45], pancreatic[46], ovarian[47], head and neck[48], and prostate[49] cancer. ALDH is a superfamily of detoxifying enzymes responsible for metabolizing a wide variety of intracellular aldehydes and plays an important role in multiple biological activities, including drug resistance, cell differentiation, and oxidative metabolism[50-52]. ALDH expression has been used as a predictive marker of CSCs for breast cancer[12,40,41,53] – including IBC[10] – and ALDH expression has proven to be more predictive than other established markers such as CD44+ / CD24- for identification of breast CSCs, as it has been shown that ALDH can identify cells with a greater resistance to chemotherapy[54,55].

In this study, breast CSCs with high ALDH enzymatic activity were isolated from an IBC cell line, SUM149, using an ALDEFLOUR assay (see Methods)[40]. SUM149 cells were stained for ALDH using the ALDEFLOUR reagent and sorted by flow cytometry. ALDEFLUOR treated cells quenched with the ALDH inhibitor diethylaminobenzaldehyde (DEAB) were used to set the ALDEFLUOR-positive FACS gate, containing less than 0.1% of DEAB-treated cells (Fig. 5.1 B). SUM149 cells above this 0.1% fluorescence threshold were sorted as ALDH-positive (ALDH+). ALDH negative (ALDH-) cells were sorted as the bottom percentage of cells that corresponded to the ALDH+ percentage (*i.e.* if 3.5% of cells were ALDH+, then the bottom 3.5% of cells were gated for the ALDH- population).

We performed comprehensive profiling to study functional phenotypes of ALDH+ IBC CSCs. First, the ratio of ALDH+ CSCs in the SUM149 cell line was quantified across multiple sortings to establish reliability (> 20). The proportion of ALDH+ cells in the SUM149 cell line was between 1 - 7%, with an average of 3.93% ± 1.84%, similar to what has been reported previously[10]. Interestingly, the ALDH+ CSC population maintained a dynamic equilibrium in the SUM149 cell line. In a purified ALDH+ population, the percentage of ALDH+ cells gradually decreased from 100% to the normal level (3 - 5%) for SUM149 cells over 3-5 days (data not shown), presumably by cell differentiation. Thus, the ALDH+ compartment was able to recapitulate the heterogeneity of the parent cell

population by maintaining an almost constant percentage of ALDH+ CSCs, consistent with previously reported results[10,56,57].

To study the tumorigenic and metastatic potential of ALDH+ IBC CSCs, *in vitro* invasion, migration, and proliferation assays were conducted. *In vitro* invasion assays were performed using the Biocoat Matrigel Invasion Chamber (see Methods) to examine the ability of cancer cells to invade through a Matrigel membrane under a serum gradient, mimicking the basement membrane invasion process in cancer metastasis. As shown in Fig. 5.1 C and D, ALDH+ IBC CSCs were more invasive compared to the ALDH- population and the unsorted SUM149 control.

To examine cell motility, the Cellomics Cell Motility kit was utilized to measure the migration area of ALDH+ and ALDH- cells. Each sorted cell type (ALDH+ and ALDH-) was plated in equal densities in 3 -5 wells of a 96-well plate that had previously been coated with blue fluorescent microbeads. After 24 hr of incubation, the area a cell migrated is represented by the negative space in the microbead carpet that has been pushed away or phagocytosed by the cell. This cell motility assay demonstrated a significantly higher motility for ALDH+ than ALDH- cells (Fig. 5.1 E,F), suggesting a more aggressive and motile phenotype for ALDH+ IBC CSCs.

To evaluate the growth rates of ALDH+ and ALDH- cells, these populations were quantified and compared with unsorted SUM149 controls using MTT assays (see Methods). Cell populations of flow-sorted ALDH+ and ALDH- cells and unsorted SUM149 controls were measured at 24 hr, 36 hr, 72 hr, and 96 hr post sorting. As shown in Fig. 5.1 G and H, ALDH+ cells had a slower growth rate and significantly longer cell doubling time compared to ALDH- cells and unsorted control cells. This slower growth rate for ALDH+ cells suggests that the IBC CSCs can maintain a semi-quiescent or slowly-cycling state, similar to the behavior of many adult stem cell types.

Cell deformability measurements for IBC CSCs

Our invasion assays demonstrated that ALDH+ cells had a greater capability to migrate through confined physical spaces, a process that necessitates significant cell shape and cytoskeleton changes. Thus, we hypothesized that there would be a concomitant difference in cell deformability between ALDH+ and ALDH- cells. Furthermore, at a key metastatic sieve, cell deformability has been postulated to play a key role in invasion through the basement membrane[31,32]. To explore potential differences in cell deformability between the ALDH+ IBC CSCs and ALDH- subpopulations, we utilized a microfluidics-based deformability microcytometer especially designed for highly-sensitive, high-throughput and label-free quantification of cell deformability at the single-cell level.

The microfluidic deformability microcytometer was made of poly-dimethylsiloxane (PDMS) and contained an array of identical funnel-shaped, long confining microchannels that served to automatically direct and trap individual live cancer cells within each channel (Fig. 5.2 A & Fig. 5.S1). The microchannel walls were pre-coated with Pluronic-127, a hydrophilic non-ionic surfactant, so that friction between the cell and the channel wall would be negligible. Within the deformability microcytometer, differential hydrodynamic pressure acting on individual cancer cells gradually pushes the cell down the funnel and, ultimately, the motion of the cell stops and the cell is trapped due to confining space of the funnel-shaped channel. For inert microfluidic channels where cell trapping is dictated by steric interactions between cancer cells and the channel wall, the penetration length (*L*) of an individual cancer cell into the channel is completely determined by its cell volume and cell deformability (Fig. 5.2 A,B). Thus, the cell deformability of each cancer cell can be calculated (see Methods) based upon known or measured parameters including pressure, cell volume, and the penetration length *L* (or the distance *d* between the position where the cell started to deform and the final trapped position in the channel).

We quantified the cell deformability of both ALDH+ and ALDH- SUM149 cells using the deformability microcytometer, with results showing that under the same differential hydrodynamic pressure across the confining microchannels, the average penetration length *L* of ALDH+ IBC CSCs was significantly greater than that of ALDH- cells, while the cell diameters of both populations were comparable

(Fig. 5.2 C,D). This suggested a greater deformability of ALDH+ IBC CSCs than ALDH- cells. We further performed correlative studies using single cell data for cell deformability and cell diameter. Our analysis in Fig. 5.2 E showed no strong correlation between cell deformability and cell diameter for either ALDH+ or ALDH- cells, suggesting that cell deformability is an intrinsic biophysical property regardless of cell size. Interestingly, deformability of ALDH+ cells was distributed across a relatively higher range than ALDH- cells (Fig. 5.2 E,F), pointing to a potential inherent propensity and ability of ALDH+ IBC CSCs to more readily undergo the necessary cytoskeletal rearrangement to intravasate across the basement membrane during invasion.

In addition to measurements for CSCs, we also compared the cell deformability of another non-inflammatory and less aggressive breast cancer cell line (MCF-7) with the normal-like breast epithelial cell line (MCF-10A). Our results showed that MCF-7 cells exhibited greater cell deformability than MCF-10A cells (Fig. 5.S1 C,D). Together, our data show that the small population of IBC CSCs possesses a greater degree of cell deformability than normal breast cancer cells.

Cell adhesion strength characterization for IBC CSCs

We conducted adhesion assays for SUM149 breast cancer cells to evaluate their ability to make stable physical contact with surfaces (Fig. 5.3 A,B). Three groups of SUM149 cancer cells - sorted ALDH+ cells, ALDH- cells, and an unsorted control – were seeded at the same density as single cells in polystyrene 48-well

cell culture plates. Three hours after cell seeding, floating cells were removed, and adherent cancer cells were stained with Calcein AM for visualization. Fluorescence images of stained cancer cells in the entire sample area were taken for quantification of the adhesion rate, defined as the ratio of the number of cells adhered to the surface to the total number of cells initially seeded per sample.

Quantitative analysis revealed that ALDH+ cells had a much lower adhesion rate compared to both the ALDH- population and unsorted control (Fig. 5.3 B). On average, the adhesion rate after 3 hr of cell seeding was 25.6% for ALDH+ cells, while for ALDH- cells and unsorted control cells the adhesion rates were 60.6% and 52.0%, respectively.

Our results in Fig. 5.3 A and B demonstrating a significant difference in the adhesion properties of ALDH+ and ALDH- cancer cells suggested the possibility that adhesion strength of cancer cells might similarly be correlated with ALDH expression as was cell deformability. To examine specifically the possibility of the IBC CSC compartment consisting of intrinsically less adherent cells, we developed a microfluidic cell adhesion assay for direct measurements of the adhesion strength of cancer cells (Fig. 5.3 C; see Methods). A low density of ALDH+ or ALDH- IBC cells was seeded uniformly inside the microfluidic channel for 12 hr before they were exposed to constant directional fluid shear (0.1 - 320 dyne cm^{-2}) for 3 min. We quantified the fraction of cancer cells remaining

adherent in the microfluidic channel after exposure to this sustained 3-min directional fluid shear. Our data demonstrated that indeed, the ALDH+ IBC CSCs that adhered to the microfluidic channel were only capable of withstanding much lower fluidic shear stresses than the ALDH- cells (Fig. 5.3 D,E). The adhesion strength of cancer cells, defined as the fluidic shear stress at which 50% of cancer cells initially adherent on the microfluidic channel detach after exposed to shear, was significantly lower for ALDH+ IBC CSCs than ALDH- cells (Fig. 5.3 F).

Together, our results in Fig. 5.3 demonstrated that adhesive properties could be quantitatively delineated and correlated with the ALDH-defined IBC CSC population in the SUM149 cell line. In summary, ALDH+ IBC cells had a decreased ability to adhere to a substrate and overall decreased adhesion strength.

Cell traction force measurements for IBC CSCs

The difference seen in cell adhesion properties between ALDH+ IBC CSCs and ALDH- cells implicated an involvement of actin cytoskeleton (CSK) and integrin-mediated focal adhesions that tether the actin CSK to the extracellular matrix. To investigate this hypothesis, we utilized an array of PDMS microposts as subcellular live-cell force sensors to quantify intracellular CSK contractile forces (Fig. 5.4 and Fig. 5.S2)[58-60]. This PDMS micropost array consists of hexagonally spaced, vertical, elastomeric posts fabricated using replica molding with PDMS

from microfabricated silicon masters (Fig. 5.4 A and Fig. 5.S2 A-D). After adhesive proteins are coated on the post tips using microcontact printing (Fig. 5.S2; see Methods), cells are able to adhere, spread out, and exert contractile forces that deflect the underlying posts (Fig. 5.4 A-D and Fig. 5.S2 C). Each post, therefore, functions as a cantilever and force sensor, capable of measuring local cellular traction force exerted at the post tip (Fig. 5.S2 E-G)[58-60].

We performed quantitative analysis of cell morphology and CSK contractility of SUM149 cells with the PDMS micropost array (Fig. 5.4 E,F). Our results revealed that the total cell traction force was significantly less for ALDH+ cells compared to ALDH- ones (Fig. 5.4 G). Previous studies have demonstrated that cell traction force generation can be confounded by a cell's footprint area[36,37,58]. To exclude the possibility that the decreased cell traction force for ALDH+ CSCs was simply caused by a variance in cellular area, we quantified cell spread area for SUM149 cells. Our results in Fig. 5.4 H showed no significant difference in cell spread area between ALDH+ and ALDH- cells. To further investigate the role of cell spread area in the generation of traction forces, we analyzed the total traction force of each cell normalized by its spread area (traction force per cell area), with results showing that the average traction force per cell area was lower for ALDH+ IBC CSCs compared to ALDH- SUM149 cells (Fig. 5.4 I). Hence, these results indicate that the smaller traction forces exerted by ALDH+ IBC CSCs *vs.* ALDH- cells are not linked to differences in cell spread area, but to other inherent cellular differences between the two populations. Consistent with

previous reports though[36,37,58], within the same group of cells (ALDH+ or ALDH-) the correlative plot (Fig. 5.4 J) of single-cell data of total traction force and cell spread area did show a strong linear correlation of increasing traction force with cell spread area. However, the slope of the linear correlation between the traction force and cell spread area was substantially less for ALDH+ cells than for ALDH- cells (0.13 nN μm^{-2} *vs.* 0.07 nN μm^{-2}), again indicating distinct biophysical properties of ALDH+ and ALDH- cells. Our traction force study in conjunction with the adhesion strength results indicate that ALDH+ and ALDH- cells have differential biophysical properties with the ALDH+ IBC CSCs being less adherent and exerting less contractile force. This may help explain the metastatic potential difference between the ALDH+ and ALDH- populations. Cells that are prone to forming strong connections with their surrounding ECM (ALDH- cells) may be less likely to successfully migrate away from the primary tumor[61].

Discussion

Cancer stem cells have been proven to initiate tumorigenesis and are the primary population of cells responsible for cancer metastasis in numerous cancer types[4-10]. Within IBC, the ALDH+ population has been shown to represent the tumorigenic and metastatic subpopulation[10], but detailed studies characterizing the IBC CSC's mechanical properties were lacking. ALDH expression is also negatively correlated with survival outcome[10], thus we postulated that the ALDH+ CSCs of IBC would exhibit distinct biomechanical properties that would help explain their extremely aggressive metastatic behavior. In our studies, we first

examined the migratory and invasive phenotypes of the ALDH+ population in an IBC cell line, SUM149. Utilizing *in vitro* cell motility and Matrigel invasion assays, we demonstrated a more aggressive phenotype for IBC CSCs, which covered a larger migration area and were more successful in invading through a basement membrane mimic. Furthermore, the ALDH+ population could recapitulate the parental cell line heterogeneity and was more slowly cycling than the ALDH- population. Both of these characteristics support the fact that the ALDH+ population comprises, or is contained within, the IBC CSC compartment. Although helpful, these studies only allowed identification of the appropriate group of cells in which to explore metastatic aggressiveness that is potentially derived from cellular mechanical properties. In order to more specifically ascertain and potentially explain the mechanical basis for the aggressive behavior of IBC CSC's, we undertook novel experiments and engineered devices targeted at quantitatively defining cells' mechanical properties.

This biophysical characterization of ALDH+ IBC CSCs revealed distinct biophysical properties that might mechanistically explain the functional differences seen between the IBC CSC and non-CSC population. These biophysical properties included a greater cell deformability, weaker adhesion strength, and less cellular traction force. This unique profile of biophysical characteristics associated with ALDH+ IBC CSCs could help explain how CSCs are better adapted than non-CSCs to successfully navigate through their dynamic microenvironment in the metastatic series of sieves.

In the first metastatic sieve encountered, decreased adhesion of IBC CSCs, as demonstrated by their lower measured adhesion strength, might indicate why these cells are able to migrate away from the primary tumor. The strongly adherent ALDH- cells might not be able to overcome their attachment, which is further supported by ALDH- cells' reduced migration capacity in our *in vitro* studies. Additionally, IBC CSCs, a highly metastatic cell population, showed significantly lower traction forces compared to their non-CSC counterparts, suggesting inherent differences in cell force generation correlated with aggressiveness. In the next sieves of the metastatic program, migrating cancer cells must invade through the basement membrane and squeeze through endothelial cell tight junctions during intravasation and extravasation. As measured in our assays, the greater capacity for deformation of ALDH+ cells suggests significant plasticity towards cytoskeletal changes or reorganization and underlying mechanical differences in IBC CSCs. This may account in part for their invasive capability to more successfully transit through a confining biophysical microenvironment. Cell deformability may thus be used as a label-free biophysical marker for identification and understanding of other CSCs in future studies.

Together, our study of IBC CSC's biophysical properties paints a picture where these cells are mechanically adapted to migrate and invade for successful completion of the metastatic series of sieves. At initial diagnosis, 60-80% of IBC

patients present with axillary lymph node involvement and 20-30% already have distant metastases[16,17]. Why IBC is so much more aggressive and metastatic than other breast cancers though is not definitively known. Previous studies have identified ALDH+ IBCs as key mediators of tumorigenesis and metastasis, and they are negatively correlated with survival[10]; however, the how and why have been left unstudied. Therefore, in this work we comprehensively profiled the functional as well as biophysical characteristics of IBC CSCs at the single-cell level using multiple microengineered tools. Such multiparametric cellular phenotypic profiling of CSCs can provide critical insight into the characteristics of these cells and their biomechanical adaptation for cancer metastasis, opening the door for the standardization of studies to potentially prognosticate the probability of metastatic growth and/or of therapies that target a tumor's unique biophysical signature associated with IBC CSCs.

Materials and Methods

Fabrication of PDMS microfluidic devices for cell deformability and adhesion strength measurements

Poly-dimethylsiloxane (PDMS) microfluidic devices for cell adhesion strength and deformability measurements were fabricated using soft lithography and replica molding. Briefly, a silicon master for microfluidic channels was fabricated using photolithography and deep reactive ion etching (DRIE; STS Deep Silicon Etcher, Surface Technology Systems, Newport, UK). The silicon master was then silanized with (tridecafluoro-1,1,2,2,-tetrahydrooctyl)-1-trichlorosilane vapor

(United Chemical Technologies, Bristol, PA) for 4 hr under vacuum to facilitate subsequent release of the PDMS microfluidic channel from the silicon master. PDMS prepolymer (Sylgard 184, Dow-Corning, Midland, MI) was then prepared by thoroughly mixing PDMS monomer with curing agent (with the *w* / *w* ratio of 10:1), poured onto the silicon master and cured at 110ºC for 30 min. The fully cured PDMS top layer was then peeled off from the silicon mold, and excess PDMS was trimmed using a razor blade. Through-holes were then punched in the PDMS top layer using a Harris Uni-Core Punch (GE Healthcare Whatman, Piscataway, NJ) to generate microfluidic inlet and outlet holes. The PDMS top layer was then bound to a coverslip substrate using an oxygen plasma-assisted bonding process (Plasma Prep II, West Chester, PA).

Fabrication and surface functionalization of PDMS micropost array

The PDMS micropost array was fabricated using DRIE and replica molding, as previously described[58]. The silicon micropost array master was first fabricated using photolithography and DRIE. The PDMS micropost array was then generated through a 'double casting' process (Fig. 5.S2 D). Briefly, the silicon master was first silanized with (tridecafluoro-1,1,2,2,-tetrahydrooctyl)-1-trichlorosilane vapor for 4 hr under vacuum to facilitate subsequent release of the negative PDMS mold from the silicon master. PDMS prepolymer was then prepared, poured onto the silicon master, and cured at 110ºC for 20 min. The fully cured negative PDMS mold was peeled off from the silicon mold, before activated with an oxygen plasma for 1 min and silanized with (tridecafluoro-

1,1,2,2,-tetrahydrooctyl)-1-trichlorosilane vapor for 24 hr. To generate the final PDMS micropost array, 1:10 ratio PDMS prepolymer was poured over the negative PDMS mold and degassed under vacuum for 10 min. A 25 cm × 25 cm cover glass, which served as the substrate for the PDMS micropost array, was then placed on top of the negative PDMS mold. After curing at 110ºC for 40 hr, the PDMS micropost array was peeled off from the negative mold to release the final PDMS micropost array. When peeling induced collapse of the PDMS microposts, we regenerated freestanding PDMS microposts by sonication in 100% ethanol for 30 sec followed by dry-release with liquid CO_2 using a critical point dryer. The PDMS micropost array used in this study had a post diameter of 1.83 μm, a height of 7.1 μm, and a post center-to-center distance of 4 μm.

Microcontact printing was used to functionalize the PDMS microposts with ECM proteins to promote cell attachment (Fig. 5.S2 D). Briefly, a flat 1:30 PDMS stamp was prepared and inked with collagen (BD Biosciences, San Jose, CA) at a saturating concentration of 50 mg mL^{-1} in distilled water for 1 hr at room temperature. The PDMS stamp was then thoroughly rinsed with distilled water and blown dry with nitrogen gas. In parallel, the PDMS micropost array was treated with ultraviolet (UV) ozone (UV-ozone cleaner; Jelight, Irvine, CA) for 7 min to ionize the PDMS surface and thus facilitate transfer of ECM molecules from the stamp to the PDMS micropost tops. The collagen-coated PDMS stamp was then gently placed in conformal contact with the PDMS micropost array for 30 sec to complete the protein transfer process. To utilize the PDMS micropost

array for live-cell traction force measurements, we stained the PDMS micropost with 1,1′-dioleyl-3,3,3′,3′-tetramethylindocarbocyanine methanesulfonate (Δ^9-DiI; Invitrogen, Grand Island, NY). Pluronic F127 NF dissolved in PBS (0.2%, *w*/*v*; BASF, Ludwigshafen, Germany) was then adsorbed to the PDMS surface for 1 hr at room temperature to prevent protein adsorption to non-functionalized portions of the PDMS micropost array.

Cell culture and reagents

SUM149 cells were cultured in growth medium (Ham's F-12 with L-glutamine, Fisher Scientific, Hanover Park, IL) supplemented with 5% fetal bovine serum (Atlanta Biological, Flowery Branch, GA), 0.5 μg mL^{-1} Fungizone (Invitrogen), 5 μg mL^{-1} Gentamicin (Invitrogen), 5 μg mL^{-1} insulin (Sigma-Aldrich, St. Louis, MO), 1 μg mL^{-1} Hydrocortisone (Sigma-Aldrich), 50 units mL^{-1} penicillin, and 50 μg mL^{-1} streptomycin. Cells were maintained at 37ºC with 10% CO_2 and 100% humidity. Fresh 0.025% trypsin-EDTA in phosphate buffered saline (PBS) was used to re-suspend cells.

ALDEFLUOR assay

The ALDEFLUOR assay was performed using the ALDEFLOUR Kit (Stemcell Technologies, Vancouver, Canada) according to the manufacturer's instructions[40]. Briefly, ALDEFLUOR treated cells quenched with ALDH inhibitor diethylaminobenzaldehyde (DEAB) were used to set the ALDEFLUOR-positive FACS gate, which we defined as a gate containing less than 0.1% of DEAB-

treated cells. Cells treated with ALDEFLUOR alone were then sorted by FACS and used for downstream experiments. SUM149 cells above this fluorescence threshold were sorted as ALDH+ and the bottom matching percentage was sorted as ALDH-.

Invasion assay

In vitro invasion was assayed using the Biocoat Matrigel invasion chamber (BD Biosciences, San Jose, CA). Cells were plated in triplicate in the top portion of the invasion chamber in serum-free medium with 5% serum growth medium in the bottom chamber to induce invasion through the Matrigel membrane. After 24 hr of incubation, non-invading cells were removed from the top chamber with a cotton swab, and invading cells were fixed with formaldehyde and stained with 1% crystal violet. Matrigel membranes were then removed and de-stained in 10% acetic acid, and an VersaMax optical density reading (Molecular Devices, Sunnyvale, CA) of the acetic acid was taken at 590 nm. In some experiments, Matrigel membranes stained with crystal violet were imaged with invaded cells manually counted.

Cell motility assay

The Cellomics Cell Motility kit (Thermo Scientific, Waltham, MA) was used to determine cell motility. According to the manufacturer's protocol, single cell suspensions were plated in three wells of a 96-well plate that had previously been coated with blue fluorescent microbeads. After 24 hr of incubation, the

area a cell migrated was represented by the negative space in the microbead carpet that was pushed away or phagocytosed by the cell. Cells were then fixed, and the migration tracks were imaged using fluorescence microscopy with an Olympus DP26 single chip color CCD camera and an Olympus IX-51 inverted microscope (Olympus, Center Valley, PA). To quantify cell motility, the whole sample surface area was imaged and the image processing software ImageJ (National Institutes of Health, Bethesda, MD) was then used to determine the migration track area of each cell.

Cell proliferation assay

Cell proliferation rates were quantified using an MTT Cell Proliferation Assay Kit (Life technologies, Grand Island, NY). Cells were sorted by FACS and plated in triplicate onto 96-well plates. MTT staining and a subsequent optical density reading (Molecular Devices VersaMax) at 590 nm were carried out at 24 hr, 36 hr, 72 hr, and 96 hr post sorting.

Cell deformability measurements

The cell deformability was measured using a PDMS-based microfluidic deformability microcytometer developed in our lab (See Supplemental Methods for device fabrication method). The deformability microcytometer contains an array of funnel-shaped long confining microchannels that trap individual live cancer cells in each channel for single cell deformability measurement. Each channel has a length of 300 μm, a height of 30 μm, a width at the wide end

(entry) of 30 μm and a width at the narrow end of 4 μm. The channel wall is pre-coated with Pluronic-127 (Sigma) for 30 min such that friction between the cell and the channel wall can be neglected. Single cancer cells in suspension are first loaded into the channel using a pressure pump (ELVESYS, Paris, French) under low pressure (0.1-0.5 kPa). The differential pressure acting on cancer cells will gradually push the cells down the funnel, and ultimately the motion of cancer cells will stop due to the confining channel and the cells will be trapped in place. After the cell trapping, the loading pressure is gradually increased in steps (0.5 kPa for each step) to push the cell further into the channel. The trapped cells will have different deformation under different pressure. For inert microfluidic channels where cell trapping is dictated by steric interactions of cancer cells with the confining channel, the penetration length (L) of individual cancer cells into the confining channel will be purely determined by cell size and deformability. Thereby, the single cell deformability can be calculated based on model equation $Deformability = 16.9 \times d \times (A \times \Delta P)^{-1}$, where ΔP is the change of the flow pressure, d is the penetrating length under the pressure change, and A is the projective area of the cell. Cell volume V is calculated as $V = (4 \times A \times \pi^{-1})^{-1/2}$. During the assay, deformed cells were monitored with the Carl Zeiss Axio Observer Z1 microscope using a 10× objective (0.3 NA; EC Plan NEOFLUAR®; Carl Zeiss MicroImaging). Phase-contrast images were recorded. The penetration length (L) and the longitudinal and lateral diameters (D_{long} and D_{lat}) of each cell for each pressure were quantified from the recorded microscope

images using ImageJ (National Institutes of Health, Bethesda, MD) to calculate the projective area of the cell $A \approx 0.25\pi \times D_{long} \times D_{lat}$.

Quantification of cell adhesion rate

Cells were first seeded as single cells in polystyrene 48-well cell culture plates. The total loading cell number in each sample was first determined using a hemocytometer, and the desired cell concentration was then prepared by serially diluting the original cell suspension with fresh culture medium. After incubation at 10% CO_2 and 37ºC for 3 hr, samples were rinsed gently with PBS to remove floating cells. Adherent cells were then labeled with Calcein AM (Invitrogen), before imaged using fluorescence microscopy (Nikon Eclipse Ti-S, Nikon, Melville, NY). Specifically, to quantify cell adhesion rate, the whole surface area of sample was scanned on a motorized stage (ProScan III, Prior Scientific, Rockland, MA). The images were stitched into a composite and ImageJ was used to determine the number of cells attached to the culture plate surface.

Cell adhesion strength measurements

Cell adhesion strength was quantified as previously described[62]. Briefly, cells in growth medium were first injected into the microfluidic channel by pipette, and the cells were allowed to adhere to the bottom glass surface at 37ºC with 10% CO_2 and 100% humidity for 12 hr. An optimized cell loading density (1×10^6 cells mL^{-1}) was used to ensure a uniform seeding of single cells in the microfluidic channel. After cells attached to the bottom glass surface, the

microfluidic channel was connected to a syringe pump and a constant flow of PBS was injected into the channel to exert directional fluid shear stress on cells. To remove floating cells before cell adhesion strength measurements, PBS was flowed into the channel with a very low flow rate (10 µL min^{-1} for 1 min, then 30 µL min^{-1} for 1 min). The flow rate was then gradually increased from 100 µL min^{-1} to 2 mL min^{-1} step by step. At each step, the flow rate was maintained constant for 3 min to exert a constant directional fluid shear stress on cells. During the assay, detachment of cells was monitored with a Carl Zeiss Axio Observer Z1 microscope using a 10× objective (0.3 NA; EC Plan NEOFLUAR®; Carl Zeiss MicroImaging, Thornwood, NY). Phase-contract images were recorded at 15 sec intervals for a total period of 3 min. Numbers of adherent cells on the glass surface before and after each step were quantified from the recorded microscope images using ImageJ. The fluidic shear stress (τ_0) exerted on cells was calculated using the equation $\tau_0 = (6\mu Q) / (WH^2)$, where μ was the viscosity of culture medium (~10^{-3} Pa s), Q was the flow rate, and W and H were the microfluidic channel width and height, respectively. The PDMS microfluidic channel used for cell adhesion strength measurements had a channel width W of 2 mm, a channel total length L of 6 mm, and a channel height H of 80 µm. Adhesion strength of cells was defined as the fluidic shear stress at which 50% of cells initially attached on glass surfaces would detach after exposed to 3-min fluid shear.

Quantification of cell traction force

Cell traction forces were quantified as previously described[58,59]. In brief, phase-contrast images of live cells and fluorescence images of Δ^9-DiI stained PDMS microposts underlying the cells were taken at the focal plane passing through the top surface of the posts with a 40× objective on the Zeiss Observer Z1 microscope attached with the AxioCam camera. The microscope was enclosed in the Carl Zeiss XL S1 environmental chamber to maintain the experimental environment at 37°C and 10% CO_2. Images were then analyzed with a custom-developed MATLAB program to calculate the deflection δ of the post centroid from its ideal position determined by the free and undeflected posts, which was then converted to the horizontal traction force f using the expression $f = K\delta$, where K was the nominal spring constant of the PDMS micropost calculated from the *Euler-Bernoulli* beam theory as $K = 3\pi ED^4 / (64H^3)$. In this equation, E was the elastic Young's modulus of PDMS and D and H were post diameter and height, respectively.

Statistics

p-value was calculated using the student *t*-test function in Excel (Microsoft, Seattle, WA).

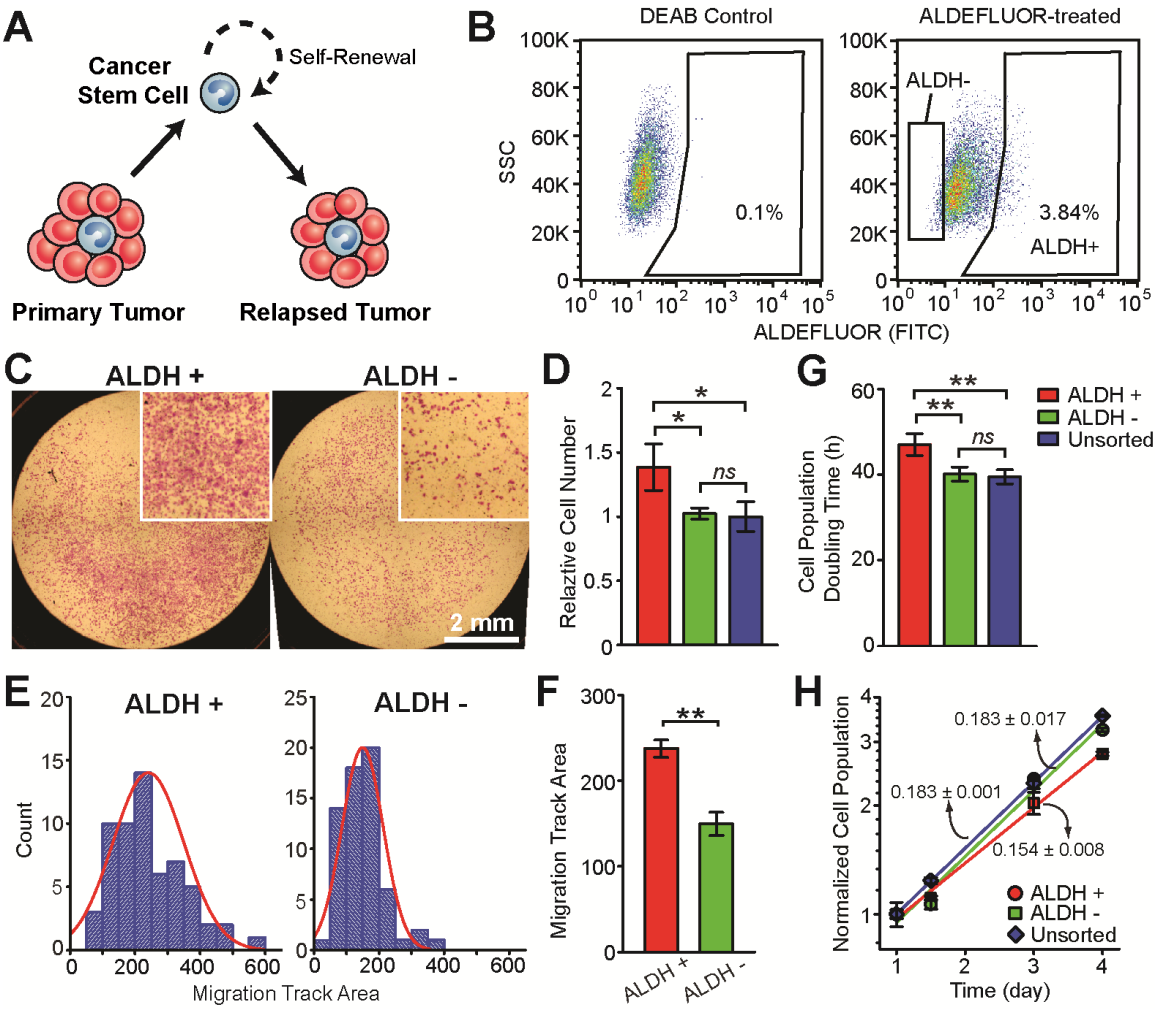

Figure 5.1. Functional phenotyping of IBC CSCs. (A) Concept of cancer stem cells. (B) Representative ALDEFLUOR analysis for SUM149 cells by FACS. Negative control samples (*left*) pre-treated with DEAB inhibitor were used to ensure identification of ALDH+ and ALDH- cells (*right*). (C&D) Representative images (C) and quantitative data (D) from *in vitro* invasion assays performed for ALDH+ and ALDH- SUM149 cells using the Biocoat Matrigel Invasion Chambers. In C, invading cells were fixed with formaldehyde before stained with 1% crystal violet. (E&F) Distribution (E) and average (F) migration track area for single ALDH+ and ALDH- SUM149 cells measured by the Cellomics Cell Motility kit. (G&H) Cell population doubling time (G) and normalized cell population as a function of culture time (H) determined using the MTT Cell Proliferation Assay Kit. For D, F, G, and H, error bars represent ± standard error of the mean (s.e.m.; n = 4). p-values were calculated using the student's t-test; *ns* ($p > 0.05$), * ($p < 0.05$), and ** ($p < 0.01$).

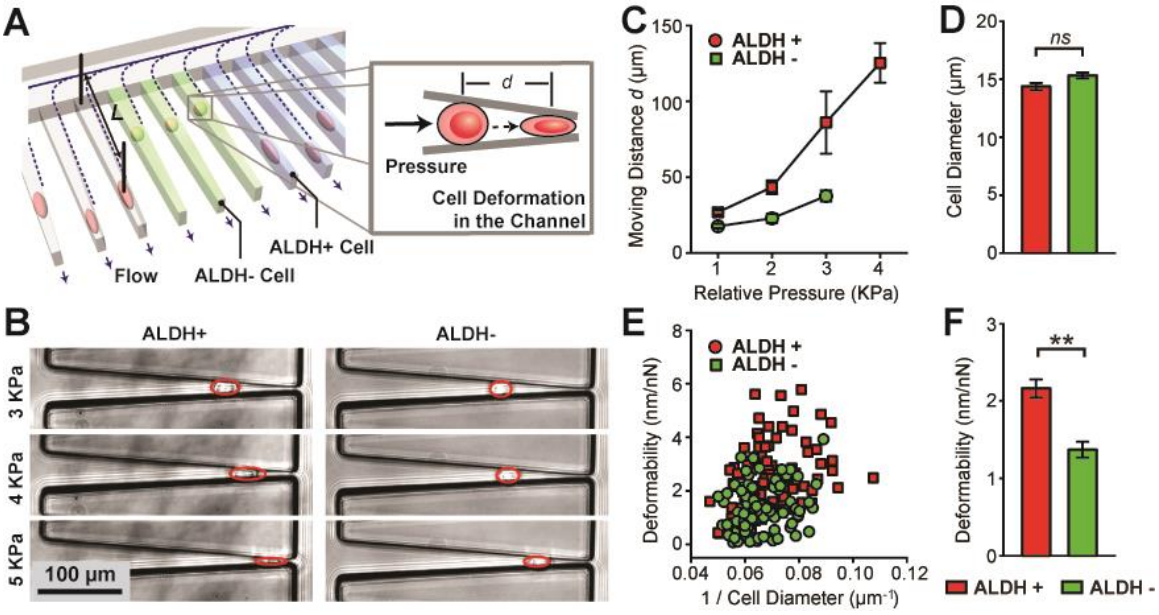

Figure 5.2. Cell deformability measurements for IBC CSCs. (A) Schematic of microfluidic deformability microcytometer for single cell deformability measurements. (B&C) Representative images (B) and quantitative data (C) showing differential penetrating distances for ALDH+ and ALDH- SUM149 cells in the deformability microcytometer under different pressures as indicated. (D) Average cell diameter of ALDH+ and ALDH- SUM149 cells. (E) Cell deformability plotted as a function of cell diameter. Each data point represents an individual cell. (F) Average cell deformability of ALDH+ and ALDH- SUM149 cells. For C, D, and F, error bars represent ± s.e.m ($n > 100$). p-values were calculated using the student t-test; *ns* ($p > 0.05$) and ** ($p < 0.01$).

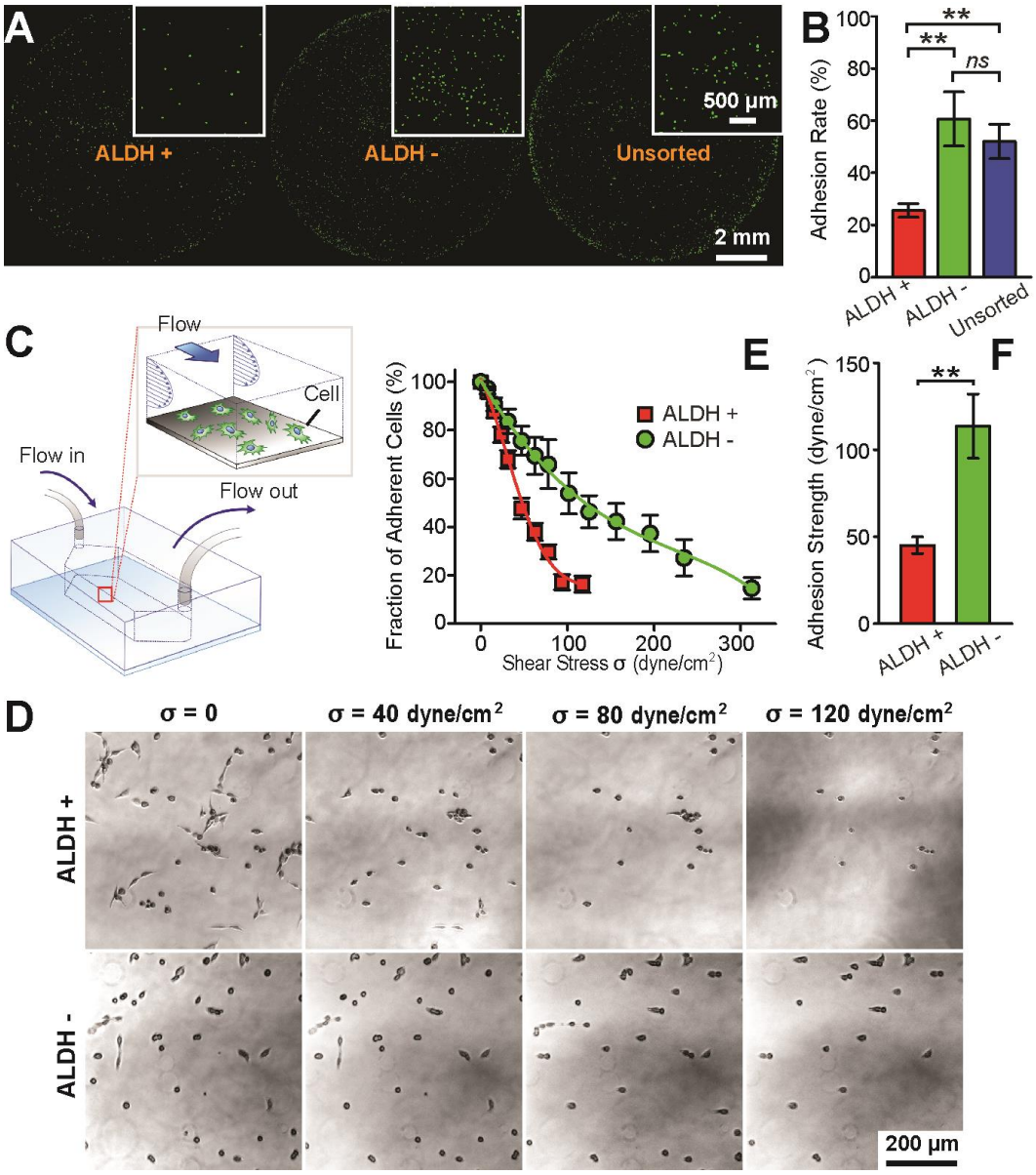

Figure 5.3. Cell adhesion strength characterization. (A&B) Representative fluorescence images (A) and quantified adhesion rate (B) of ALDH+, ALDH-, and unsorted SUM149 cells adhering to polystyrene 48-well cell culture plates 3 hr after cell seeding. Cells were stained with Calcein AM for visualization and enumeration. (C) Schematic of a microfluidic channel for quantification of cell adhesion strength. Insert shows adherent cancer cells in the channel under sustained directional fluid shear. (D) Representative brightfield images showing temporal sequences of ALDH+ and ALDH- SUM149 cells detaching from the microfluidic channel under increased fluid shear stress. (E) Fraction of ALDH+ and ALDH- SUM149 cells remaining adherent in the microfluidic channel after 3-min exposures to sustained directional fluid shear. Low densities of cancer cells were seeded into microfluidic channels and cultured for 12 hr before PBS was flowed continuously along the channel to exert fluid shear stress on cells. Solid

lines represent logistic curve fitting. (F) Adhesion strength of ALDH+ and ALDH- SUM149 cells. For B, E, and F, error bars represent ± s.e.m. (n = 4). p-values were calculated using the student t-test; *ns* ($p > 0.05$) and ** ($p < 0.01$).

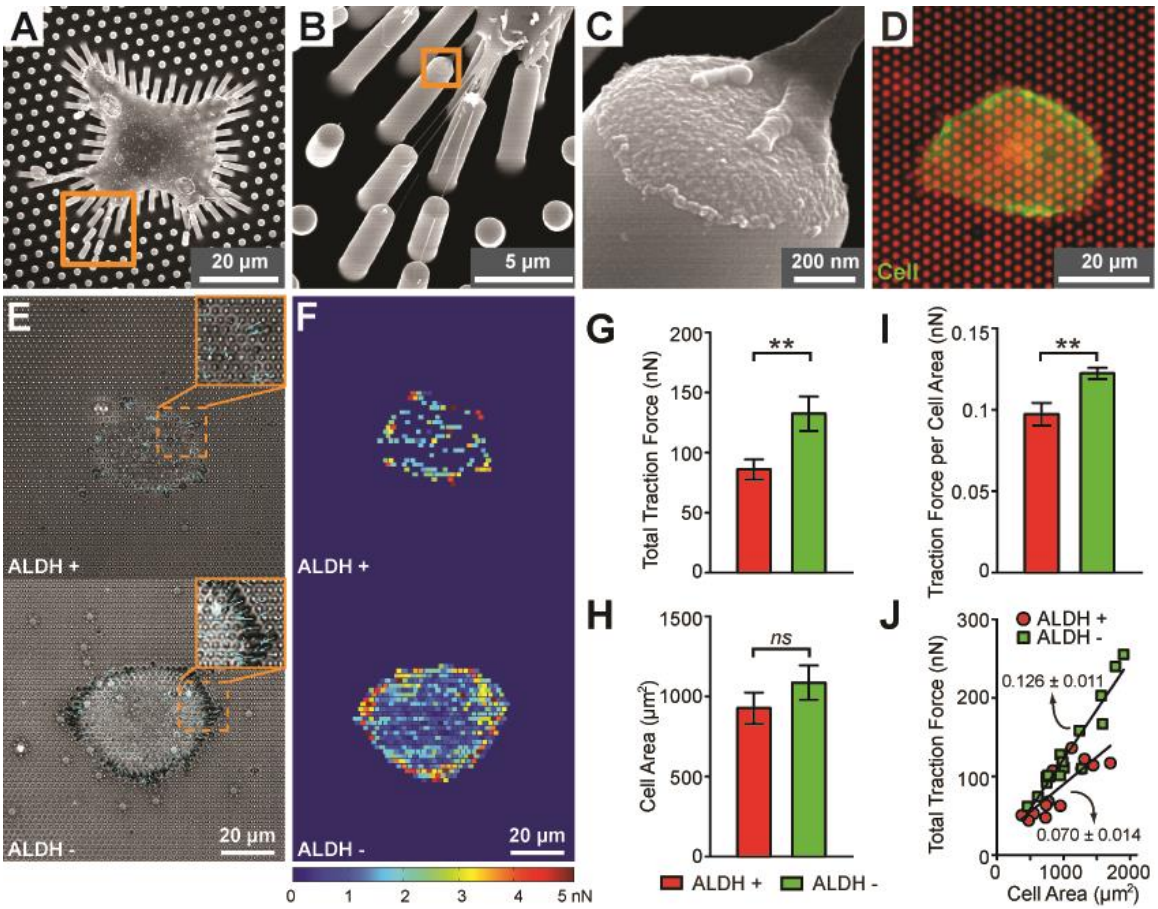

Figure 5.4. Quantification of cell traction force. (A-D) Representative SEM (A-C) and immunofluorescence (D) images showing single SUM149 cells adherent on the PDMS micropost array. In D, the single SUM149 cell was stained with fluorophore-labeled phalloidin for visualization of actin filaments (*green*). The underlying PDMS posts were labeled with DiI for visualization. (E&F) Phase (E) and colorimetric (F) maps showing subcellular traction forces exerted by single ALDH+ (*top*) and ALDH- (*bottom*) SUM 149 cells on the PDMS microposts. (G-J) Quantitative analysis of cell morphology and traction force. G-I plot total traction force per cell (G), total cell spread area (H), and traction force per cell area (I) for single ALDH+ and ALDH- cells. Data represents the means ± s.e.m ($n > 15$). *p*-values were calculated using the student *t*-test; *ns* ($p > 0.05$) and ** ($p < 0.01$). (J) Total traction force per cell as a function of cell spread area. Each data point represents an individual cell. Data trends in J are plotted using linear least square fitting (black lines), with slope values ± s.e.m indicated.

Supplemental Figures

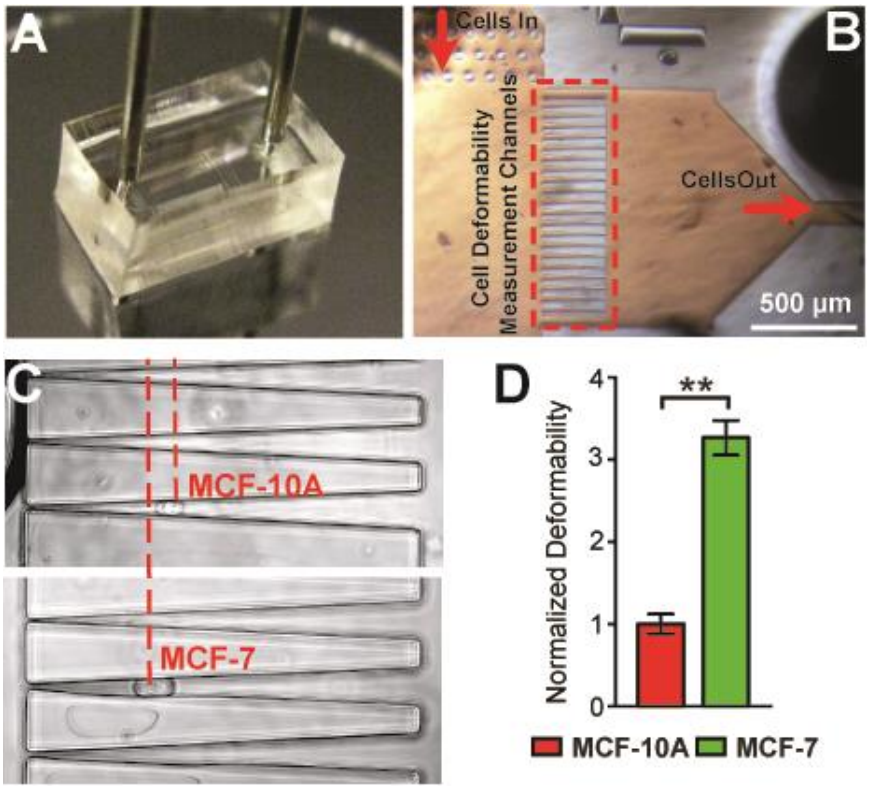

Figure 5.S1. MCF10A and MCF7 deformability measurement. (A) Photo showing the microfluidic deformability microcytometer for single cell deformability measurements. (B) Brightfield image showing structure of the deformability microcytometer. (C) Representative brightfield images showing breast cells (MCF-10A) and breast cancer cells (MCF-7) trapped in the deformability microcytometer under differential pressure across the tapped channels. (D) Normalized cell deformability of MCF-10A and MCF-7 cells. Error bars represent ± s.e.m. ($n > 20$). p-value was calculated using the student t-test. ** ($p < 0.01$).

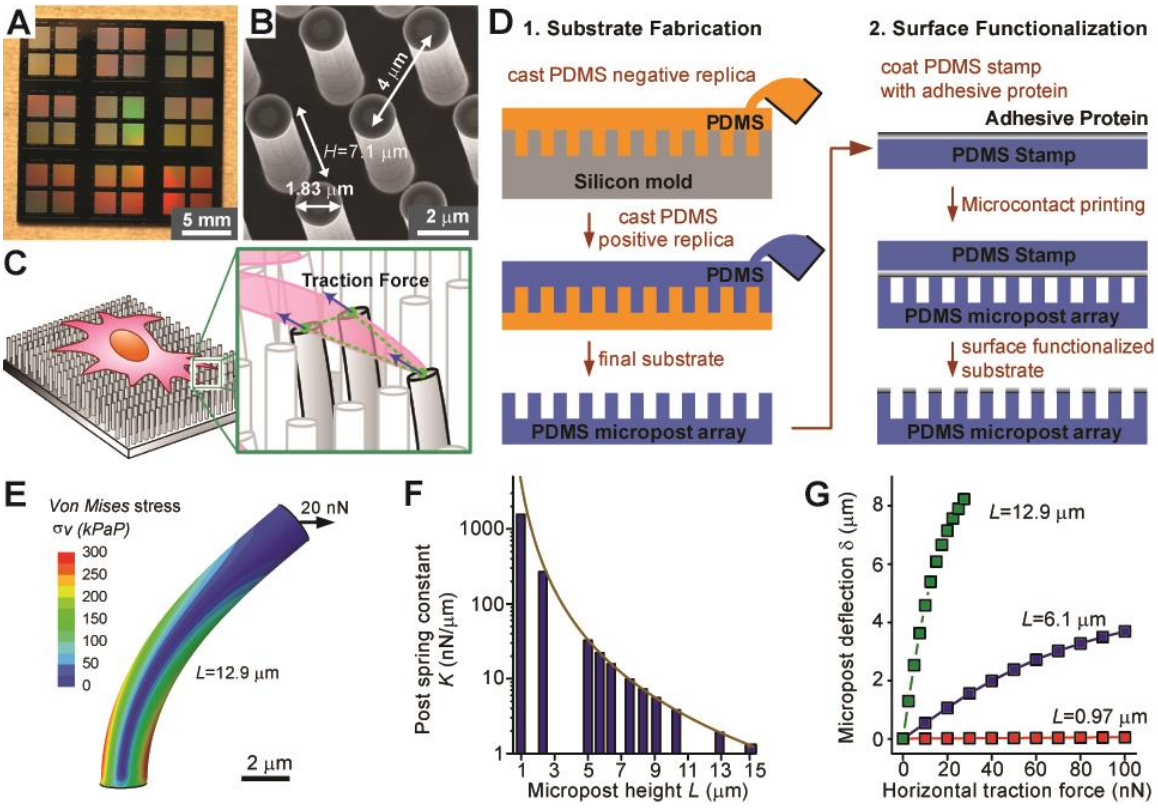

Figure 5.S2. Fabrication and characterization of PDMS micropost arrays. (A) Representative photograph of the silicon micropost array master. (B) SEM image of microfabricated hexagonally arranged silicon micropost array master with post geometrical factors indicated. (C) Schematic of using PDMS microposts as force sensors for subcellular traction force measurements. (D) Fabrication of PDMS micropost arrays involves standard photolithography and deep reactive-ion etching (DRIE) for the silicon micropost array master in a cleanroom environment, and then replica molding with PDMS to generate the final PDMS micropost array. (E) Finite-element method (FEM) analysis of micropost bending in response to a horizontal traction force F of 20 nN. Values of *Von Mises* stress, σ_v, are plotted ($\sigma_v = 0.707 \cdot [(\sigma_1 - \sigma_2)^2 + (\sigma_2 - \sigma_3)^2 + (\sigma_1 - \sigma_3)^2]^{1/2}$, where σ_1, σ_2, and σ_3 are the principle stresses in orthogonal directions). (F) Dependence of nominal spring constant K of PDMS micropost on micropost height L, as computed from FEM (bars), and from the *Euler-Bernoulli* beam theory (dark yellow curve). K is determined as $K = dF / d\delta$ ($\delta \rightarrow 0$). (G) Micropost deflection δ as a function of F for PDMS microposts of different heights, as calculated by FEM analysis (L = 0.97 μm (*red*), L = 6.1 μm (*blue*), and L = 12.9 μm (*green*)).

References

1. Reya, T., Morrison, S. J., Clarke, M. F. & Weissman, I. L. Stem cells, cancer, and cancer stem cells. *Nature* 414, 105-111, (2001).
2. Alison, M. R., Islam, S. & Wright, N. A. Stem cells in cancer: instigators and propagators? *J Cell Sci* 123, 2357-2368, (2010).
3. Jordan, C. T., Guzman, M. L. & Noble, M. Cancer stem cells. *N Engl J Med* 355, 1253-1261, (2006).
4. Al-Hajj, M., Wicha, M. S., Benito-Hernandez, A., Morrison, S. J. & Clarke, M. F. Prospective identification of tumorigenic breast cancer cells. *Proc Natl Acad Sci U S A* 100, 3983-3988, (2003).
5. Singh, S. K. *et al.* Identification of a cancer stem cell in human brain tumors. *Cancer Res* 63, 5821-5828, (2003).
6. Collins, A. T., Berry, P. A., Hyde, C., Stower, M. J. & Maitland, N. J. Prospective identification of tumorigenic prostate cancer stem cells. *Cancer Res* 65, 10946-10951, (2005).
7. Liu, H. *et al.* Cancer stem cells from human breast tumors are involved in spontaneous metastases in orthotopic mouse models. *Proc Natl Acad Sci U S A* 107, 18115-18120, (2010).
8. Hermann, P. C. *et al.* Distinct populations of cancer stem cells determine tumor growth and metastatic activity in human pancreatic cancer. *Cell Stem Cell* 1, 313-323, (2007).
9. Pang, R. *et al.* A subpopulation of CD26+ cancer stem cells with metastatic capacity in human colorectal cancer. *Cell Stem Cell* 6, 603-615, (2010).
10. Charafe-Jauffret, E. *et al.* Aldehyde dehydrogenase 1-positive cancer stem cells mediate metastasis and poor clinical outcome in inflammatory breast cancer. *Clin Cancer Res* 16, 45-55, (2010).
11. Ricci-Vitiani, L. *et al.* Identification and expansion of human colon-cancer-initiating cells. *Nature* 445, 111-115, (2007).
12. Ginestier, C. *et al.* ALDH1 is a marker of normal and malignant human mammary stem cells and a predictor of poor clinical outcome. *Cell Stem Cell* 1, 555-567, (2007).
13. Dalerba, P. *et al.* Phenotypic characterization of human colorectal cancer stem cells. *Proc Natl Acad Sci U S A* 104, 10158-10163, (2007).
14. Dylla, S. J. *et al.* Colorectal cancer stem cells are enriched in xenogeneic tumors following chemotherapy. *PLoS One* 3, e2428, (2008).
15. Teramura, T. *et al.* Isolation and characterization of side population stem cells in articular synovial tissue. *BMC Musculoskelet Disord* 9, 86, (2008).
16. Robertson, F. M. *et al.* Inflammatory breast cancer: the disease, the biology, the treatment. *CA Cancer J Clin* 60, 351-375, (2010).
17. Yamauchi, H. *et al.* Inflammatory breast cancer: what we know and what we need to learn. *Oncologist* 17, 891-899, (2012).
18. Levental, K. R. *et al.* Matrix crosslinking forces tumor progression by enhancing integrin signaling. *Cell* 139, 891-906, (2009).

19. Jinka, R., Kapoor, R., Sistla, P. G., Raj, T. A. & Pande, G. Alterations in Cell-Extracellular Matrix Interactions during Progression of Cancers. *Int J Cell Biol* 2012, 219196, (2012).
20. Cox, T. R. & Erler, J. T. Remodeling and homeostasis of the extracellular matrix: implications for fibrotic diseases and cancer. *Dis Model Mech* 4, 165-178, (2011).
21. Berthiaume, F., Moghe, P. V., Toner, M. & Yarmush, M. L. Effect of extracellular matrix topology on cell structure, function, and physiological responsiveness: hepatocytes cultured in a sandwich configuration. *FASEB J* 10, 1471-1484, (1996).
22. Paszek, M. J. *et al.* Tensional homeostasis and the malignant phenotype. *Cancer Cell* 8, 241-254, (2005).
23. Lopez, J. I., Kang, I., You, W. K., McDonald, D. M. & Weaver, V. M. In situ force mapping of mammary gland transformation. *Integr Biol (Camb)* 3, 910-921, (2011).
24. Kumar, S. & Weaver, V. M. Mechanics, malignancy, and metastasis: the force journey of a tumor cell. *Cancer Metastasis Rev* 28, 113-127, (2009).
25. Davies, P. F., Spaan, J. A. & Krams, R. Shear stress biology of the endothelium. *Ann Biomed Eng* 33, 1714-1718, (2005).
26. Ingber, D. E. Mechanobiology and diseases of mechanotransduction. *Ann Med* 35, 564-577, (2003).
27. Swaminathan, V. *et al.* Mechanical stiffness grades metastatic potential in patient tumor cells and in cancer cell lines. *Cancer Res* 71, 5075-5080, (2011).
28. Suresh, S. Biomechanics and biophysics of cancer cells. *Acta Biomater* 3, 413-438, (2007).
29. Katira, P., Bonnecaze, R. T. & Zaman, M. H. Modeling the mechanics of cancer: effect of changes in cellular and extra-cellular mechanical properties. *Front Oncol* 3, 145, (2013).
30. Lekka, M. *et al.* Cancer cell recognition--mechanical phenotype. *Micron* 43, 1259-1266, (2012).
31. Byun, S. *et al.* Characterizing deformability and surface friction of cancer cells. *Proc Natl Acad Sci U S A* 110, 7580-7585, (2013).
32. Wirtz, D., Konstantopoulos, K. & Searson, P. C. The physics of cancer: the role of physical interactions and mechanical forces in metastasis. *Nat Rev Cancer* 11, 512-522, (2011).
33. Xu, W. W. *et al.* Cell Stiffness Is a Biomarker of the Metastatic Potential of Ovarian Cancer Cells. *Plos One* 7, (2012).
34. Pelham, R. J., Jr. & Wang, Y. Cell locomotion and focal adhesions are regulated by substrate flexibility. *Proc Natl Acad Sci U S A* 94, 13661-13665, (1997).
35. Lauffenburger, D. A. & Horwitz, A. F. Cell migration: a physically integrated molecular process. *Cell* 84, 359-369, (1996).
36. Chen, W., Sun, Y. & Fu, J. Microfabricated nanotopological surfaces for study of adhesion-dependent cell mechanosensitivity. *Small* 9, 81-89, (2013).
37. Weng, S. & Fu, J. Synergistic regulation of cell function by matrix rigidity and adhesive pattern. *Biomaterials* 32, 9584-9593, (2011).

38. Mierke, C. T., Bretz, N. & Altevogt, P. Contractile forces contribute to increased glycosylphosphatidylinositol-anchored receptor CD24-facilitated cancer cell invasion. *J Biol Chem* 286, 34858-34871, (2011).
39. Kraning-Rush, C. M., Califano, J. P. & Reinhart-King, C. A. Cellular traction stresses increase with increasing metastatic potential. *PLoS One* 7, e32572, (2012).
40. Rosenthal, D. T. *et al.* RhoC impacts the metastatic potential and abundance of breast cancer stem cells. *PLoS One* 7, e40979, (2012).
41. Croker, A. K. *et al.* High aldehyde dehydrogenase and expression of cancer stem cell markers selects for breast cancer cells with enhanced malignant and metastatic ability. *J Cell Mol Med* 13, 2236-2252, (2009).
42. Jiang, F. *et al.* Aldehyde Dehydrogenase 1 Is a Tumor Stem Cell-Associated Marker in Lung Cancer. *Molecular Cancer Research* 7, 330-338, (2009).
43. Ucar, D. *et al.* Aldehyde dehydrogenase activity as a functional marker for lung cancer. *Chemico-Biological Interactions* 178, 48-55, (2009).
44. Ma, S. *et al.* Aldehyde dehydrogenase discriminates the CD133 liver cancer stem cell populations. *Molecular Cancer Research* 6, 1146-1153, (2008).
45. Carpentino, J. E. *et al.* Aldehyde Dehydrogenase-Expressing Colon Stem Cells Contribute to Tumorigenesis in the Transition from Colitis to Cancer. *Cancer Research* 69, 8208-8215, (2009).
46. Rasheed, Z. A. *et al.* Prognostic significance of tumorigenic cells with mesenchymal features in pancreatic adenocarcinoma. *J Natl Cancer Inst* 102, 340-351, (2010).
47. Silva, I. A. *et al.* Aldehyde Dehydrogenase in Combination with CD133 Defines Angiogenic Ovarian Cancer Stem Cells That Portend Poor Patient Survival. *Cancer Research* 71, 3991-4001, (2011).
48. Chen, Y. C. *et al.* Aldehyde dehydrogenase 1 is a putative marker for cancer stem cells in head and neck squamous cancer. *Biochemical and Biophysical Research Communications* 385, 307-313, (2009).
49. van den Hoogen, C. *et al.* High aldehyde dehydrogenase activity identifies tumor-initiating and metastasis-initiating cells in human prostate cancer. *Cancer Res* 70, 5163-5173, (2010).
50. Magni, M. *et al.* Induction of cyclophosphamide-resistance by aldehyde-dehydrogenase gene transfer. *Blood* 87, 1097-1103, (1996).
51. Luo, Y. *et al.* ALDH1A isozymes are markers of human melanoma stem cells and potential therapeutic targets. *Stem Cells* 30, 2100-2113, (2012).
52. Vasiliou, V., Pappa, A. & Estey, T. Role of human aldehyde dehydrogenases in endobiotic and xenobiotic metabolism. *Drug Metab Rev* 36, 279-299, (2004).
53. Charafe-Jauffret, E., Ginestier, C. & Birnbaum, D. Breast cancer stem cells: tools and models to rely on. *BMC Cancer* 9, 202, (2009).
54. Marcato, P. *et al.* Aldehyde Dehydrogenase Activity of Breast Cancer Stem Cells is Primarily Due to Isoform ALDH1A3 and Its Expression is Predictive of Metastasis. *Stem Cells* 29, 32-45, (2011).

55. Tanei, T. *et al.* Association of breast cancer stem cells identified by aldehyde dehydrogenase 1 expression with resistance to sequential Paclitaxel and epirubicin-based chemotherapy for breast cancers. *Clin Cancer Res* 15, 4234-4241, (2009).
56. Gupta, P. B. *et al.* Stochastic state transitions give rise to phenotypic equilibrium in populations of cancer cells. *Cell* 146, 633-644, (2011).
57. Chaffer, C. L. *et al.* Normal and neoplastic nonstem cells can spontaneously convert to a stem-like state. *Proceedings of the National Academy of Sciences of the United States of America* 108, 7950-7955, (2011).
58. Fu, J. *et al.* Mechanical regulation of cell function with geometrically modulated elastomeric substrates. *Nat Methods* 7, 733-736, (2010).
59. Yang, M. T., Fu, J., Wang, Y. K., Desai, R. A. & Chen, C. S. Assaying stem cell mechanobiology on microfabricated elastomeric substrates with geometrically modulated rigidity. *Nat Protoc* 6, 187-213, (2011).
60. Fan, Z. *et al.* Acoustic tweezing cytometry for live-cell subcellular modulation of intracellular cytoskeleton contractility. *Sci Rep* 3, 2176, (2013).
61. Brodland, G. W. & Veldhuis, J. H. The mechanics of metastasis: insights from a computational model. *PLoS One* 7, e44281, (2012).
62. Chen, W. Q. *et al.* Nanoroughened Surfaces for Efficient Capture of Circulating Tumor Cells without Using Capture Antibodies. *Acs Nano* 7, 566-575, (2013).

Chapter 6

Conclusions and Future Directions

The metastatic series of sieves represents the complement of biological challenges a tumor cell must overcome in order to metastasize. Not every cell in a cancer is intrinsically able to navigate the metastatic process. Less than 0.01% of a cancer's heterogeneous population can successfully initiate a distant site of tumor growth, and understanding what gives these rare cells this capability – be they genes, extrinsic cytokines, or a biomechanical phenotype – will ultimately provide insight into how to target the process responsible for more than 90% of cancer deaths. In this work I advanced our present knowledge of the metastatic process by marrying microfluidic techniques with four fundament questions of the metastatic series of sieves.

What are genetic molecular drivers that allow certain cancer cells to metastasize?

In Chapter 2, we showed that the highly chemotactic subpopulation of MDA-MB-231 breast cancer cells selected through the migration assay maintained this migratory phenotype after harvesting and reintroduction to the migration assay. Furthermore, the chemotactic cells expressed significantly greater amounts of the MAPK isoform p38γ and the RhoC GTPase, both critical modulators of

mesenchymal motility. Our lymphatic capillary mimetic device can be used to directly visualize one of the critical steps of the metastatic series of sieves in order to reveal further insights into what molecular underpinnings allow certain cancer cells within a heterogeneous tumor to intravasate into capillaries and subsequently metastasize. Thus, the present platform provides the capability to correlate the migration phenotype of the highly chemotactic cells with a molecular signature of gene expression within this subpopulation.

The most logical next step to elevate the significance of this work would be to isolate patient tumor cells from a biopsy and screen them for chemotactic subpopulations. Our device has proven capable with the loading of just a few hundred cells and technologies exist that could run a panel of genetic assays on the limited output of only tens of chemotactic cells. The limitation of the present study was its reliance on derived cell lines. If the device can be proven to sort patient samples, then it would be useful as a tool for discovery of new molecular drivers of metastasis in addition to being a diagnostic tool driving treatment decisions. Different anti-metastatic therapies will be developed to target different mechanisms and oncologists will need a function-based assay to determine which is active in a given patient to rationalize precision therapy.

What are environmental cues to tumor cells that trigger metastasis?

In Chapter 3, we demonstrated that inflammatory breast cancer – a rare and very aggressive subset of breast cancer nearly metastatic from its inception – is

hyper-responsive to macrophage-conditioned media, which stimulates an extreme migratory phenotype. We found that interleukins -6, -8, and -10 within the macrophage media are sufficient to induce this effect individually and that a Ras-homology GTPase is necessary for the extreme migration. Rather than acting as the chemoattractants themselves, it appears that the macrophage-conditioned media serves to “prime” the IBC cells to have a magnified migration response by increasing the expression of RhoC.

It remains an open question and studies are ongoing in our lab as to whether the specific cytokines identified *in vitro* will have a metastasis-promoting effect in mouse models. There are no transgenic mouse models of inflammatory breast cancer and so we are left with studying the process in immunocompromised animals. Preliminarily, mice implanted with macrophages only, inflammatory breast cancer cells only, or both together all grew masses therefore confounding any interpretation of the source of human DNA in the mouse lungs as determined by PCR. This results from the limitation of using cell line derived macrophages rather than macrophages isolated and stimulated from healthy donors or, better still, macrophages isolated from the tumor stroma of IBC patients. Further experiments will make use of specifically tagged cancer cells and patient-derived macrophages. Another limitation of this work was the relatively small magnitude of the enhanced migration effect seen with single-agent cytokine stimulation. Despite this, for patients with metastatic inflammatory breast cancer on the last lines of treatment options, opening a clinical trial for anti-interleukin-6 therapies

already in use against rheumatoid arthritis might be an option to see if inhibiting the microenvironmental cues might alter the course of this aggressive breast cancer.

Can we harness physical property differences to isolate cancer cells in patients once they do metastasize?

In Chapter 4, we developed a microfluidic CTC capture chip that incorporated a nanoroughened glass substrate for capturing CTCs from blood samples. Our CTC capture chip utilized the differential adhesion preference of cancer cells to nanoroughened etched glass surfaces as compared to normal blood cells and thus did not depend on the physical size or surface protein expression of CTCs. Most significantly, in a syngeneic mouse model of lung cancer using cell lines with differential metastasis capability, CTCs were captured from all mice with detectable primary tumors independent of the cell lines' metastatic ability.

Thus, a population of CTCs incapable of forming metastases was detected by the microfluidic CTC capture chip, supporting that cellular signals and biological processes that allow for individual cell invasion and intravasation are not identical to those governing the seeding of fruitful metastases. It remains to be proven if these same properties will reliably detect patient CTCs and not just those derived from cell lines and xenografts. However, if they can be detected, future important research will be to understand the differences in the nature of non-metastasis forming CTCs from those that form metastasis to determine their true

significance in patient prognosis and in the clinical management of cancer. This is now possible as our microfluidic CTC capture chip allows for both populations' study with its unbiased capture method based on the selective adhesion of cancer cells.

Is there an overall mechanical phenotype of the most aggressive tumor cells that are successful in metastasis?

In Chapter 5, we comprehensively profiled the functional and, more importantly, biophysical characteristics of IBC CSCs at the single-cell level using multiple microengineered tools and traditional *in vitro* studies to delineate the live cell phenotypic characteristics of the model of the most metastatic breast cancer subtype. This biomechanical characterization of ALDH+ IBC CSCs revealed distinct physical properties that might mechanistically explain the functional differences seen between the IBC CSC and non-CSC population. These biophysical properties included a greater cell deformability, weaker adhesion strength, and less cellular traction force. This unique profile of mechanical characteristics associated with ALDH+ IBC CSCs could help explain how CSCs are better adapted than non-CSCs to successfully navigate through their dynamic microenvironment in the metastatic series of sieves. Our multiparametric cellular phenotyping of functional and biophysical characteristics of IBC CSCs yields a new understanding of IBC's metastatic properties and how they might develop and be targeted for therapeutic interventions. While the present work is limited to an *in vitro* model and will need validation, future work to

alter these cells' mechanical characteristics and profile their metastatic ability could pave the way for an entirely new class of anti-cancer and anti-metastatic therapies targeted to modify the physical parameters of cells.

Appendix

Chronic Mastitis in Egypt and Morocco: Differentiating Between Idiopathic Granulomatous Mastitis and IgG4-related Disease

The work presented in the Appendix has been accepted for publication in The Breast Journal.

Appendix Summary

Idiopathic granulomatous mastitis (IGM) is a benign, frequently severe chronic inflammatory lesion of the breast. Its etiology remains unknown and reported cases vary in their presentation and histologic findings with an optimal treatment algorithm yet to be described owing mainly to the disease's heterogeneity. IgG4-related disease (IgG4-RD) is a newly recognized systemic fibroinflammatory condition characterized by a dense lymphoplasmacytic infiltrate with many IgG4-positive plasma cells, storiform fibrosis, and obliterative phlebitis. Immunosuppressive therapy is considered to be an effective first-line therapy for IgG4-RD. We sought to clarify and classify chronic mastitis according to the histologic findings of IgG4-RD mastitis with respect to IGM and to develop a robust diagnostic framework to help select patients for optimal treatment strategies. Using the largest collection to date (43 cases from Egypt and Morocco), we show that despite sharing many features, IGM and IgG4-RD

mastitis are separate diseases. To diagnostically separate the diseases, we created a classification schema – termed the Michigan Classification – based upon our large series of cases, the consensus statement on IgG4-RD, and the histologic description of IGM in the literature. Using our classification, we discerned 17 cases of IgG4-RD and 8 cases of IGM among the 43 chronic mastitis cases, with 18 indeterminate cases. Thus our Michigan Classification can form the basis of rational stratification of chronic mastitis patients between these two clinically and histopathologically heterogeneous diseases.

Introduction

Idiopathic granulomatous mastitis (IGM) is a non-neoplastic, chronic inflammatory lesion of the breast that mimics carcinoma both clinically and radiologically [1-5]. IGM affects mostly parous women of child-bearing age, but has been reported in the age range of 11-80 years [2,6]. Patients most commonly present with an enlarging, firm, and tender breast lump with erythema and occasionally nipple retraction and/or axillary lymphadenopathy [3,4,7,8]. With these concerning clinical characteristics and non-specific imaging findings frequently resembling inflammatory breast cancer, the diagnosis is often made by core needle biopsy [1-4,6,7,9]. Histologically, IGM appears as non-caseating granulomas, frequently centered on the breast lobules, with epithelioid histiocytes and multinucleated giant cells and varying numbers of plasma cells, lymphocytes, neutrophils, and eosinophils [8,10]. IGM remains a diagnosis of exclusion, however, as there are multiple processes that may cause granulomatous

inflammation of the breast [8]. An optimal treatment algorithm remains elusive owing mainly to the lack of a complete etiological classification. Therapeutic choices comprise observation, immunosuppressive therapy, wide local excision, mastectomy, or combined therapies; however, these strategies have varied success and recurrences are common [2,6,7,9,11].

IgG4-related disease (IgG4-RD) is a newly recognized fibroinflammatory condition affecting various organs [12-14]. It is characterized by a dense lymphoplasmacytic infiltrate with many IgG4-positive plasma cells, storiform fibrosis, obliterative phlebitis, and often elevated serum IgG4 concentration [12-17]. Reportedly uncommon are the presence of well-formed granulomas and a marked neutrophilic infiltration [12,13,18]. IgG4-RD is now known to at least partly explain a broad range of medical conditions previously believed to be unique diseases [12,15,17]. While no randomized clinical trials have been conducted, glucocorticoid treatment is the standard first-line therapy [12,15].

In contrast to the abundance of cases in other organs, there have been up to now only 9 reported cases of IgG4-RD occurring in the breast [19-23]. Among these cases of IgG4-RD mastitis, there is a great heterogeneity in the clinical and histopathological findings and apparent overlap with IGM characteristics. Consistent with this observation, IgG4-RD is known to have variations in histologic appearance depending on the specific organ involved [12-14,17,18]. Furthermore, IGM itself is known to have a heterogeneous appearance and lacks

a consensus on an optimal treatment protocol [2,3,6,9,11]. Thus, we sought to clarify and classify chronic mastitis according to the histologic findings of IgG4-RD mastitis with respect to IGM from a large retrospective collection of cases from Egypt and Morocco, in order to better characterize and distinguish the subset of chronic mastitis patients with IgG4-RD who would benefit from immunosuppressive therapy.

Results

Diagnosis of IgG4-Related Disease and Idiopathic Granulomatous Mastitis

Table 1 summarizes the histopathologic findings and IgG4 and IgG quantification of the cases. In total, 17 cases of IgG4-RD mastitis were identified along with 8 cases of IGM and 18 indeterminate chronic mastitis cases. In our schema, which we term the Michigan Classification, to be classified as most likely IgG4-RD mastitis, a sample must have met at least 4 of 5 positive criteria and 2 of 3 negative criteria. The positive criteria were adapted from and are consistent with the IgG4-RD consensus statement and the negative criteria were newly developed by our group to propose a classification schema that would encompass the heterogeneity of the findings in our large sample while in agreement with the consensus statement and the general histologic characteristics of IGM described previously [10,13]. The positive criteria were: dense lymphoplasmacytic infiltrate, storiform fibrosis, obliterative phlebitis, >10 IgG4+ cells/hpf, and >40% IgG4:IgG ratio. The negative criteria were: epithelioid histiocytes, well-formed granulomas, and giant cells. Consistent with the

histological description of IGM [10], cases were classified as IGM if they demonstrated: epithelioid histiocytes, vague or well-formed granulomas, and giant cells. The diagnostic criteria for IGM and our newly developed criteria for IgG4-RD mastitis are outlined in Table 2. The IGM category was assigned irrespective of the number of IgG4-positive plasma cells or IgG4:IgG ratio or the presence of other histologic characteristics of IgG4-RD. Although a prominent neutrophilic infiltration has generally been reported as relatively rare with IgG4-RD, this is known to vary by organ [12,13]. Neutrophils were not therefore considered in our diagnostic criteria for breast IgG4-RD because they did not appear to be a distinguishing characteristic between IgG4-RD mastitis and IGM in our large sample.

Pathologic Findings

Both IgG4-RD mastitis (Figure 1A) and IGM (Figure 1B) cases overwhelmingly had a dense lymphoplasmacytic infiltrate and only the indeterminate cases tended to have a mixed infiltrate. The presence of storiform fibrosis, however, was a more specific differentiator between the two diseases as it was present in 17 of 17 IgG4-RD mastitis cases (Figure 1C) and absent in the 5 of 8 IGM cases (Figure 1D) ($P<0.001$). Obliterative phlebitis was not a differentiating criterion and was seen in 11 of 17 IgG4-RD cases (Figure 1E) and present in 3 of 8 IGM cases ($P=0.39$). The presence of epithelioid histiocytes was the most common IGM feature overlapping with the IgG4-RD cases, being present in 5 of the 17 IgG4-RD cases. There were no well-formed granulomas in the IgG4-RD mastitis

cases and giant cells were present in 3 cases. Representative images of IGM epithelioid histiocytes, granulomas, and giant cells can be seen in Figures 2A-D.

IgG4 Quantification

The average number of IgG4 cells per high power field and the IgG4:IgG ratio for each of the IgG4-RD mastitis, IGM, and indeterminate cases are plotted in Figures 3A-B. There were statistically significantly more IgG4+/hpf in the IgG4-RD cases than in the indeterminate cases ($P<0.01$), but not compared to the IGM cases ($P=0.061$). However, the average ratio of the IgG4-RD mastitis cases (49%) was significantly higher than the average ratio for both the IGM cases (26%, $P<0.001$) and indeterminate cases (20%, $P<0.001$). As has been reported previously [13,14,16,17], an IgG4:IgG ratio of >40% proved quite specific as a diagnostic criterion with 14 of 17 IgG4-RD cases meeting the threshold, in contrast to only 2 of 8 IGM cases ($P<0.01$). Representative images of IgG4 and IgG dual-staining of IgG4-RD mastitis and IGM cases are shown in Figures 4 A-B and C-D, respectively.

Discussion

Our report describes the largest chronic mastitis series to date comprising of 43 cases from Egypt and Morocco and seeks to develop a robust framework to begin to differentiate and to understand the possible pathogenetic basis of this complex set of diseases. In light of previous work in this field, we first sought to understand IGM in the context of the more recently recognized IgG4-RD. Of

these 43 chronic mastitis cases, 17 (40%) were determined to be IgG4-RD mastitis, 8 were IGM, and 18 were indeterminate cases of mastitis. Ogura *et al* [20] first posited that IGM could be separated into IgG4-related and non-IgG4-related cases, but our analysis supports the conclusion that the two appear more likely to be distinct disease entities. While the two cases of IGM Ogura *et al* [20] reported on did have significant numbers of IgG4 positive cells, an IgG4:IgG ratio was not calculated, which has proven to be the most specific indicator for IgG4-RD in our study and others [13]. In our present study, when classified solely based upon the presence of epithelioid histiocytes, giant cells, and vague or well-formed granulomas, it is apparent that some of the IGM cases (see cases 18 and 22 Table 1) do share many features typical for IgG4-RD mastitis. Therefore, the distinction between the two diseases likely only became apparent with our larger sample size.

Furthermore, we were able to ascertain which histologic features are the most specific for differentiating between IgG4-RD mastitis and IGM by classifying IGM cases without regard to their IgG4-RD features. Therefore, by our schema, it was determined the most common and least specific IgG4-RD features seen in IGM were a dense lymphoplasmacytic infiltrate (7/8 cases) and large numbers of IgG4-positive plasma cells (5/8 cases). In contrast, the dual criteria of storiform fibrosis coupled with an IgG4:IgG ratio >40% is reasonably specific for IgG4-RD mastitis with 14/17 cases meeting both criteria. Additionally, since we did not specify which of the positive or negative criteria must be met to diagnose IgG4-

RD mastitis, we can determine the most frequently absent IgG4-RD feature and most frequently present IGM feature. This is helpful in further clarifying the distinction between borderline cases. Obliterative phlebitis was the feature most often absent from IgG4-RD mastitis cases and epithelioid histiocytes the most common IGM characteristic seen in IgG4-RD mastitis. Therefore, the presence of giant cells or well-formed granulomas is quite specific within the breast for IGM when differentiating between it and IgG4-RD mastitis. Conversely, the absence of obliterative phlebitis should not preclude a diagnosis of IgG4-RD mastitis.

The average number of IgG4-positive plasma cells per high power field is lower for some of our reported IgG4-RD mastitis cases (12-29 cells/hpf for 7 of the 17 cases) than for cases reported in the literature [18,19]. We point to two likely explanations for this apparent deviation. First, our samples were biopsy samples known to have fewer IgG4+/hpf than surgical specimens [18] and, in fact, the consensus criteria lowers the requirement from 30 to 10 IgG4+/hpf for biopsy samples [13]. All of our IgG4-RD mastitis cases met this lower threshold. Second, we had an observable area of 0.139 mm^2 compared to 0.196 mm^2 reported by Cheuk *et al* [19] and mentioned by the consensus statement [13]. While this area difference would not affect the IgG4:IgG ratio, it would be expected to affect the absolute number of positive cells. If the absolute counts for our IgG4-RD cases were multiplied by a 1.2x area scaling factor, then 13 of the 17 cases would have greater than 30 IgG4+ cells/hpf – even as biopsy and not surgical specimens.

Ultimately though, it is the IgG4:IgG ratio that is a better and more specific diagnostic criterion for IgG4-RD.

In summary, we report on the largest chronic mastitis series to date comprising of 43 cases from Egypt and Morcco, of which 17 (40%) were IgG4-RD of the breast, 8 were IGM, and 18 indeterminate cases of mastitis. This also represents the largest collection of IgG4-RD of the breast – nearly doubling the number of previously reported cases [19-23]. Among our samples, storiform fibrosis, an IgG4:IgG ratio >40%, and the absence of well-formed granulomas and giant cells is a highly specific 4-variable panel for IgG4-RD mastitis. IGM on the other hand is characterized by many giant cells and epithelioid histiocytes and one should not be misled by the occasional high number of IgG4-positive plasma cells or increased IgG4:IgG ratio. Thus our Michigan Classification requiring the presence of 4 of 5 positive criteria and absence of 2 of 3 negative criteria suggests a rational stratification basis between these two clinically and histopathologically heterogeneous diseases.

Materials and Methods

Study Population

We performed a retrospective hospital-based study and identified 43 cases of chronic mastitis of unknown etiology from 5 hospitals in Morocco (L'hopital Ibn Rochd, Hassan II University and L'Hopital Ibn Toufail) and Egypt (Cairo University Medical School, Mansoura University Oncology Center, and the Tanta

Cancer Center) [5]. The average age of the patients was 36.9 years (SD 9.1, range 17-60). Cases were defined as any female patient with histopathological diagnosis of chronic mastitis of unknown etiology based upon an excisional biopsy and seen at the study hospitals from 2008-2011. All patients initially presented with a breast mass and routine clinical workup (e.g. acid-fast staining and appropriate cultures) was performed to rule out other common mass-forming and granulomatous-forming lesions of infectious and other etiologies. The only exclusion criterion was previous diagnosis of malignancy [5]. Further epidemiological and clinical characteristics (including lactation history and parity) of the study population are reported in detail in Oltean *et al* [5]. The study underwent ethics board review and approval at all the institutions named above and at the University of Michigan.

Pathology Review and Dual Staining Protocol

Blinded to the IgG4 quantification, two authors (C.K. and S.G.A.) analyzed one haematoxylin and eosin (H&E) slide from each case sectioned from the same paraffin-embedded tissue cassette as were the immunostained slides. The parameters assessed were: a dense lymphoplasmacytic infiltrate, storiform fibrosis, obliterative phlebitis, epithelioid histiocytes, granulomas, giant cells, and neutrophils. Immunohistochemistry staining was performed as described previously [24]. Specific to this study, slides were incubated for 1.5 hours at room temperature with an antibody cocktail containing rabbit anti-IgG (Cell Marque, Cat# 269A-15) diluted 1:5400 and mouse anti-IgG4 (Cell Marque, Cat# 367M-15)

diluted 1:900 and detected with Mach 2 Double Stain 2, (Biocare Medical) for 10 minutes at room temperature.

Imaging and counting protocol

H&E images were captured using an Olympus BX41TF microscope with an Olympus UD03 CCD at 100x and 400x magnification. After immunostaining, digital images were captured by an Olympus DP26 CCD using an Olympus IX-51 microscope. The 200x immunostain digital images' field of view was 0.139 mm^2 in area. This was 20% smaller in area than the hpf reported by Cheuk *et al* [19]. The three areas of the most intense inflammation were imaged and then IgG4 and IgG positive cells were quantified in each of the three images using ImageJ and averaged. The IgG4:IgG ratio was calculated as: IgG4/(IgG4+IgG).

Statistics

OriginPro 9.1 was used to calculate statistical differences using either Fisher's exact test or a t-test of unequal variances.

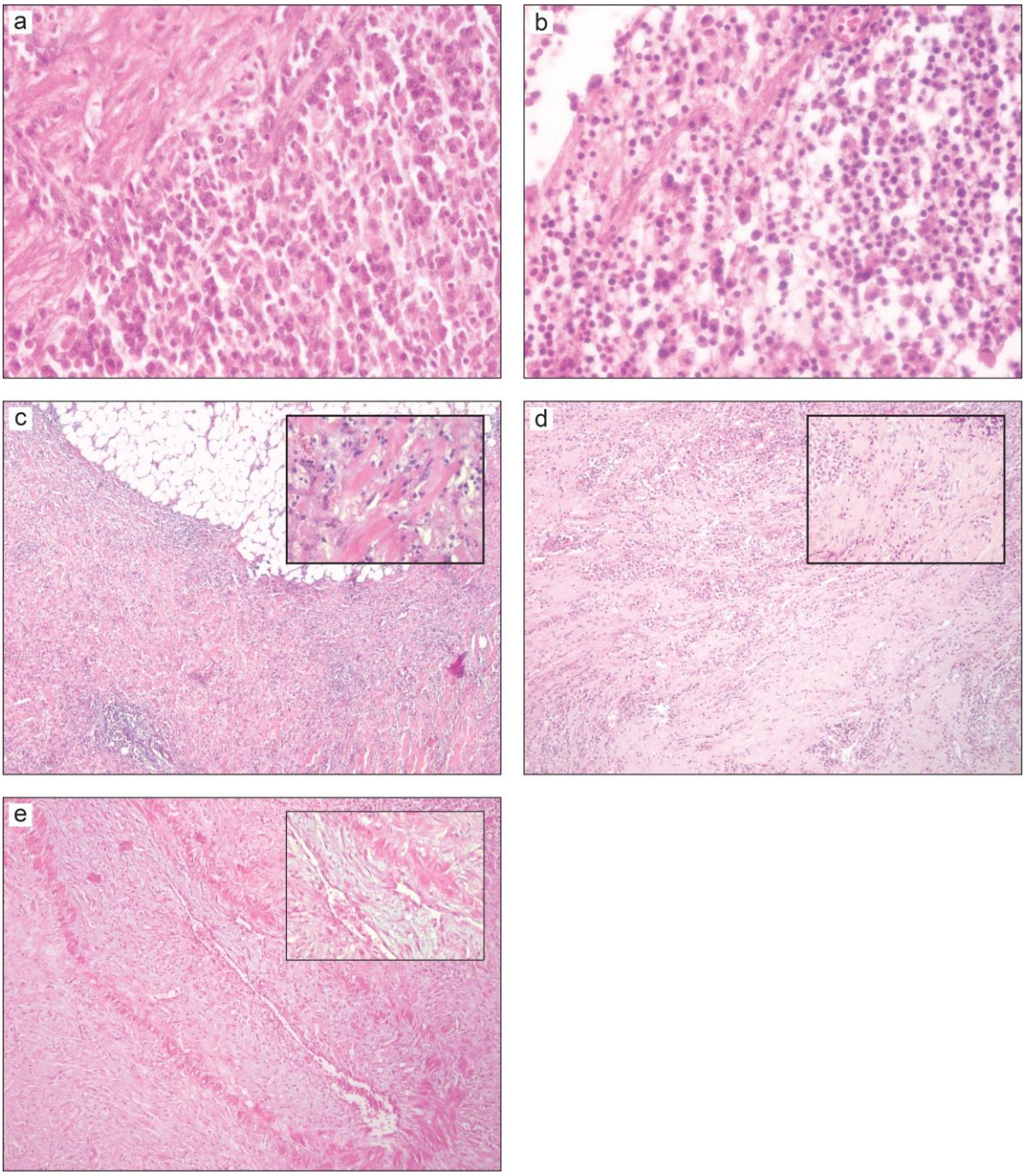

Figure A.1 – IgG4-RD and IGM comparison
Representative H&E images of IgG4-RD (**a**, **c**, and **e**) and IGM (**b** and **d**). A dense lymphoplasmacytic infiltrate is seen in IgG4-RD mastitis (**a**) and IGM (**b**), x400. (**c**) Storiform fibrosis in IgG4-RD mastitis, x100, x400. (**d**) Non-storiform fibrosis in IGM, x100, x400. (**e**) Obliterative phlebitis in IgG4-RD mastitis, x100, x400.

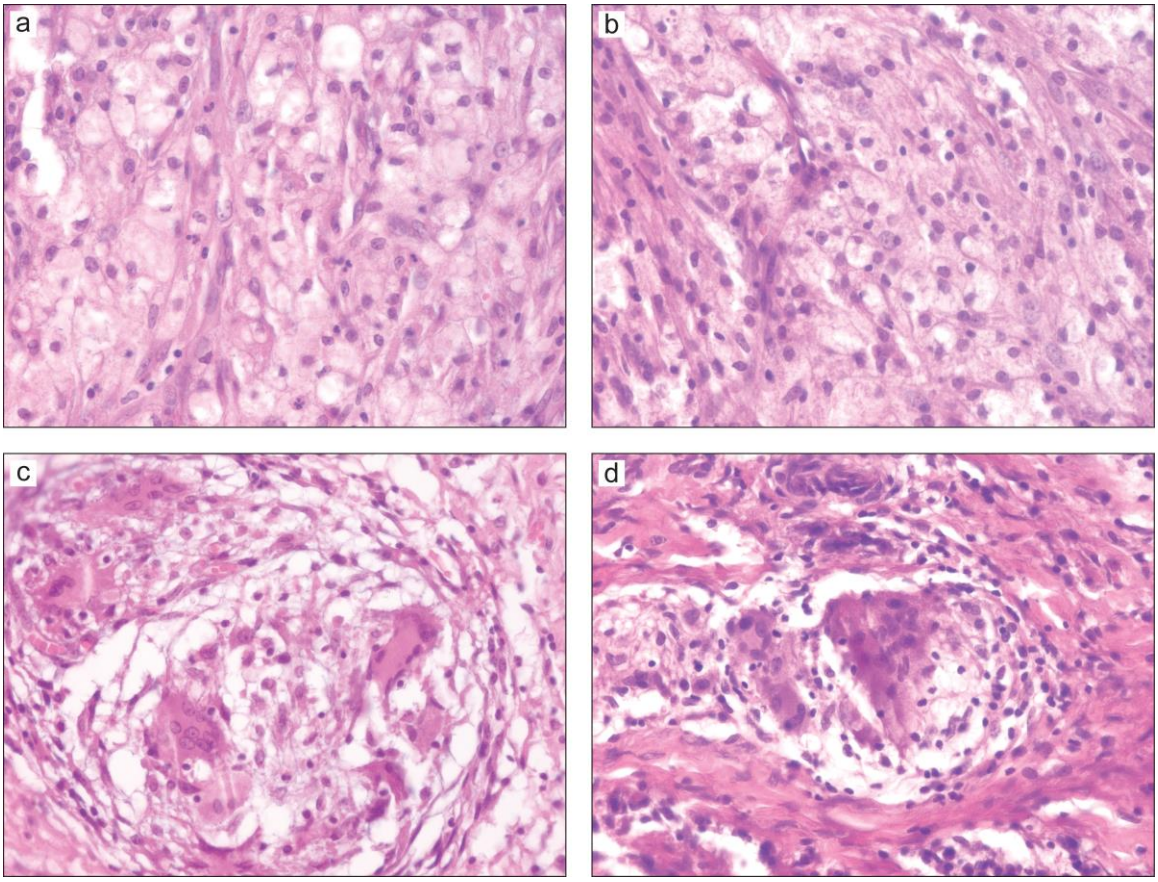

Figure A.2 – IGM histopathology
(**a** and **b**) Epithelioid histiocytes, x400. (**c** and **d**) Well-formed granulomas and giant cells, x400.

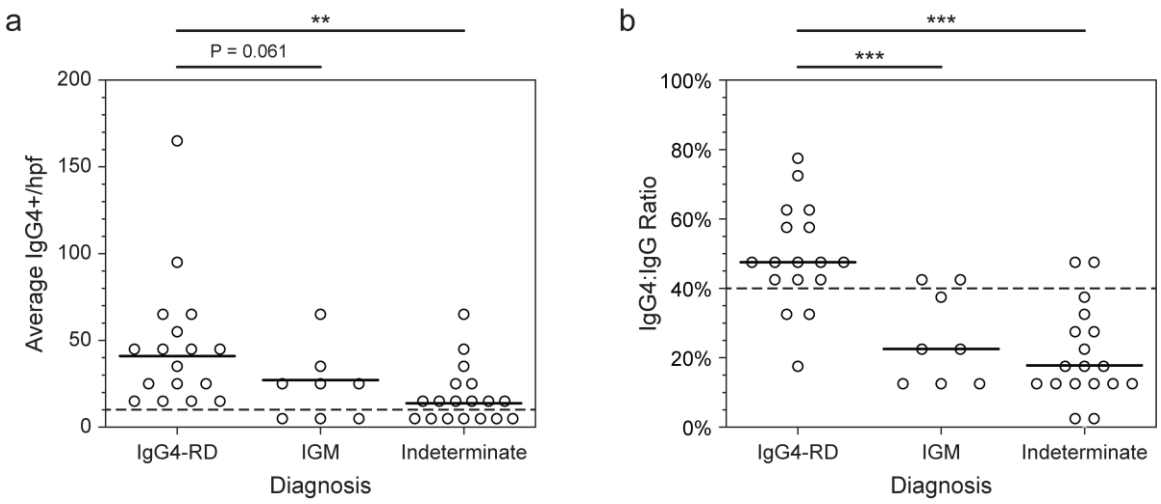

Figure A.3 – Quantification of IgG4 and IgG immunostaining
(**a**) Plot of the average number of IgG4+ plasma cells per high power field. The average IgG4/hpf was significantly higher for the IgG4-RD cases than the indeterminate cases (P<0.01). (**b**) Plot of the IgG4:IgG plasma cell ratio. The IgG4:IgG ratio is significantly greater in the IgG4-RD cases as compared to the IGM and indeterminate cases (each P<0.001). Solid lines represent means, dashed lines the diagnostic cutoffs.

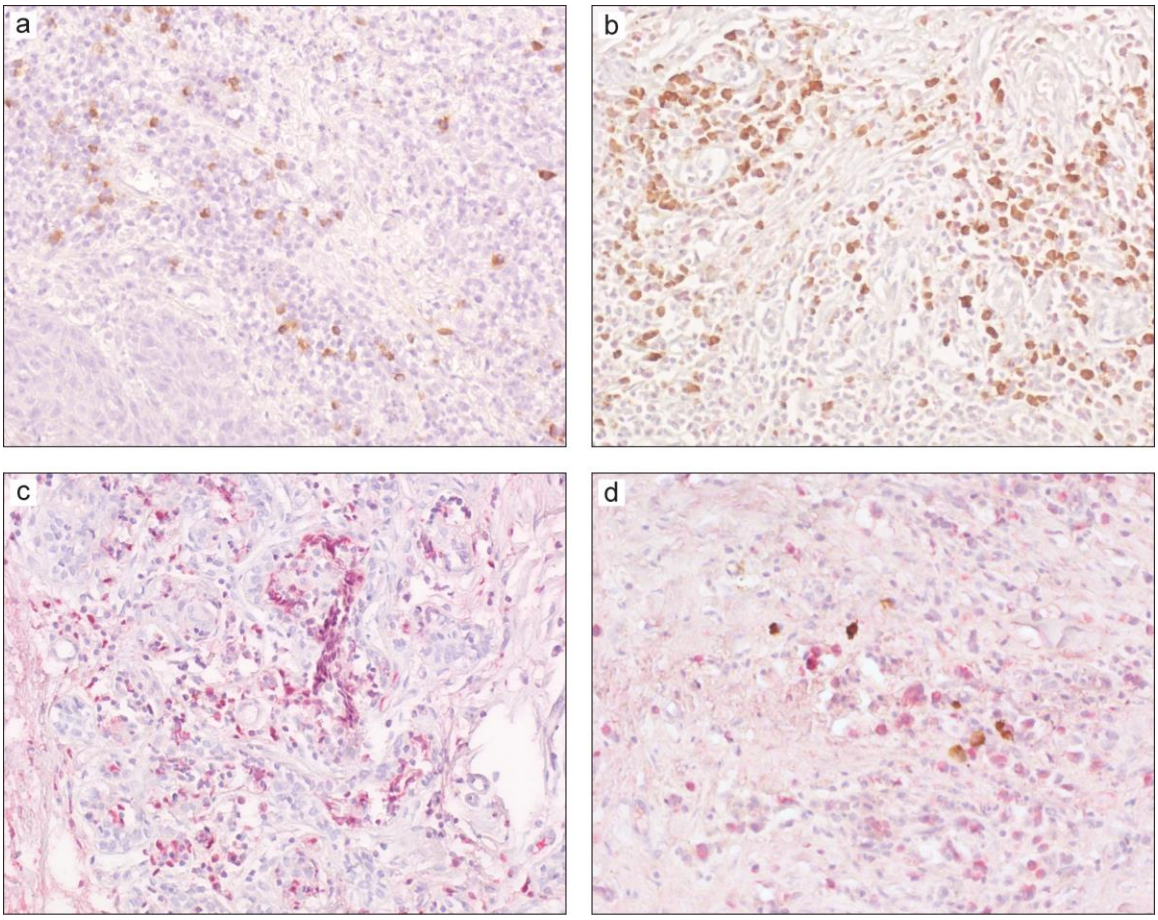

Figure A.4 – IgG4 and IgG immunostaining
Images of dual-stained (IgG4+ brown, IgG+ red) IgG4-RD mastitis cases (**a** and **b**) and IGM cases (**c** and **d**), x200.

Case Number	Diagnosis	Average IgG4/hpf	Average IgG/hpf	Ratio	Dense lymphoplasmacytic infiltrate	Fibrosis, focally storiform	Obliterative phlebitis	Epithelioid histiocytes	Granulomas	Giant cells	Neutrophils
1	IgG4-RD	166	55	75.10%	yes	yes	yes	not epithelioid	vague	present	<5/hpf
2	IgG4-RD	99.3	110	47.50%	yes	yes	yes	none	vague	none	prominent, pockets
3	IgG4-RD	68.3	83.3	45.10%	yes	yes	no phlebitis	not epithelioid	none	none	<5/hpf
4	IgG4-RD	64	22.3	74.10%	yes	yes	yes	none	none	none	prominent, involves skin
5	IgG4-RD	52.7	39.7	57.00%	yes	yes	no phlebitis	yes	none	none	<5/hpf
6	IgG4-RD	48.7	33	59.60%	yes	yes	no phlebitis	not epithelioid	none	none	prominent
7	IgG4-RD	42.3	90	32.00%	yes	yes	yes	yes	none	none	<5/hpf
8	IgG4-RD	41.7	62	40.20%	yes	yes	no veins in section	not epithelioid	none	rare	moderate, pockets
9	IgG4-RD	41	60.3	40.50%	yes	yes	not obliterative	not epithelioid	none	none	<5/hpf
10	IgG4-RD	31	19	62.00%	yes	yes	yes	not epithelioid	vague	rare	<5 hpf
11	IgG4-RD	28.7	122.7	18.90%	yes	yes	yes	none	none	none	<5/hpf
12	IgG4-RD	27.3	28	49.40%	yes	yes	yes	yes	vague	none	<5/hpf
13	IgG4-RD	26.3	16.7	61.20%	yes	yes	yes	not epithelioid	none	none	moderate, central
14	IgG4-RD	19.7	38	34.10%	yes	yes	yes	none	vague	none	<5/hpf
15	IgG4-RD	17.7	18	49.50%	yes	yes	not obliterative	yes	vague	none	<5/hpf
16	IgG4-RD	16.7	23	42.00%	yes	yes	yes	not epithelioid	none	none	<5/hpf
17	IgG4-RD	12	14	46.20%	yes	yes	yes	yes	vague	none	prominent
18	IGM	62.3	82.3	43.10%	yes	yes	no phlebitis	yes	vague	present	<5/hpf
19	IGM	30.3	94	24.40%	yes	not storiform	no veins in section	yes	vague	present	<5 hpf
20	IGM	29.7	113.7	20.70%	mixed	not storiform	no phlebitis	yes	well-formed	present	prominent
21	IGM	27.7	173	13.80%	yes	yes	yes	yes	vague	present	moderate
22	IGM	26.7	36	42.60%	yes	yes	yes	yes	well-formed	present	<5/hpf
23	IGM	9.3	63.7	12.80%	yes	not storiform	no phlebitis	yes	well-formed	present	<5/hpf
24	IGM	9	14.7	38.00%	yes	not storiform	yes	yes	vague	present	<5/hpf
25	IGM	7.3	56	11.60%	yes	not storiform	no phlebitis	yes	vague	present	<5/hpf
26	Indeterminate	60	110.3	35.20%	yes	yes	no phlebitis	not epithelioid	vague	present	<5/hpf
27	Indeterminate	49.7	123.7	28.70%	yes	not storiform	no phlebitis	not epithelioid	none	present	prominent, diffuse
28	Indeterminate	31	77	28.70%	yes	scar	not obliterative	yes	none	none	moderate
29	Indeterminate	23	116.7	16.50%	mixed	no fibrosis	not obliterative	not epithelioid	none	present	prominent
30	Indeterminate	22	198.7	10.00%	mixed	yes	yes	yes	none	present	moderate
31	Indeterminate	18.7	75.7	19.80%	yes	not storiform	no veins in section	yes	none	none	<5/hpf
32	Indeterminate	17.7	129.3	12.00%	yes	yes	no phlebitis	not epithelioid	none	present	<5/hpf
33	Indeterminate	15.3	32	32.40%	mixed	not storiform	no phlebitis	not epithelioid	none	none	moderate
34	Indeterminate	14.7	17.3	45.80%	yes	no fibrosis	no phlebitis	yes	none	none	prominent, central
35	Indeterminate	13	99.3	11.60%	yes	not storiform	no phlebitis	yes	none	none	moderate
36	Indeterminate	13	55	19.10%	yes	scar	yes	none	none	none	<5/hpf
37	Indeterminate	9	10.3	46.60%	yes	scar	no phlebitis	none	none	none	<5/hpf
38	Indeterminate	9	74.3	10.80%	mixed	no fibrosis	not obliterative	not epithelioid	none	rare	prominent
39	Indeterminate	8.7	33	20.80%	yes	not storiform	no phlebitis	yes	vague	none	prominent, central
40	Indeterminate	6.7	59	10.20%	yes	yes	no phlebitis	not epithelioid	none	present	<5/hpf
41	Indeterminate	5	31	13.90%	mixed	scar	no phlebitis	not epithelioid	none	rare	prominent
42	Indeterminate	0.7	247.3	0.30%	yes	not storiform	no phlebitis	not epithelioid	vague	rare	prominent
43	Indeterminate	0	186	0.00%	mixed	no fibrosis	no phlebitis	not epithelioid	none	none	prominent

Table A.1 – Histopathology of Chronic Mastitis
The histopathologic characteristics and IgG4 and IgG immunostaining quantification of the IgG4-RD, IGM, and indeterminate cases.

IgG4-Related Disease Mastitis

Positive Criteria (4 of 5 present):	Negative Criteria (2 of 3 absent):
1. Dense lymphoplasmacytic infiltrate 2. Storiform fibrosis 3. Obliterative phlebitis 4. >10 IgG4 cells/hpf 5. >40% IgG4:IgG ratio	1. Epithelioid histiocytes 2. Well-formed granulomas 3. Giant cells

Idiopathic Granulomatous Mastitis

Positive Criteria (3 of 3 present):	Negative Criteria:
1. Epithelioid histiocytes 2. Vague or well-formed granulomas 3. Giant cells	none

Table A.2 – Diagnostic criteria for IgG4-RD mastitis and IGM
The positive and negative criteria we developed to distinguish IgG4-RD mastitis from IGM.

References

1. Dursun, M. *et al.* Multimodality imaging features of idiopathic granulomatous mastitis: outcome of 12 years of experience. *Radiol Med* **117**, 529-538, (2012).
2. Kuba, S. *et al.* Vacuum-assisted biopsy and steroid therapy for granulomatous lobular mastitis: report of three cases. *Surg Today* **39**, 695-699, (2009).
3. Erozgen, F. *et al.* Corticosteroid treatment and timing of surgery in idiopathic granulomatous mastitis confusing with breast carcinoma. *Breast Cancer Res Treat* **123**, 447-452, (2010).
4. Hovanessian Larsen, L. J., Peyvandi, B., Klipfel, N., Grant, E. & Iyengar, G. Granulomatous lobular mastitis: imaging, diagnosis, and treatment. *AJR Am J Roentgenol* **193**, 574-581, (2009).
5. Oltean, H. N. *et al.* Risk factors for chronic mastitis in morocco and egypt. *Int J Inflam* **2013**, 184921, (2013).
6. Sakurai, K., Fujisaki, S., Enomoto, K., Amano, S. & Sugitani, M. Evaluation of follow-up strategies for corticosteroid therapy of idiopathic granulomatous mastitis. *Surg Today* **41**, 333-337, (2011).
7. Baslaim, M. M., Khayat, H. A. & Al-Amoudi, S. A. Idiopathic granulomatous mastitis: a heterogeneous disease with variable clinical presentation. *World J Surg* **31**, 1677-1681, (2007).
8. Kok, K. Y. & Telisinghe, P. U. Granulomatous mastitis: presentation, treatment and outcome in 43 patients. *Surgeon* **8**, 197-201, (2010).
9. Lai, E. C. *et al.* The role of conservative treatment in idiopathic granulomatous mastitis. *Breast J* **11**, 454-456, (2005).
10. Lacambra, M. *et al.* Granulomatous mastitis: the histological differentials. *J Clin Pathol* **64**, 405-411, (2011).
11. Hur, S. M. *et al.* Experience of treatment of patients with granulomatous lobular mastitis. *J Korean Surg Soc* **85**, 1-6, (2013).
12. Stone, J. H., Zen, Y. & Deshpande, V. IgG4-related disease. *N Engl J Med* **366**, 539-551, (2012).
13. Deshpande, V. *et al.* Consensus statement on the pathology of IgG4-related disease. *Mod Pathol* **25**, 1181-1192, (2012).
14. Umehara, H. *et al.* A novel clinical entity, IgG4-related disease (IgG4RD): general concept and details. *Mod Rheumatol* **22**, 1-14, (2012).
15. Kamisawa, T., Takuma, K., Egawa, N., Tsuruta, K. & Sasaki, T. Autoimmune pancreatitis and IgG4-related sclerosing disease. *Nat Rev Gastroenterol Hepatol* **7**, 401-409, (2010).
16. Deshpande, V. & Khosroshahi, A. Diagnostic guidelines for IgG4-related disease with a focus on histopathological criteria. *Diagnostic Histopathology* **19**, 119-127, (2013).
17. Mahajan, V. S., Mattoo, H., Deshpande, V., Pillai, S. S. & Stone, J. H. IgG4-Related Disease. *Annu Rev Pathol* **9**, 315-347, (2014).

18. Zen, Y. & Nakanuma, Y. IgG4-related disease: a cross-sectional study of 114 cases. *Am J Surg Pathol* **34**, 1812-1819, (2010).
19. Cheuk, W. *et al.* IgG4-related sclerosing mastitis: description of a new member of the IgG4-related sclerosing diseases. *Am J Surg Pathol* **33**, 1058-1064, (2009).
20. Ogura, K. *et al.* IgG4-related tumour-forming mastitis with histological appearances of granulomatous lobular mastitis: comparison with other types of tumour-forming mastitis. *Histopathology* **57**, 39-45, (2010).
21. Ogiya, A. *et al.* IgG4-related sclerosing disease of the breast successfully treated by steroid therapy. *Breast Cancer* **21**, 231-235, (2014).
22. Zen, Y. *et al.* Inflammatory pseudotumor of the breast in a patient with a high serum IgG4 level: histologic similarity to sclerosing pancreatitis. *Am J Surg Pathol* **29**, 275-278, (2005).
23. Dite, P. *et al.* Unusual Multiorgan Immunoglobulin G4 (IgG4) Inflammation: Autoimmune Pancreatitis, Mikulicz Syndrome, and IgG4 Mastitis. *Gut Liver* **7**, 621-624, (2013).
24. Schwartz, T. *et al.* Expression of aldehyde dehydrogenase 1 as a marker of mammary stem cells in benign and malignant breast lesions of Ghanaian women. *Cancer* **119**, 488-494, (2013).